



저작자표시-비영리-변경금지 2.0 대한민국

이용자는 아래의 조건을 따르는 경우에 한하여 자유롭게

- 이 저작물을 복제, 배포, 전송, 전시, 공연 및 방송할 수 있습니다.

다음과 같은 조건을 따라야 합니다:



저작자표시. 귀하는 원저작자를 표시하여야 합니다.



비영리. 귀하는 이 저작물을 영리 목적으로 이용할 수 없습니다.



변경금지. 귀하는 이 저작물을 개작, 변형 또는 가공할 수 없습니다.

- 귀하는, 이 저작물의 재이용이나 배포의 경우, 이 저작물에 적용된 이용허락조건을 명확하게 나타내어야 합니다.
- 저작권자로부터 별도의 허가를 받으면 이러한 조건들은 적용되지 않습니다.

저작권법에 따른 이용자의 권리는 위의 내용에 의하여 영향을 받지 않습니다.

이것은 [이용허락규약\(Legal Code\)](#)을 이해하기 쉽게 요약한 것입니다.

[Disclaimer](#)

공학박사학위논문

**나노입자 적층시스템과 집속이온빔을  
이용한 나노스케일 3차원 인쇄 공정**

**Nanoscale 3D Printing Process using Nano Particle  
Deposition System and Focused Ion Beam**

2013 년 2 월

서울대학교 대학원

기계항공공학부

김 충 수



공학박사학위논문

**나노입자 적층시스템과 집속이온빔을  
이용한 나노스케일 3차원 인쇄 공정**

**Nanoscale 3D Printing Process using Nano Particle  
Deposition System and Focused Ion Beam**

2013 년 2 월

서울대학교 대학원

기계항공공학부

김 충 수



나노입자 적층시스템과 집속이온빔을  
이용한 나노스케일 3차원 인쇄 공정  
Nanoscale 3D Printing Process using Nano Particle  
Deposition System and Focused Ion Beam

지도교수 안 성 훈

이 논문을 공학박사 학위논문으로 제출함

2013 년 2 월

서울대학교 대학원

기계항공공학부

김 충 수

김충수의 공학박사 학위논문을 인준함

2013 년 2 월

위 원 장 : 이 건 우

부위원장 : 안 성 훈

위 원 : 장 동 영

위 원 : 서 갑 양

위 원 : 차 석 원





# ABSTRACT

## Nanoscale 3D Printing Process using Nano Particle Deposition System and Focused Ion Beam

Chung-Soo Kim

School of Mechanical and Aerospace Engineering

The Graduate School

Seoul National University

A novel nanoscale 3D printing process was developed with the main stream of down-scaling of structures and systems. In order to find out the way of building 3D micro- and nanostructures with multimaterials, two technological paradigms of '*3D printing*' and '*hybrid*' were combined to get the high impact of synergy by integrating nano particle deposition system (NPDS) and focused ion beam (FIB). The NPDS which sprays micro- and nano-sized particle at supersonic speed was utilized to layer-up thin films with multimaterials (ceramics and metals). FIB was adopted as a profiling nanostructures to the single and multilayer of thin films, i.e., profile cutting.

In order to show the feasibility of multimaterial processing through NPDS, various kinds of materials of metal and ceramic were deposited on various substrate such as metal, ceramic and polymers. Among those film materials, Sn, TiO<sub>2</sub> and Al<sub>2</sub>O<sub>3</sub> were investigated deeply as an engineering film. The deposition characteristics were studied by controlling the feed rate and stand-off distance. Each film's physical properties were investigated for the verification as engineering films. The hardness, the elastic Modulus, bonding strength (peel-put test and work of adhesion) and microstructural changes were investigated. Furthermore, the bonding mechanism of metal and ceramic by NPDS was thoroughly investigated through the transmission electron microscope (TEM) by observing the interfaces of the particle-to-particle and particle-to-substrate. Especially in metal particle of Sn, the evolution mechanism,

related to the bonding mechanism, from particle to film was proved with the experimental model.

In order for the FIB to fabricate the target precisely, the advanced scan method, which adopted the dot-to-dot scan, was compared to the conventional scan method. In order to understand and avoid the defective structure from conventional scan method, the dwell time and the beam overlap were taken into consideration, and their effects were investigated. On the basis of these two parameters, several ion beam paths adaptive for 2D/3D target shapes were generated, and it improved the precision and the yield in FIB fabrication.

In order to apply for 3D micro- and nanostructures with multimaterials, the combination and repetition of NPDS and FIB were performed by resulting in the feasibility of nanoscale 3D printing process. With a series of experiments the new process showed the multilayered structure with multimaterial deposition, the profiling of multilayered nanostructure by FIB, the selective profiling of nanostructure, and the repetition of both additive and subtractive processes as a printing process. Additionally, the NPDS showed not only its patterning resolution could be achieved below 50 nm but also it could build the high aspect ratio over 5 when it combined with FIB process.

As an application, the smart material of shape memory alloy (NiTi) was utilized for the fabrication of functional nanostructure. The FIB showed that it can fabricate the nanostructure of NiTi with the 1<sup>st</sup> order bucking mode model, and the thermally-driven nanomanipulation of NiTi was performed via *in situ* TEM. The NPDS showed that it has the potential to deposit the metal material of Sn on NiTi with the good adhesion status.

**Keywords:** Nanoscale 3D Printing System, Nano Particle Deposition System, Focused Ion Beam, Multimaterial, Nanomanipulator

**Student Number:** 2007-30192

# Contents

<b>CHAPTER 1 Introduction</b>	<b>1</b>
1.1 Micro/nano manufacturing processes and their applications	1
1.2 Research trends in micro/nano manufacturing processes	2
1.2.1 3D printing technology	2
1.2.2 What is “ <i>hybrid</i> ” in manufacturing regime?	5
1.3 Recent advances in micro/nano manufacturing processes	7
1.4 Development of nanoscale 3D printing process	8
<b>CHAPTER 2 Process design and system integration</b>	<b>10</b>
2.1 Conceptual design	10
2.2 Design of nanoscale 3D printing process	11
2.2.1 Nano particle deposition system (NPDS)	11
2.2.2 Focused ion beam (FIB)	12
2.2.3 Nanoscale 3D printing process	13
2.3 Design for functionality	13
2.3.1 Functions for NPDS	14
2.3.2 Functions for FIB	14
2.4 Development of system	14
2.4.1 Nano particle deposition system (NPDS)	14
2.4.2 Focused ion beam (FIB)	15
2.4.2.1 FIB column	15
2.4.2.2 Secondary electron detector (SED)	15
2.4.2.3 High vacuum compatible 5-axes eucentric stage	16
2.4.2.4 Main processing chamber	17
2.4.2.5 Evacuation system	19

2.5 Integration of FIB system	20
2.6 Essential requirements for nanoscale 3D printing process	23
<b>CHAPTER 3 Nanostructuring by NPDS</b>	<b>24</b>
3.1 Overview	24
3.2 Process parameters	26
3.3 Materials	27
3.3.1 Metal: Tin, Sn	27
3.3.2 Ceramic: Titanium oxide, TiO <sub>2</sub>	29
3.3.3 Ceramic: Aluminum oxide, Al <sub>2</sub> O <sub>3</sub>	32
3.4 Deposition of metal and ceramic films	32
3.4.1 Overview	32
3.4.2 Experimental conditions	32
3.4.3 Films thicknesses of metal and ceramic	34
3.5 Characterization of metal and ceramic films	35
3.5.1 Overview	35
3.5.2 Strength of films	36
3.5.3 Bonding of films	37
3.5.3.1 Peel-out test by adhesive tape	37
3.5.3.2 Work of adhesion	38
3.5.4 Microstructural property	41
<b>CHAPTER 4 Nanostructuring by FIB</b>	<b>44</b>
4.1 Overview	44
4.2 Definition of FIB parameters	46
4.2.1 Ion beam parameters	46
4.2.2 Processing parameters	46

4.2.3 Ion beam path parameters	47
4.2.4 Evaluation parameters	47
4.2.5 Relative parameters	47
4.3 Material	47
4.4 Instrumentation	48
4.5 Modeling of scan method	49
4.6 Understanding of nanoscale phenomena	53
4.6.1 Influence of dwell time	54
4.6.1.1 Overview	54
4.6.1.2 Experiment	55
4.6.1.3 Surface morphology	57
4.6.1.4 Compositional characteristic	59
4.6.1.5 Physicochemical characteristic	64
4.6.1.6 Summary	65
4.6.2 Influence of beam overlap	66
4.6.2.1 Overview	66
4.6.2.2 Experimental conditions	67
4.6.2.3 Ion/solid and ion/gas molecule interactions	68
4.6.2.4 Surface morphology	68
4.6.2.5 Deposition rates as a function of beam overlap	72
4.6.2.6 Summary	74
4.7 Ion beam path for FIB fabrication	75
4.7.1 Overview	75
4.7.2 Generation of ion beam path	75
4.7.3 Experimental conditions	77
4.7.4 Surface morphology	77
4.7.5 Evaluation of geometrical precision and accuracy	79
4.7.6 Evaluation of geometrical precision	80

4.7.7 Evaluation of geometrical accuracy	81
4.7.8 Summary	84
4.8 Advanced fabrication strategy for 3D nanostructures	84
4.8.1 Overview	84
4.8.2 Fabrication strategy	86
4.8.3 Geometry from micro-mould	87
4.8.4 Geometry from polymer replication	88
4.8.5 Summary	91
<b>CHAPTER 5 Nanostructuring by 3D printing process</b>	92
5.1 Overview	92
5.2 Multilayer structure with multimaterials	93
5.3 Step coverage of NPDS in the nanostructured substrate	95
5.3.1 Fabrication of nanostructured substrate by FIB	95
5.3.2 Deposition of metal and ceramic films by NPDS	96
5.3.3 Surface morphology of metallic and ceramic nanostructures	98
5.3.4 Aspect ratio of metal and ceramic nanostructure	101
5.4 FIB profiling of multilayer structure with multimaterials	102
5.5 Selective FIB profiling of multilayered structure	104
5.5.1 Algorithm for selective FIB profiling	104
5.5.2 Selective FIB profiling on multilayer structures	106
5.6 Hybrid nanofabrication via repeated procedure	108
<b>CHAPTER 6 Interface &amp; Mechanism</b>	110
6.1 Overview	110
6.2 Interface and mechanism of metallic particle deposition	110
6.2.1 Interface between metallic (Sn) film and substrate	110

6.2.2 Evolution mechanism of metallic film of Sn	113
6.3 Interface and mechanism of ceramic particle deposition	117
6.3.1 Interface and mechanism of TiO <sub>2</sub> film	117
6.3.2 Interface and mechanism of Al <sub>2</sub> O <sub>3</sub> film	119
<b>CHAPTER 7 Functional nanostructures</b>	<b>122</b>
7.1 Overview	122
7.2 Shape memory alloy of TiNi	122
7.3 Sample preparation and instrumentation	123
7.3.1 Memorizing the geometry of NiTi	123
7.3.2 Fabrication of nanoscale beam of TiNi	124
7.3.3 Instrumentation for nanomanipulation	124
7.4 Manipulation of nanoscale TiNi beam	125
7.5 Model for NiTi actuation	128
<b>CHAPTER 8 Conclusions</b>	<b>132</b>
<b>Bibliography</b>	<b>134</b>

# List of Tables

<b>Table 1.1</b> Comparisons of current 3D micro- and nano printers	4
<b>Table 1.2</b> Current hybrid manufacturing technologies	7
<b>Table 1.3</b> The next generation manufacturing technologies for 3D nanostructures	8
<b>Table 2.1</b> Basic and optional components for the design of the main processing chamber	17
<b>Table 2.2</b> Specification of FIB system	22
<b>Table 3.1</b> Comparison between NPDS and ALD	24
<b>Table 3.2</b> Progresses on deposition by NPDS	25
<b>Table 3.3</b> Multimaterial combinations by NPDS	26
<b>Table 3.4</b> Experimental conditions of NPDS for Sn, TiO <sub>2</sub> and Al <sub>2</sub> O <sub>3</sub>	33
<b>Table 3.5</b> Physical properties and their measurement method	35
<b>Table 3.6</b> Hardness and elastic Modulus of metal and ceramic films	36
<b>Table 3.7</b> Peel-out test by adhesive tape	37
<b>Table 3.8</b> Contact angles, surface energy values and work of adhesion of Sn, TiO <sub>2</sub> and Al <sub>2</sub> O <sub>3</sub> films (W: water and E: ethanol)	40
<b>Table 4.1</b> Target geometries for nanostructuring by FIB	46
<b>Table 4.2</b> Relative parameters according to the scan style in the raster scan	51
<b>Table 4.3</b> Experimental conditions	55
<b>Table 4.4</b> Overall chemical compositions of six FIB microstructures	59
<b>Table 4.5</b> Experimental conditions	77
<b>Table 4.6</b> Comparisons between fabricated moulds and replicated PUA microstructures	90

<b>Table 5.1</b> Experimental conditions for multilayer structure with multimaterials	94
<b>Table 5.2</b> Experimental conditions for nanostructured substrates	96
<b>Table 5.3</b> Experimental conditions for metal and ceramic deposition on the nanostructured substrate	97

# List of Figures

<b>Figure 1.1</b> Micro- and nano manufacturing and their applications	2
<b>Figure 1.2</b> Historical review of 3D printing technologies from the invention to the state-of-art	3
<b>Figure 1.3</b> Current three 3D printing technologies in micro- and nanoscale: (a) two photon lithography, (b) FIB-CVD and (3) FIB & FIB-CVD & implantation	4
<b>Figure 1.4</b> Convergence of <i>'top-down'</i> and <i>'bottom-up'</i> nanotechnology for the next generation nanomanufacturing process	6
<b>Figure 1.5</b> The nanoscale 3D printing process in the manufacturing processes with the consideration of a dimensional complexity and a scale of shape	9
<b>Figure 2.1</b> Conceptual description for nanoscale 3D printing process integrated by both NPDS and FIB	10
<b>Figure 2.2</b> Description of NPDS.	11
<b>Figure 2.3</b> Description of FIB system	12
<b>Figure 2.4</b> Process flow of nanoscale 3D printing process	13
<b>Figure 2.5</b> Backside view of vacuum compatible 5-axes eucentric stage looked from the rear of chamber towards the front door to show how the 5-axes motion plays	16
<b>Figure 2.6</b> Accessible port configurations for multifunctional nano production in FIB system	17
<b>Figure 2.7</b> Assembled 3D model of FIB system	19
<b>Figure 2.8</b> Description of evacuation system for FIB system	20
<b>Figure 2.9</b> Assembled FIB system placed in Seoul National University	21
<b>Figure 2.10</b> Inside of the main processing chamber and assembled components taken from IR-CCD camera	21

<b>Figure 2.11</b> The representative target geometries for the performance verification of nanoscale 3D printing process	23
<b>Figure 3.1</b> Fish-bone diagram for particle deposition in NPDS.	27
<b>Figure 3.2</b> FE-SEM images of virgin Sn particles: 2-20 $\mu\text{m}$ in diameters	28
<b>Figure 3.3</b> HR-TEM images of Sn virgin particle: (a) TEM sample of Sn fabricated by FIB lift-off technique, (a <sub>1</sub> ) SIM image of Sn TEM sample (60° tilt view), (b) Sn with dislocational defects (low magnification), (c) lattices of Sn without defects, and (d) lattices of Sn with dislocational defects	28
<b>Figure 3.4</b> FE-SEM images of TiO <sub>2</sub> nanoparticles	30
<b>Figure 3.5</b> HR-TEM images of TiO <sub>2</sub> nanoparticles: (a) agglomerated TiO <sub>2</sub> nanoparticles, and (b) crystalline TiO <sub>2</sub> nanoparticles (detail view of box in Figure 3.5(a))	30
<b>Figure 3.6</b> FE-SEM images of Al <sub>2</sub> O <sub>3</sub> nanoparticles	31
<b>Figure 3.7</b> HR-TEM images of Al <sub>2</sub> O <sub>3</sub> nanoparticle: (a) agglomerated Al <sub>2</sub> O <sub>3</sub> nanoparticles, (b) magnified view of 20 nm particles, and (c) crystalline structure of Al <sub>2</sub> O <sub>3</sub> nanoparticles	31
<b>Figure 3.8</b> Description of two parameters, the feed rate and SoD, in NPDS	33
<b>Figure 3.9</b> Film thicknesses of metal and ceramic films: (a) Sn, (b) TiO <sub>2</sub> and (c) Al <sub>2</sub> O <sub>3</sub> as functions of the feed rate and SoD	34
<b>Figure 3.10</b> XRD results of Sn: before and after deposition	41
<b>Figure 3.11</b> XRD results of TiO <sub>2</sub> : before and after deposition	42
<b>Figure 3.12</b> XRD results of Al <sub>2</sub> O <sub>3</sub> : before and after deposition	43
<b>Figure 4.1</b> 2D illustration of nanoscale phenomena induced by ion-solid interactions: representative surface morphology of FIB milled structure influenced by the various nanoscale phenomena such as surface amorphization, material redeposition, self-focusing and	45

material swelling.

**Figure 4.2** SMI 3050 (SII Nanotechnology Inc.) with (a) *in situ* Monitoring system and (b) inside of main processing chamber 48

**Figure 4.3** Two types of scan style for the development of raster scan: (a) normal raster scan (synchronized with scan signal when imaging) and (b) raster scan with dot-to-dot 50

**Figure 4.4** Ion beam tracking in the raster scan utilized with dot-to-dot scan style: (a) without area blanking time and (b) with area blanking time 51

**Figure 4.5** Modified scan method from Figure 4.3(b) 52

**Figure 4.6** Simulation of the effect of both dwell time and beam overlap to the ion beam irradiation enhancement factor (F) and the processing time (total ion beam processing time (E)) according to the scan styles of conventional raster scan ( $a_{1-2}$ ) and dot-to-dot scan ( $b_{1-2}$ ) 53

**Figure 4.7** FE-SEM images of FIB milled microstructures: ( $a_1 \sim f_1$ ) plain view, ( $a_2 \sim f_2$ ) 45° tilt view and ( $a_3 \sim f_3$ ) 45° tilt view which are rotated 90° to the counterclockwise from ( $a_2 \sim f_2$ ). The continuous arrow indicates the horizontal scan direction and the dotted arrow indicates the vertical scan direction 56

**Figure 4.8** 3D optical profiles of FIB milled microstructures: (a) 1  $\mu$ sec, (b) 200  $\mu$ sec, (c) 400  $\mu$ sec, (d) 600  $\mu$ sec, (e) 800  $\mu$ sec, and (f) 1,000  $\mu$ sec of dwell times (two arrows express the ion beam scan directions in horizontal and vertical) 58

**Figure 4.9** 3D compositional mapping of silicon using EPMA: (a) 1  $\mu$ sec, (b) 200  $\mu$ sec, (c) 400  $\mu$ sec, (d) 600  $\mu$ sec, (e) 800  $\mu$ sec and (f) 1,000  $\mu$ sec of dwell times 60

**Figure 4.10** 3D compositional mapping of silicon using EPMA: (a) 1  $\mu$ sec, (b) 200  $\mu$ sec, (c) 400  $\mu$ sec, (d) 600  $\mu$ sec, (e) 800  $\mu$ sec and (f) 61

1,000  $\mu$ sec of dwell times

**Figure 4.11** The detail view of Figure 4.9(c): the area A indicates the region where the material swelling occurs, and the area B indicates the region where the self-focusing effect occurs 63

**Figure 4.12** (a) *Raman spectra* of pristine and FIB milled microstructures on the silicon (100) wafer with 1  $\mu$ sec of dwell time. Spectroscopic Raman mapping of FIB milled microstructures on the silicon (100) wafer with (b) 1  $\mu$ sec and (c) 400  $\mu$ sec of dwell time. Color bar displays relative intensity ( $I_{c-Si}/I_{a-Si}$ ); top (red) and bottom (blue) means high and low intensity, respectively. 63

**Figure 4.13** (a) Four different regions, marked by labels, for obtaining the *Raman spectra* of each zone of FIB milled wafers with (b) 1  $\mu$ sec and (c) 400  $\mu$ sec of dwell time 65

**Figure 4.14** Schematics of the ion beam processing as a function of beam overlap. The pixel size was 30 nm, and the probe diameter was 31 nm as measured by the knife edge method (simplified to 30 nm) 67

**Figure 4.15** Top views of SIM images: the carbon using phenanthrene gas molecules was deposited as a function of beam overlap; a: -900 %, b: -800 %, c: -700 %, d: -600 %, e: -500 %, f: -400 %, g:-300 %, h:-200 %, i:-100 %, j: 0 %, and k: 50 % 69

**Figure 4.16** Tilt views of SEM images: Top view of SIM images: the carbon using phenanthrene gas molecules was deposited as a function of beam overlap; a: -900 %, b: -800 %, c: -700 %, d: -600 %, e: -500 %, f: -400 %, g:-300 %, h:-200 %, i:-100 %, j: 0 %, and k: 50 % 69

**Figure 4.17** Measured dimensions (width, length, and thickness) and deposition rate as a function of beam overlap 71

**Figure 4.18** Deposition rate and processing time as a function of beam overlap 73

<b>Figure 4.19</b> Volumetric changes and deposition rate as a function of beam overlap	73
<b>Figure 4.20</b> Five types of ion beam paths for hollow circular geometry	76
<b>Figure 4.21</b> Traces of ion beam paths, depicted in Figure 4.20, by FIBID	76
<b>Figure 4.22</b> Fabrication results of seven types of scan strategies: (a) raster scan with beam blanking, (b) raster scan without beam blanking, (c) serpentine scan, (d) offset scan (inbound), (e) offset scan (outbound), (f) spiral scan (inbound), and (g) spiral scan (outbound). The former subscripts 1 and 2 represent the 5 $\mu$ sec and 500 $\mu$ sec dwell time, respectively	78
<b>Figure 4.23</b> Image processing algorithm for the precision and accuracy measurements of the hollow circular structure	79
<b>Figure 4.24</b> Precision of inner and outer diameters on top surface	80
<b>Figure 4.25</b> Precision of inner and outer diameters on top surface	81
<b>Figure 4.26</b> Roundness of inner diameter at top surface	82
<b>Figure 4.27</b> Roundness of outer diameter at top surface	82
<b>Figure 4.28</b> Roundness of inner diameter at bottom surface	82
<b>Figure 4.29</b> Roundness of outer diameter at bottom surface	83
<b>Figure 4.30</b> Concentricity between inner and outer circles at top surface	83
<b>Figure 4.31</b> Concentricity between inner and outer circles at bottom surface	83
<b>Figure 4.32</b> Comparison of complexity of process design: (a) stepwise process and (b) serial process	84
<b>Figure 4.33</b> Three different methodologies for 3D geometry: a) Vasile's method: sputtering by changing the dwell time on the pixel, b) Fu's method: sputtering the sequential 2D slice by slice, and c) continuous slicing method (CSM): it is modified by repeating the Fu's method	85

continuously by reducing the ion dose for each one slice, while the total ion dose is the same as Fu's method

**Figure 4.34** Comparisons between Fu's method and CSM; (a) has stair-step structures (defective structure) and (b) has no defective structure 87

**Figure 4.35** Definitions for a fabricated mould, and the SIM image of a fabricated mould: all the fabricated moulds have a diameter of about 4  $\mu\text{m}$ . 88

**Figure 4.36** Mould depth and sputtering yield as a function of ion dose for three specific dwell times of 0.5  $\mu\text{sec}$ , 1.0  $\mu\text{sec}$ , and 2.0  $\mu\text{sec}$  88

**Figure 4.37** Polymeric microstructure (PDMS) replicated from silicon micro-mould in case of highest ion dose case of  $4.13 \times 10^{17}$  ions/ $\text{cm}^2$ , having a depth of 1283.25 nm 89

**Figure 4.38** 3D optical surface profiles replicated from PUA microstructures 90

**Figure 5.1** Target geometries for depicting the nanoscale 3D printing process integrated by NPDS and FIB 92

**Figure 5.2** Description of multilayer structure with multimaterials of Sn and  $\text{Al}_2\text{O}_3$  by NPDS 93

**Figure 5.3** FE-SEM image of a cross-section of multilayer system, Sn/ $\text{Al}_2\text{O}_3$ /Sn on Si, with the line EDS result. 94

**Figure 5.4** Experimental procedures for metal and ceramic nanofabrication on patterned substrate 95

**Figure 5.5** FIB fabricated nanoscale patterns on silicon substrates as function of pattern width and ion doses (for depth control) 96

**Figure 5.6** Cross-sections of Sn metallic film on the nanostructured Si substrate: the applied ion doses were increased from (a) to (e) as following; 1.3, 2.7, 4.0, 5.3, and  $6.7 \times 10^{18}$  ions/ $\text{cm}^2$  97

**Figure 5.7** Cross-sections of nanoporous structures of  $\text{TiO}_2$ : the 98

applied ion doses were increased from (a) to (e) as following; 1.3, 2.7, 4.0, 5.3, and  $6.7 \times 10^{18}$  ions/cm<sup>2</sup>

**Figure 5.8** Cross-sections of nanoporous structures of Al<sub>2</sub>O<sub>3</sub>: the applied ion doses were increased from (a) to (e) as following; 1.3, 2.7, 4.0, 5.3, and  $6.7 \times 10^{18}$  ions/cm<sup>2</sup> 99

**Figure 5.9** Depths as functions of widths and ion doses in the nanostructured patterns: (a) Sn, (b) TiO<sub>2</sub>, and (c) Al<sub>2</sub>O<sub>3</sub> 100

**Figure 5.10** Aspect ratios functions of widths and ion doses in the nanostructured patterns: (a) Sn, (b) TiO<sub>2</sub>, and (c) Al<sub>2</sub>O<sub>3</sub> 101

**Figure 5.11** Images used for FIB profile cutting: (a) line shape and (b) rectangular shape 102

**Figure 5.12** Fabrication of nanowalls in the Sn/Al<sub>2</sub>O<sub>3</sub>/Sn on Si: it was observed at a 30° tilt angle in SIM 103

**Figure 5.13** Fabrication of micropillar in the Sn/Al<sub>2</sub>O<sub>3</sub>/Sn on Si: it was observed at a 45° tilt angle in SIM 103

**Figure 5.14** Difference of FIB milling rate on Sn film deposited by NPDS 104

**Figure 5.15** Algorithm for selective FIB profiling 105

**Figure 5.16** Redefinition of FIB processing area for the selective FIB profiling 106

**Figure 5.17** Procedures for the selective FIB profiling on the irregular Sn surface 107

**Figure 5.18** Fabrication of metallic electrodes (Sn) on dielectric layer (Al<sub>2</sub>O<sub>3</sub>) using selective FIB profiling technique 108

**Figure 5.19** Fabricated Sn/Al<sub>2</sub>O<sub>3</sub>/Sn/Si wafer structure with an Al<sub>2</sub>O<sub>3</sub> pocket. 109

**Figure 6.1** Interface of Sn film on substrate 111

**Figure 6.2** Interface of Sn film inside the nanostructured substrate 112

<b>Figure 6.3</b> The Gaussian shaped NPDS deposition	114
<b>Figure 6.4</b> Sn particle deposition: (a-b): before particle deposition on aluminum substrate and (c-d): after particle deposition on soft PDMS substrate	114
<b>Figure 6.5</b> The Sn thin lamella taken by FIB lift-off technique from the regions of A-C in Figure 6.3: (a) region A, (b) region B, and (c) region C in Figure 6.3. The subscriptions of 1 and 2 represent the SIM and TEM images, respectively.	115
<b>Figure 6.6</b> Observation on the formation and the growth of nanoparticles in Sn films with <i>in situ</i> heating in TEM: (a) 350 °C, (b) 400 °C and (c) 500 °C.	116
<b>Figure 6.7</b> Evolution mechanism of Sn thin film by NPDS	117
<b>Figure 6.8</b> HR-TEM images of nanoporous TiO <sub>2</sub> thin film: (a) interface between film and substrate, (b) amorphization of TiO <sub>2</sub> and (c) nanocrystalline TiO <sub>2</sub> particles	118
<b>Figure 6.9</b> HR-TEM images of nanoporous TiO <sub>2</sub> structure inside the nanostructured substrate: (a) amorphous necking networks between aggregated particles, (b) adhesion interface: particle-to-particle and particle-to-substrate and (c) magnified view of amorphous necking network	119
<b>Figure 6.10</b> HR-TEM images of Al <sub>2</sub> O <sub>3</sub> thin film: (a) interface between film and substrate, (b) interface between particles in the middle of film and (c) low densification region with small porosity	120
<b>Figure 6.11</b> HR-TEM images of nanoporous Al <sub>2</sub> O <sub>3</sub> structure inside the nanostructured substrate: (a) near the top surface region, (b) near the middle surface region and (c) near the down surface region	121
<b>Figure 7.1</b> HR-TEM images of shape memory alloy of TiNi	123
<b>Figure 7.2</b> Fabrication of TiNi nanoscale beam using one-way TiNi (a),	124

two-way TiNi (b) and Sn on tow-way TiNi (c)

**Figure 7.3** *in situ* TEM (JEM-3011 (HR), Jeol Ltd, Japan) which can heat up the sample up to 800°C and can observe in real time with CCD camera (SC 1000, Gatan Inc.) and its heating sample holder; the NiTi sample was loaded in the sample holder 125

**Figure 7.4** Manipulation of one-way nanoscale TiNi beam: (a) 25 °C, (b) 100°C, (c) 150 °C and (d) 200 °C 126

**Figure 7.5** Manipulation of two-way nanoscale TiNi beam: (a) 25 °C, (b) 250°C, (c) 25 °C, (d) 250 °C and (e) 25 °C 127

**Figure 7.6** Manipulation principle of nanoscale TiNi beam 128

**Figure 7.7** Structural model and geometrical configuration of nanoscale TiNi beam 129

**Figure 7.8** Comparison of experimental and theoretical results of one-way nanoscale TiNi beam 131

**Figure 7.9** Comparison of experimental and theoretical results of two-way nanoscale TiNi beam 131

# 1 Introduction

## 1.1 Micro/nano manufacturing processes and their applications

The phenomenon of miniaturization, *down-scaling*, is probably most commemorative encapsulation in *Moore's law* of 1965, which declared that the number of transistors on computer semiconductor chips would double at about every two years [1, 2]. This declaration has proved remarkably strong, and it has been brought the concentration on manufacture and production at ever-decreasing scales triggered striking developments in fields of materials, processes and product innovations with the help of various micro/nano manufacturing processes. These innovations come from not only conventional manufacturing processes such as mechanical machining processes, including turning, milling, etc, but also non-conventional processes, electron beam lithography, nano imprinting, etc. Both types of manufacturing processes were still in improving and developing in the criteria of micro/nano manufacturing processes. Resultantly, these innovations have been leading in lots of applications in industrial and academic uses, as shown in Figure 1.1 [3-7].

Developing more functions with variable purposes into smaller device dimensions is one of the solutions to satisfy requirements such as higher standards of living, healthcare, and quality of consumer's goods and curiosities. This growing significance of micro/nano manufacturing led to provision for dedicated topics within the nanotechnology and nanosciences, multifunctional materials, knowledge based manufacturing, advanced manufacturing processes and devices through tremendous elaboration of researches and businesses [3, 8].



**Figure 1.1** Micro- and nano manufacturing and their applications

## 1.2 Research trends in micro/nano manufacturing processes

With the main stream of ‘*down-scaling*’ of structures and devices it is noticeable to focus on two leading paradigms for the development of advanced manufacturing processes, which can lead significant technological advances. The first paradigm is the ‘*3D printing technology*’, and the second paradigm is ‘*hybrid*’ in manufacturing.

### 1.2.1 3D printing technology

The roadmap of multimaterial micro manufacture which published in 2006 by Dimov *et al.* suggested that the 3D printing technology will be the first priority with strongly perceived importance in various manufacturing processes [9]. The 3D printing technology has advantages of manufacturing the functional structures with comparably easy and fast because the

conventional process has disadvantages of complexity which driven by the various combination of several manufacturing processes. There are several types of 3D printing processes and systems, which are well known, invented by universities and companies [10-14]. The historical 3D printing technologies are shown in Figure 1.2. From this figure, it can be identified that 3D printing technology also follows the main stream of ‘down-scaling’ of structures and systems like other manufacturing technologies. Even though it has been paying tremendous attentions with the demand of easy-making, there are only three printing processes dealing with hundreds of micro- and nanoscale with 3D structures; (1) two photon lithography (microscale) [15], (2) focused ion beam - chemical vapor deposition (FIB-CVD) (nanoscale) [16] and (3) Combination of FIB & FIB-CVD and deep reactive ion etching (nanoscale) [17]. These examples of 3D micro- and nanostructures are illustrated in Figure 1.3, and the comparisons are illustrated in Table 1.1.

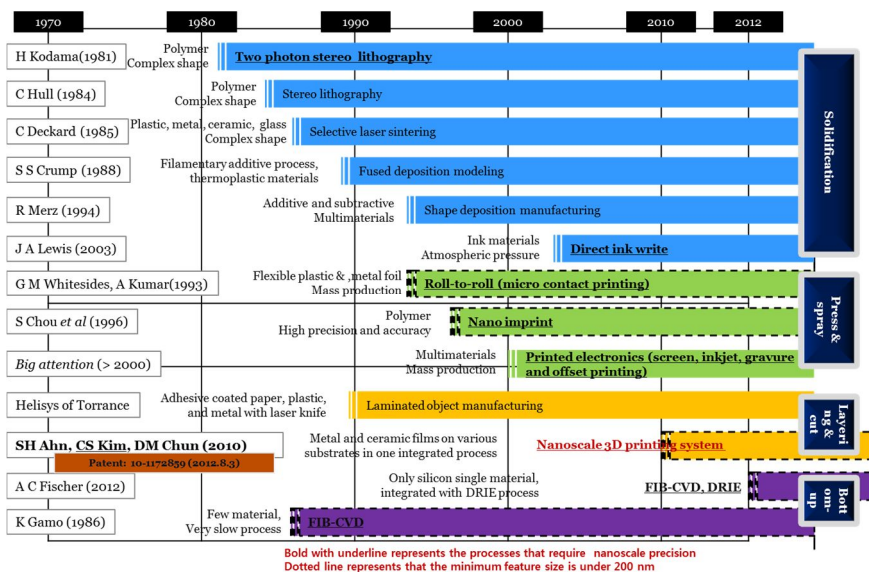


**Figure 1.2** Historical review of 3D printing technologies from the invention to the state-of-art



**Figure 1.3** Current three 3D printing technologies in micro- and nanoscale: (a) two photon lithography [15], (b) FIB-CVD [18] and (3) FIB & FIB-CVD & implantation [17].

**Table 1.1** Comparisons of current 3D micro- and nano printers

	Two photon lithography	FIB-CVD	FIB & FIB-CVD & Ion implantation
<b>Materials</b>	Polymeric materials	$\alpha$ -C, Pt and W	Si
<b>Multimaterials</b>	No	Few materials	No
<b>Min. linewidth</b>	> 250 nm	> 80 nm	> 80 nm
<b>Max. feature size (S)</b>	$20 \mu\text{m} < S < 500 \mu\text{m}$	$1 \mu\text{m} < S < 10 \mu\text{m}$	$1 \mu\text{m} < S < 100 \mu\text{m}$
<b>Functionality</b>	Still No	Can be functional	Can be functional

### 1.2.2 What is “*hybrid*” in manufacturing regime?

The terminology of “*hybrid*” implies at least three meaning as follows;

(1) **Type I: Convergence of ‘top-down’ and ‘bottom-up’:** In 2010, E B Brousseau *et al.* reviewed the advances in micro- and nano manufacturing processes [5]. In their review, they suggested new technological trends, convergence of top-down and bottom-up, from the previous article by E W Whatmore who is first introduced the convergence of top-down and bottom-up, as illustrated in Figure 1.4 [19]. Even though many researchers perceives that only atomic or molecular level process is categorized as ‘bottom-up’ process, but ‘*building-up*’ itself cab be categorized as ‘*bottom-up*’ process.

(2) **Type II: Convergence of ‘fabrication’ and ‘measurement’:** after machining mechanical parts in conventional manufacturing processes, the precision measurement should be done separately in order to evaluate the machined products. However, some manufacturing system can implement both works in only one system such as focused electron and ion beam assisted processes (called cross beam or dual beam system) [20, 21].

(3) **Type III: Convergence of more than one process:** this implies the combination and integration of manufacturing processes in order to increase the precision, accuracy, manufacturability and so on by taking individual process’s advantage. In terms of ‘*hybrid*’ concept, there are two different convergences; (a) process integration without simultaneously and (b) process integration with simultaneously. For example, some mechanical machining and energy beam process can be helped by the ultrasonic vibration or electro discharge machining can be integrated with both turning and grinding

processes.

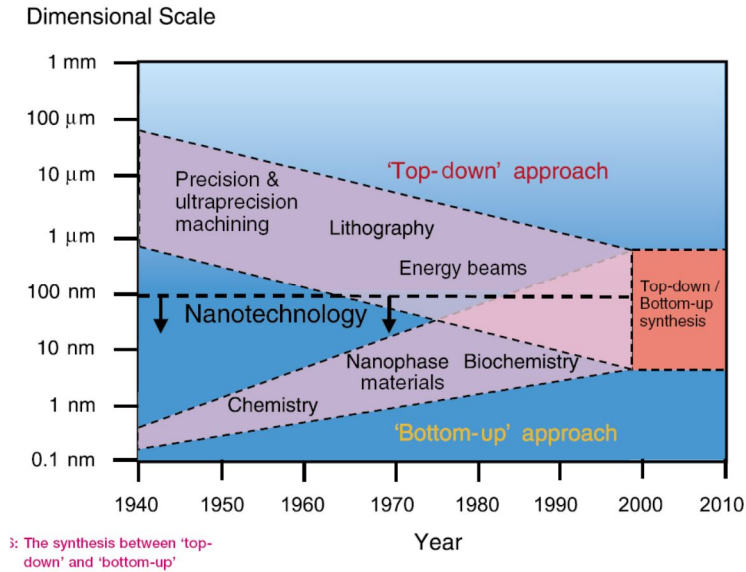


**Figure 1.4** Convergence of 'top-down' and 'bottom-up' nanotechnology for the next generation nanomanufacturing process [5, 19].

In terms of 'hybrid', there were several approaches in the manufacturing regime, as shown in Table 1. 2. This table contains characteristics of each manufacturing technologies, including precision, size, and 3D complexity of shapes and so on. It is very noticeable that there is the tremendous gap between mechanical and recent nanotechnology based manufacturing processes. It means that each processes has limitations which can be overcome each other.

**Table 1.2** Current hybrid manufacturing technologies

Hybrid manufacturing process	Precision	Resolution	Size	Temperature	Multimaterials	3D complexity
Laser + chemical [22-25]	⊙⊙⊙	⊙⊙⊙	⊙⊙⊙⊙	⊙	⊙⊙	⊙⊙⊙
Grinding + electrochemical [26]	⊙⊙⊙	-⊙⊙⊙	⊙⊙⊙	⊙	⊙	⊙⊙
EDM + grinding + drilling [27, 28]	⊙⊙⊙	⊙⊙⊙	⊙⊙⊙	⊙	⊙	⊙⊙⊙⊙
EDM + grinding [29]	⊙⊙⊙	⊙⊙⊙	⊙⊙⊙	⊙	⊙	⊙⊙⊙
Laser + ultrasonic vibration [30]	⊙⊙⊙	⊙⊙⊙	⊙⊙⊙⊙	⊙	⊙⊙	⊙⊙⊙
EDM + ultrasonic [31]	⊙⊙	⊙⊙	⊙⊙⊙	⊙	⊙	⊙⊙⊙
EDM + drilling [32]	⊙⊙	⊙⊙	⊙⊙⊙	⊙	⊙	⊙⊙⊙
Focused electron & ion beams [20, 21, 33]	⊙⊙⊙⊙	⊙⊙⊙⊙	⊙⊙	⊙⊙⊙⊙	⊙⊙	⊙⊙⊙⊙

⊙⊙⊙⊙: Best, ⊙⊙⊙: Good, ⊙⊙: Normal, ⊙: Bad

### 1.3 Recent advances in micro/nano manufacturing processes

There are lots of new manufacturing processes whether they are independent process or dependent processes (a hybrid or an integrated or an assisted processes), as listed in Table 1-3 and [8]. Particularly in Table 1.3, it shows the some representative advanced nanomanufacturing processes which can lead the innovation, and it tells even though many kinds of manufacturing process has been introduced, still there are big empty space to cover up the entire envelope of manufacturing needs by satisfying a precision, an accuracy, a scalability, manufacturability and so on.

**Table 1.3** The next generation manufacturing technologies for 3D nanostructures

Institute	Process	Character	Focus
Companies	Focused electron & ion beam system	Min. resolution: 10 nm	Fabrication & measurement
Cardiff University	Multibeam lithography	High throughput	Throughput
KTH Royal Institute of Technology [17]	FIB & FIB-CVD & ion implantation	Type I & II & III Min. line width 33 nm Limited scale < 20 $\mu\text{m}$ Only single material	“Top-down” & “bottom-up” Fabrication & measurement One more processes
UC Berkeley (SINAM) [34]	Plasmonic imaging nanolithography & nano imprint & self-assembly	Type II & III hybrid Min. resolution: 10 nm	“Top-down” & “bottom-up” One more processes
University of Illinois at Urban-Champaign [35]	Electro hydrodynamic jet printing	Metal and polymer Only dot and line pattern	Printing technology
University of Illinois at Urban-Champaign [36]	Direct ink write	3D nanostructure but filamentary	3D structure Multimaterial
V. B. Aleskovskii (inventor) & Suntola [37, 38]	Atomic layer deposition	0.1 ~ 0.3 $\text{\AA}$	Resolution
University of Michigan, Ann Arbor [39]	Roll-to-roll (roll-to-plate, nanoimprint)	Mass production	Mass production
University of Maine [40]	Scanning probe microscopy based lithography	1.5D	Resolution

KIMM (Korea Institute of Machinery and Materials), UCB (University of California at Berkley), UIUC (The University of Illinois at Urbana-Champaign)

## 1.4 Development of nanoscale 3D printing process

It remains a challenge to researchers to control the precision, accuracy, dimensional complexity, scalability, usability of multimaterials and processing conditions including high temperatures and wet environments even after development of numerous manufacturing processes as presented in Table 1.2 and 1.3. Among these issues, the usability of multimaterial restricts the functionality of structures and devices in the nanoscale manufacturing regime.

Especially, three nano printing processes which were pointed out previously have a big obstacle of the multimaterial availability and the functionality.

Therefore, nanoscale 3D printing process by integrating nano particle deposition system (NPDS) and focused ion beam (FIB) was proposed and developed to minimize the restriction of previous processes. Figure 1.5 illustrates the coverage of this new manufacturing process in current manufacturing envelope. For the development of nanoscale 3D printing process, first, the manufacturing systems were constructed, and then the each manufacturing process, both NPDS and FIB, was tested to check the feasibility as a 3D printing process. The material related issues and applications were investigated and fabricated as following sections.

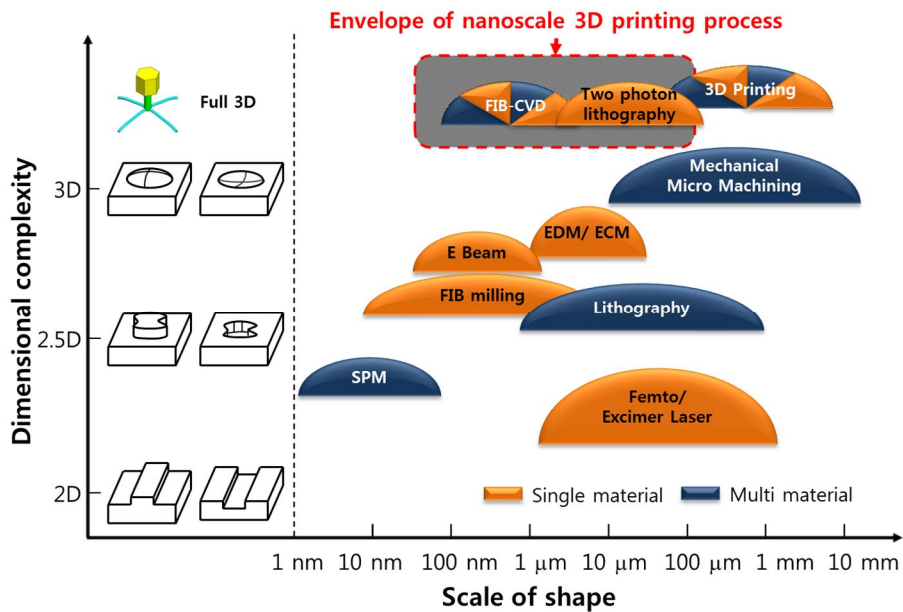


**Figure 1.5** The nanoscale 3D printing process in the manufacturing processes with the consideration of a dimensional complexity and a scale of shape

## 2 Process design and system integration

### 2.1 Conceptual design

As the 3D nano printer aimed to 3D nanostructures with multimaterials, the manufacturing process had to take into consideration on 1) capability of hybrid manufacturing from top-down and bottom-up, 2) availability of multimaterials with metals and ceramics (metal oxides), 3) achievement of 3D nanostructures with high degree of complexity, 4) stability as a green manufacturing process without chemical contents, and 5) manufacturability with short manufacturing process and time, for the advanced 3D nanomanufacturing process.

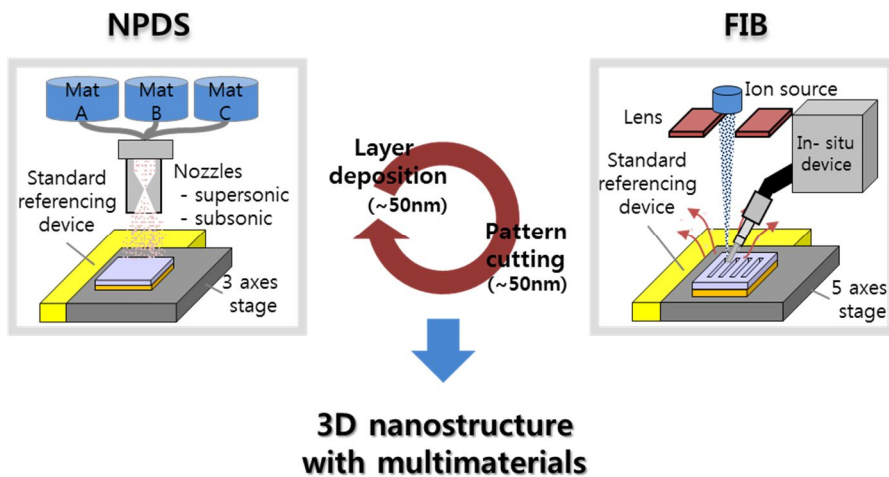


**Figure 2.1** Conceptual description for nanoscale 3D printing process integrated by both NPDS and FIB

## 2.2 Design of nanoscale 3D printing process

As the nanoscale 3D printing process, the hybrid manufacturing process had been newly introduced in [41] by integrating two processes of NPDS and FIB, as shown in Figure 2.1. Each processes roles' are material addition and removal, respectively. Specific roles of each process will be explained as follows.

### 2.2.1 Nano particle deposition system (NPDS)

The NPDS had been successively developed in 2008 by *Professor Sung-Hoon Ahn* in Seoul National University [42, 43]. This NPDS has been introducing for the fabrication of both metal and ceramic films by spraying micro- and nano-sized particles at room temperature under low vacuum condition ( $> 25$  Torr). This process was aimed to fabricate the both metals and ceramics in only one process by increasing particles' velocity using supersonic nozzle. Basically, this NPDS consists of an air compressor, powder feeder, vacuum chamber, and vacuum pump, as shown in Figure 2.2. Through NPDS, various materials, including Sn [44], Ni [45],  $\text{TiO}_2$  [42, 44], and  $\text{Al}_2\text{O}_3$  [46], had been deposited on various substrates.

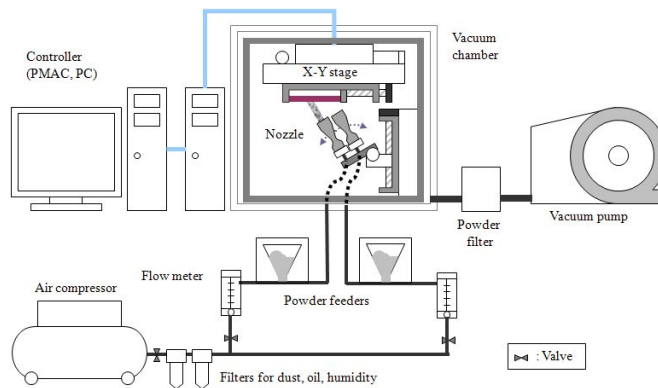


**Figure 2.2** Description of NPDS [47].

## 2.2.2 Focused ion beam (FIB)

The FIB has been utilized three decades ago for the application of micro surgery of integrated circuit by repairing its interconnection [48-50]. Nowadays it has been proven the capability of nanostructuring and applying nanostructuring of functional devices such as nanomanipulators [18, 51], micro- and nano lens [52], photonic devices [53, 54] and so on, and preparing transmission electron microscope (TEM) lamellas [55] and reconstructing 3D micro- and nanostructure for material sciences [56-59], particularly in biological samples [60-62]. This FIB system consists of an ion source, ion focusing electrodes, scanning electrodes, a processing chamber, a detector, a gas injection system, a sample stage, and an evacuation system, as shown in Figure 2.3. Through entire set of components, the FIB system can perform at least four functions, including milling, imaging, implantation and deposition (with the help of gas injection system, optionally equipped with FIB system)

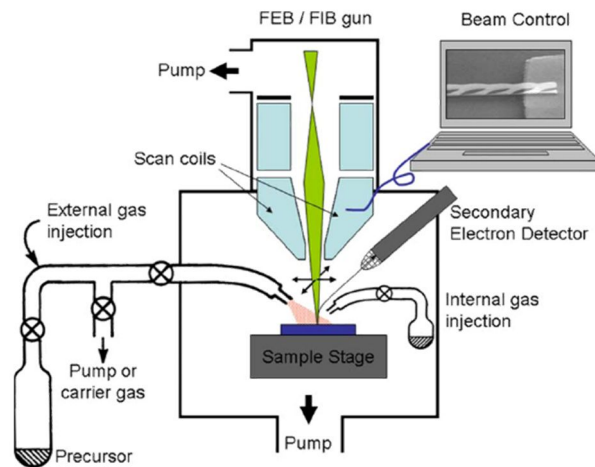


**Figure 2.3** Description of FIB system [63]

### 2.2.3 Nanoscale 3D printing process

Figure 2.4 is a process flow chart of the nanoscale 3D printing process for 3D parts with multimaterials. Based on the 3D design, the process planner will slice the part, and create layers. Each layer has different profile and materials including real part and supporter part. Based on this information, material for deposition will be selected and layer deposition will be carried out by NPDS. And the profile cutting will be performed by FIB. By repeating layer deposition and profile cutting, the 3D structure can be fabricated. Finally, a nanoscale 3D part can be produced after removing supporters and final profile cutting.

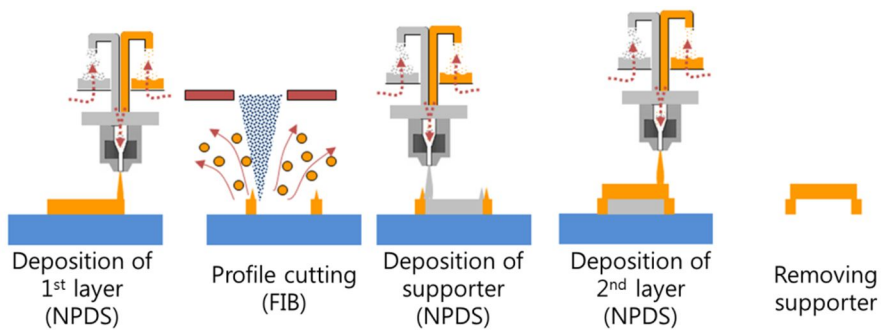


**Figure 2.4** Process flow of nanoscale 3D printing process

### 2.3 Design for functionality

For the development of nanoscale 3D printing process, FIB and NPDS will be essentially required for each subtractive and additive process basically. It is important to define the functionality in the design level for manufacturing process and system. Thus, the functionality of each process was defined as following.

### **2.3.1 Functions for NPDS**

- Thin film coating with various thicknesses
- Precision 3-axes positioning and referencing
- Other components can be expandable to increase the functionality of NPDS: multi-nozzle, vacuum annealing and so on.

### **2.3.2 Functions for FIB**

- Nanostructuring and imaging of target surface: decelerated image can also be possible for reduce the sample damage such as ceramic and polymeric materials by applying the bias voltage onto the sample holder
- Ultra precision 5-axes positioning: XYZRT should be operated in order to find the sample in the eucentric position, and tilt angle should be contained to check the cross-sections of sample thickness.
- Ultra precision and accuracy of referencing: with the combination of both imaging by FIB and positioning by stage, the ultra-fine precision can be done.
- Material property measurement: mechanical and electrical properties
- Other components can be expandable to increase the functionality of FIB system: charge neutralization, gas injection system and so on.

## **2.4 Development of system**

### **2.4.1 Nano particle deposition system (NPDS)**

As mentioned previous section, the NPDS can make thin coating layer through dry spray method under low vacuum and low temperature condition. As shown in Figure 2.2 previously, NPDS consists of controller, deposition chamber with substrate holder and nozzle, powder supplier, air compressor,

and vacuum pump, etc. The pressure condition of deposition chamber is maintained in atmospheric pressure condition to increase the economic feasibility and productivity.

## **2.4.2 Focused ion beam (FIB)**

In order to act as FIB for nanofabrication, mainly four components will be required; (1) FIB column, (2) secondary electron detector (SED), (3) eucentric stage and (4) main processing chamber with the evacuation system. In this section, the role of each component will be described.

### **2.4.2.1 FIB column**

The FIB column contains ion source, two electrostatic lens (condenser and objective lenses), octapole beam deflector and stigmator, beam blanker, and variable aperture system. The COBRA FIB column (Orsay Physic, France) was adopted for the nanoscale 3D printing system [64]. The brief specification of FIB column is followed; (1) acceleration voltage: 1 ~ 30 kV continuously, (2) ion species: gallium, (3) beam resolution: < 2.5 nm, probe current: 1 pA to more than 50 nA, number of apertures: 13, and bakeout temperature: 170 °C.

### **2.4.2.2 Secondary electron detector (SED)**

The FIB can do make an image like scanning electron microscope (SEM) by scanning the focused ions onto the targeted area where we want to see because ion-solid interaction also can generate the secondary electron from the solid target. By collecting secondary electrons, the FIB can image nanostructures. The Everhart-Thornley type SED was utilized in this system

[64]. This SED adjusts parameters, including collector voltage, accelerating voltage, brightness and contrast.

### 2.4.2.3 High vacuum compatible 5-axes eucentric stage

The roles of stage in FIB system itself and nanoscale hybrid manufacturing system are to position the sample surface accurately even in tilting motion, fix the sample tightly without mechanical vibration for high resolution imaging, make a reference when stacking multilayers with high accuracy of overlay.

Unlike SEM, of course, the role of stage is much more important because many FIB fabrication and analysis can be finished with certain angles. Therefore, the 5-axes with eucentric function are the most powerful function by keeping the working distance (objective lens to sample distance) even in tilting motion. Further, many FIB systems tried to adopt the micro probing system for TEM sample preparation. When preparing TEM sample, the eucentric tilt motion is also essential. The 3D model for 5-axes eucentric stage (SNU-UST-5100) was shown in Figure 2.5.

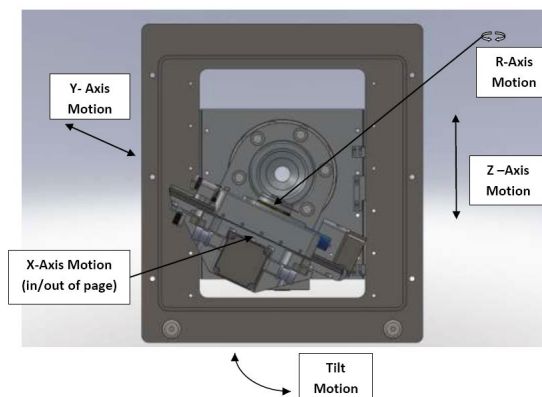


**Figure 2.5** Backside view of vacuum compatible 5-axes eucentric stage looked from the rear of chamber towards the front door to show how the 5-axes motion plays

### 2.4.2.4 Main processing chamber

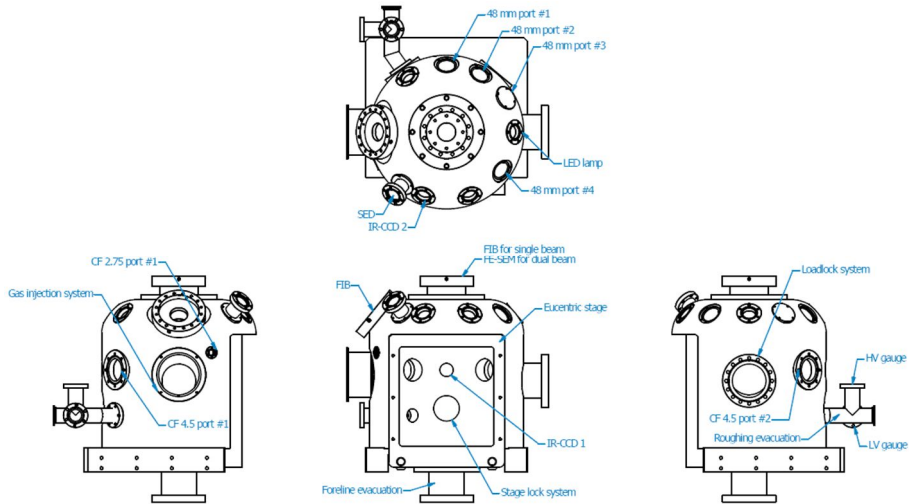


**Figure 2.6** Accessible port configurations for multifunctional nano production in FIB system

**Table 2.1** Basic and optional components for the design of the main processing chamber

	FIB	SEM	SED	Mono GIS	GIS-5	CN
<b>Model</b>	Cobra	Eclipse plus	ETD	Mono GIS	GIS-5	EKF
<b>Manufacturer</b>	Orsay Physics	Orsay Physics	Orsay Physics	Orsay Physics	Orsay Physics	Omicron
<b>Length</b>	240.50	239.25 (239.5)	276.3	283.021+25 310.088	282.247±12 (282.5)	188 254
<b>Angle</b>	0	-51	40	-	Adjustable	-
<b>Working distance (mm)</b>	12	12	33 (35)	< 0.2	< 0.2	66
<b>Port</b>	ISO63	ISO63	CF2.75	ISO63	CF2.75	CF2.75

The main processing chamber design is very critical to not only have a multi-functionality of FIB system but also connect the NPDS for hybrid manufacturing process. Basically, this main chamber also has to protect the mechanical and acoustic vibrations, and electromagnetic field.

As shown in Figure 2.6, the main processing configures lots of port for the integration of various functional components such as micro probing system, gas injection system, and so on.

One of the important points for vacuum chamber is the material for high vacuum condition under  $1.0 \times 10^{-6}$  Torr. A primary concern is that the amount of gas released under high vacuum conditions must be as small as possible. Thus, materials with a porous structure that can harbor gas, or others with flawed structures due to cracking on a microscopic scale, or that are otherwise permeable to gas, are not permissible. Materials that can be used must have adequately small outgassing rates after cleaning treatments, must be stable over the range of temperatures encountered, and must exert an insignificant vapor pressure. Mechanically, they should have adequate strength and be easy to fabricate into the shapes required. Techniques must be available for joining them to other parts of the same material and to other vacuum compatible materials.

For the vacuum chamber, austenitic stainless steel, aluminum, and glass are good materials in all the above respects. Especially, stainless steel with low carbon content and nickel and chromium content of around 18 and 8%, respectively, and members of the “300” series (304, 316, and 321, in particular) are strong, tough, and versatile, with good machining and welding properties, and good corrosion resistance and outgassing characteristics on account of the stable chromium oxide layer that forms on their surfaces. They are also nonmagnetic, though occasionally their joins may acquire some magnetism as a result of welding. The use of ‘L’ grades helps to minimize this if it is a potential problem. However, in the part of main chamber the ultra high vacuum below  $1.0 \times 10^{-9}$  Torr does not require. Therefore, the stainless

steel 304, not stainless steel 304L, was adopted to build the main chamber here. On the basis of main processing chamber design the FIB system was assembled as shown in Figure 2.7.

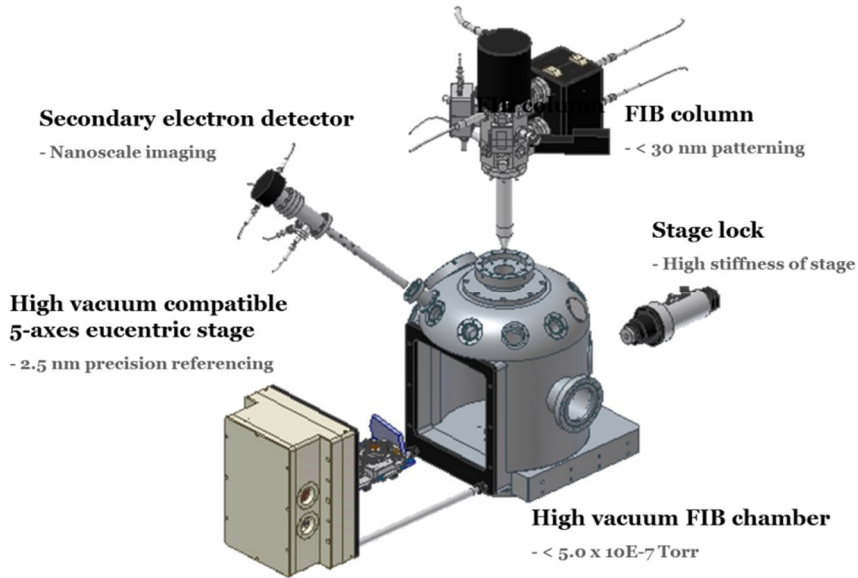


**Figure 2.7** Assembled 3D model of FIB system

#### 2.4.2.5 Evacuation system

The FIB system requires differential vacuum status between ion source and main chamber. In parts of ion sources and main chamber, the vacuum status should be satisfied in the range of  $< 7.5 \times 10^{-7}$  Torr and the  $7.5 \times 10^{-6}$  Torr, respectively.

In order to achieve the differential high vacuum, rotary pump (RP), turbo molecular pump (TMP) and two ion pumps (IP1 and IP2) combination were adopted. After assembling the main process chamber with other vacuum components like RP, TMP and vacuum valves without FIB column, SED and stage. The bake-out process had been implemented for total 5 times with the

temperature of 150°. The known leak rate of stainless steel is around  $1.5 \times 10^{-8}$  mbar l/sec·cm<sup>2</sup> (5 hours after 24 hours 150 ~ 250 °C).

Through the series of evacuation test, the maximum achievable vacuum status was  $5.5 \times 10^{-8}$  Torr at the main processing chamber. Its value was better than what it was expected because recent vacuum pumping devices has been improved its operational performances. After assembling of FIB column, SED and stage, its maximum vacuum pressure was kept even though it took more time.

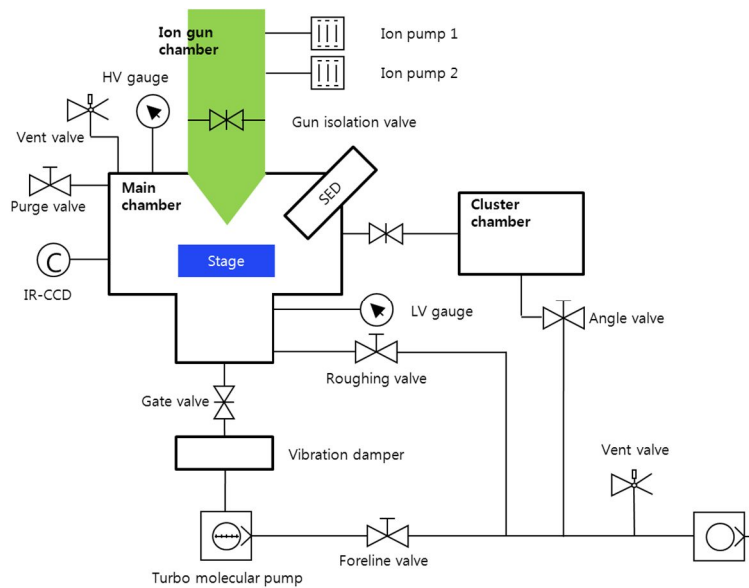


**Figure 2.8** Description of evacuation system for FIB system

## 2.5 Integration of FIB system

Finally the FIB system where placed in Seoul National University was constructed as shown in Figure 2.9. And Figure 2.10 shows the inside of the main processing chamber by the infrared charged coupled device (IR-CCD) camera. The specification of FIB system was shown in Table 2.1.

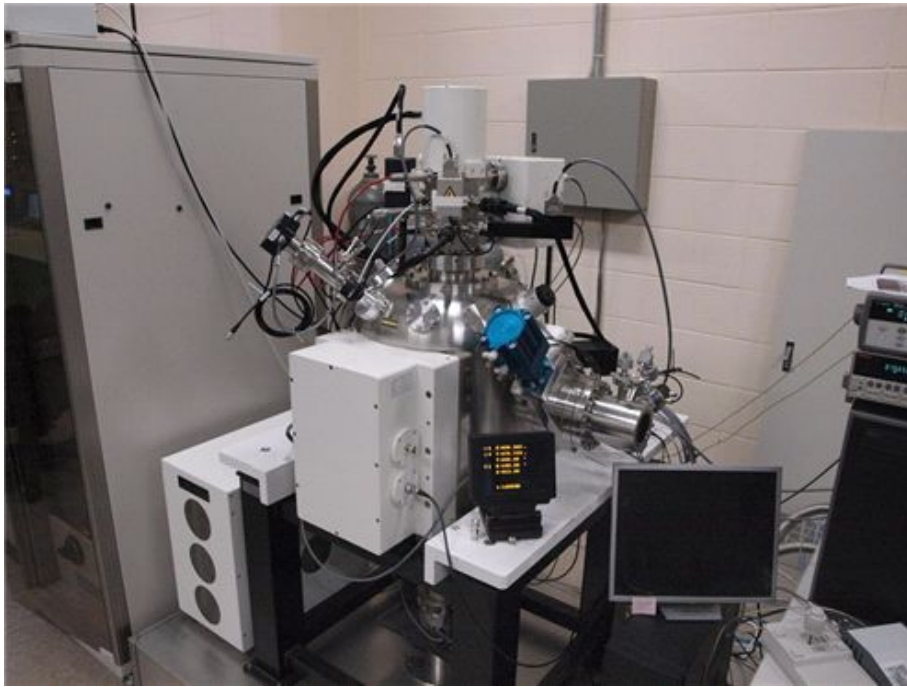


**Figure 2.9** Assembled FIB system placed in Seoul National University



**Figure 2.10** Inside of the main processing chamber and assembled components taken from IR-CCD camera

**Table 2.2** Specification of FIB system

Category	Specifications	
<b>Ion beams</b>	Acceleration voltage	1 ~ 30 kV
	Probe current	1 pA ~ 50 nA (13 apertures)
	Resolution	2.5 nm @ 1 pA of probe current and 12 mm of working distance
<b>Stage</b>	Travel	X, Y: 100 mm, Z: 50 mm, R: 360, T: -10~60
	Repeatability	X, Y: 1 $\mu$ m
	Resolution	2.5 nm (joystick)
<b>Detection</b>	Everhart-Thornley type	2 <sup>nd</sup> electron
<b>Imaging</b>	Milling & Imaging S/W	MISS and Elphy Quantum
		Port for user interface
<b>Evacuation system</b>	Evacuation system	RP, TMP, IP (2)
	Operating vacuum	2.0E-7 Torr for specimen chamber & 1.3E-8 Torr for ion gun chamber
<b>Additional</b>	IR-CCD Navigation	
	Decelerated imaging mode	
	Various micro/nano manipulator & systems can be assembled	

## 2.6 Essential requirements for nanoscale 3D printing process

The essential four representative geometries were defined as an objective to fabricate the 3D nanostructures with multimaterials. This is shown in Figure 2.11. From these representative geometries the feasibility and capability of nanoscale 3D printing process by both NPDS and FIB will be verified as following sections.

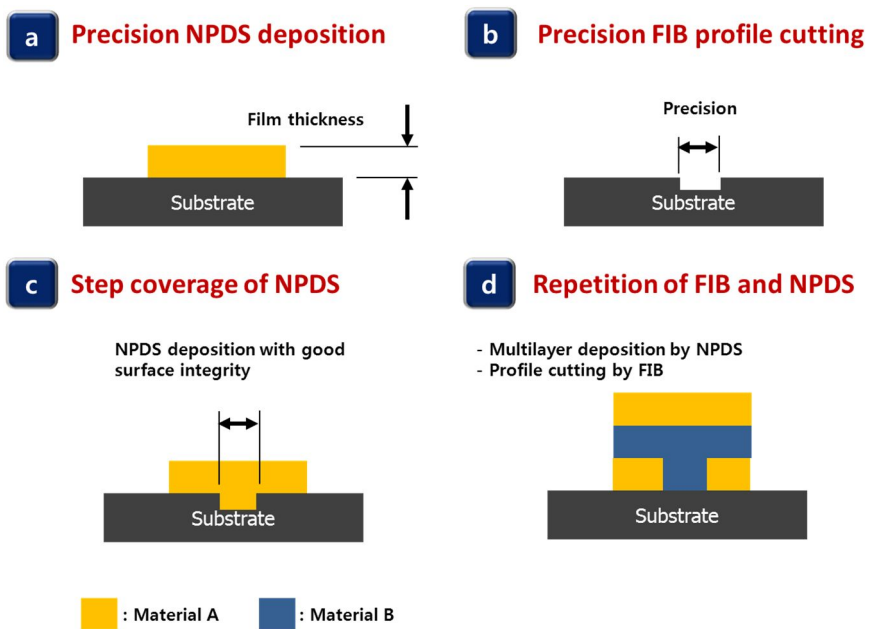


**Figure 2.11** The representative target geometries for the performance verification of nanoscale 3D printing process

# 3 Nanostructuring by NPDS

## 3.1 Overview

The NPDS was developed to compare with the cold spray technique and the aerosol deposition as a part of particle spray deposition. NPDS was found to have strong potential to deposit multimaterials in one system with some unique advantages over the cold spray and aerosol deposition [42, 47, 65, 66]. However, it is need to weigh with the state-of-art technology for the verification of current status of technology. In the field of material additive process, the atomic layer deposition (ALD) has been receiving most attentions as the promising technology with its usability of multimaterials and thickness resolution. In order to explain the advantages of NPDS over the ALD (thin film processing), Table 4.1 was presented for the comparison of process between ALD and NPDS.

**Table 3.1** Comparison between NPDS and ALD

Category	ALD	NPDS
Resolution	> 0.01 nm	100 nm
Temperature	100~500 °C	Room temperature
Rate	0.027 nm/sec	25 um/sec
Material	Metal/ceramic	Metal/ceramic
Substrate	Metal/ceramic/polymer	Metal/ceramic/polymer
Uniformity	Good	Not good
Environmental	Chemical residue	Friendly
Character	Mass production	Maskless direct writing

With comparison of ALD, NPDS have benefits of the availability of multimerials, the processing rate and the capability of direct writing without mask. The only limitation of NPDS is the uniformity of thin film and if solved properly, it must be an innovative technology for the thin film process regime.

For several years after the invention of NPDS, precision nanostructuring by NPDS had been investigated in the literatures, as shown in Table 3.2. Except for Table 3.2, Table 3.3 shows all of work had been implemented (some materials combinations are not reported).

**Table 3.2** Progresses on deposition by NPDS

Year	Materials/Substrate	Reference
2012	TiO <sub>2</sub> /(ITO-Glass and ITO-PET)	[67]
2012	Al <sub>2</sub> O <sub>3</sub> /Sapphire	[68]
2011	Sn/Silicon and Al <sub>2</sub> O <sub>3</sub>	[41]
	Al <sub>2</sub> O <sub>3</sub> /Sn	
2011	Al <sub>2</sub> O <sub>3</sub> /Sapphire	[65]
2011	TiO <sub>2</sub> /(ITO-glass)	[69]
2010	Al <sub>2</sub> O <sub>3</sub> /(Cu and Al)	[46]
2010	Ni/Silicon	[70]
2010	Sn/(PCB, PP, PET)	[47]
	Sn/(Glass, Sapphire)	[47]
	Sn/Paper	[47]
2008	TiO <sub>2</sub> /(Cu, Al, SUS)	[42]
2008	TiO <sub>2</sub> /PET, PE, ITO-PET	[44]

As seen in both tables, lots of metal and ceramic particles were deposited onto various substrates, including polymer, metal, ceramic and paper. However, most of works list in Table 3.2 were focused on the feasibility of various material deposition on different substrates and applications.

In this section, thus, the precision issue will be dealt with multimaterials such as metal (tin, Sn) and ceramic (titanium dioxide, TiO<sub>2</sub> and aluminum oxide, Al<sub>2</sub>O<sub>3</sub>). Especially in the value of thickness, namely, thickness resolution (Figure 2.11(a)) on substrates will be shown. Moreover, the physical properties such as the film strength (hardness and elastic Modulus) and the bonding strength (peel-out test by adhesive tape and work of adhesion by contact angle) were investigated as an engineering film.

**Table 3.3** Multimaterial combinations by NPDS

		Polymer						Metal					Ceramic			Etc
		CFRP	PCB	PE	PP	PMA	PET	AISI304	AISI316	Cu	Al	Ni	Si	Al <sub>2</sub> O <sub>3</sub>	Glass	Paper
Ceramic	TiO <sub>2</sub>	(x)		(Δ)	(Δ)	(○)	(○)	○		○	○	(○)				(Δ)
	Al <sub>2</sub> O <sub>3</sub>							○		(○)	(○)					
	Mn-Zn ferrite										(○)					
Metal	Sn		○			○	○			(○)	(○)	○	○		○	○
	Ni		(Δ)	(Δ)		(Δ)	(Δ)						(○)			
	Al				(○)											
	Cu	(x)	(x)													
	AlN									(○)	(○)					

- x: No deposition, Δ: Powder attachment (not film), □: Film deposition with specific condition (carrier and heating), ○: Film deposition  
 - ( ): judged by only optical microscope, not by SEM, surface profiler, and FIB cross-sectioning

### 3.2 Process parameters

Success of NPDS is in selection of parameters such as material properties of particle, wide range of substrate, gas pressure, gas flow rate, and vacuum. Therefore, important process parameters should be selected carefully. Among the process parameters illustrated in Figure 3.1, carrier gas pressure, the vacuum level in deposition chamber, and the distance between nozzle and substrate are directly related to the impact velocity. The effects of these

selected parameters to the impact velocity had been studied by computational fluid dynamics, and the physical meanings of the results had been investigated in [71]. Here, two process parameters, those play the deceive role on the film thickness will be selected to check the deposition tendency. The two parameters were the feed rate and stand-off distance (SoD).

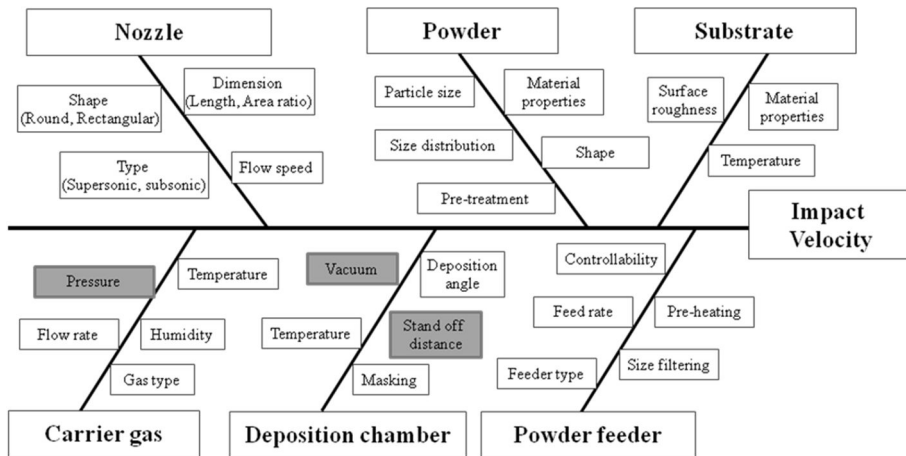


**Figure 3.1** Fish-bone diagram for particle deposition in NPDS [71].

### 3.3 Materials

#### 3.3.1 Metal: Tin, Sn

Tin (Sn) is a key material in the electronic devices, especially in soldering [47, 72, 73]. The use of lead in solders was prohibited and the ratio of tin has increased as alternatives made of Sn-Ag, Sn-Bi, Sn-Zn, and Sn-Cu have been developed [47, 74]. Unlike the use of compound materials for soldering materials, Sn itself can be applicable for other purposes. Tin bonds readily to iron and is used for coating lead or zinc and steel to prevent corrosion. Tin-plated steel containers are widely used for preservation of food and contribute to large portion of the market for metallic tin. Sn is also used as a negative

electrode in advanced Li-ion batteries. Its application is somewhat limited by the fact, that some tin surfaces catalyze decomposition of carbonate-based electrolytes used in Li-ion batteries [75].

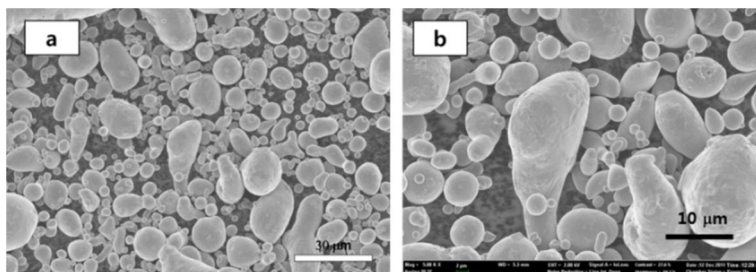


**Figure 3.2** FE-SEM images of virgin Sn particles: 2-20  $\mu\text{m}$  in diameters

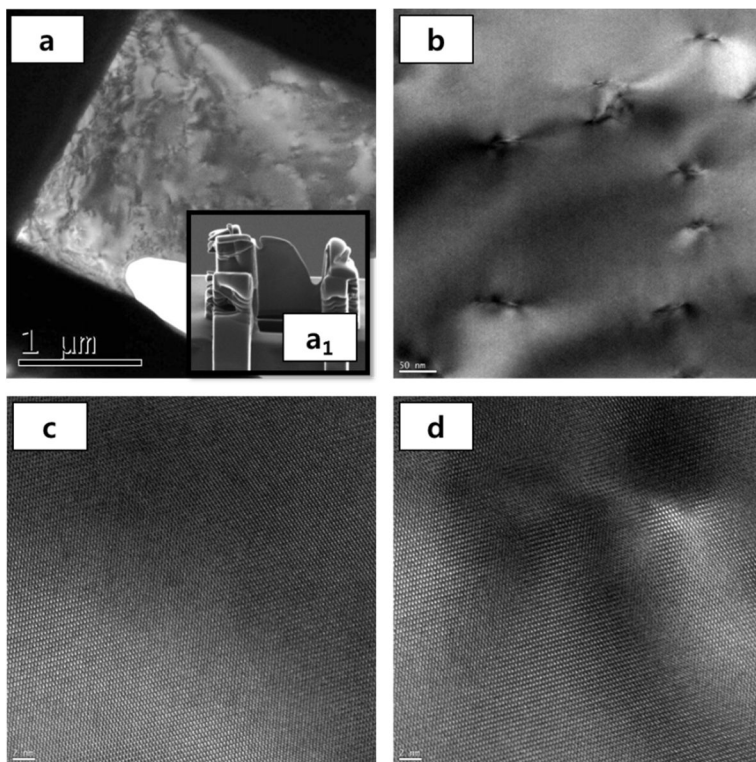


**Figure 3.3** HR-TEM images of Sn virgin particle: (a) TEM sample of Sn fabricated by FIB lift-off technique, (a<sub>1</sub>) SIM image of Sn TEM sample (60° tilt view), (b) Sn with dislocational defects (low magnification), (c) lattices of Sn without defects, and (d) lattices of Sn with dislocational defects.

Tin particles with diameters 2 ~ 20  $\mu\text{m}$  (Sigma-Aldrich) were used for metallic thin film, as shown in Figure 3.2 taken by field emission electron microscope (FE-SEM). In order to observe the microstructure of Sn particle, the high resolution transmission electron microscope (HR-TEM) analysis was taken to the virgin Sn particle, as shown in Figure 3.3. In Figure 3.3(a-b), there were lots of dislocation defects in a single Sn particle even though the defective structure did not appear in Figure 3.3(a<sub>1</sub>), scanning ion microscope (SIM) image of Sn TEM sample prepared by FIB lift-off technique. Figure 3.3(a) represents the contrast difference appeared by the dislocation in Sn metallic structures. Even though it had lots of dislocational defects, HR-TEM images showed that Sn particle had a single crystalline structure in Figure 4.3(c-d).

### **3.3.2 Ceramic: Titanium oxide, TiO<sub>2</sub>**

Preparation of TiO<sub>2</sub> thin films was attempted as these are extremely important in terms of corrosion protection, gas sensors, self-cleaning surfaces, photovoltaic surfaces, and capacitors because of their unique dielectric, and transparent ferromagnetic material properties with their highly chemical stability [76-81]. TiO<sub>2</sub> is also used as a material in the memristor, a new electronic circuit element. It can be employed for solar energy conversion based on dye, polymer, or quantum dot sensitized nano crystalline TiO<sub>2</sub> solar cells using conjugated polymers as solid electrolytes [69, 82, 83]. In 2010, researchers at the University of Tokyo (Japan) had created a crystal form of TiO<sub>2</sub> particle having a size of 5 to 20 nanometers that can be switched between two states with light. Use of the 5 nm particles could lead to a 25 TB storage disc theoretically [84].

Anatase TiO<sub>2</sub> nanoparticles (Nanoarmor) with diameters around 15 nm, known value from seller, were used for metallic thin film, as shown in Figure 3.4 and 5. In Figure 3.4 taken by FE-SEM the TiO<sub>2</sub> nanoparticles (15 nm)

were agglomerated in sizes of 200 nm to 800 nm. In order to check the particle size exactly, HR-TEM images were taken as shown in Figure 3.5. In this figure, not only the agglomerated  $\text{TiO}_2$  particles were found but also the crystalline  $\text{TiO}_2$  nanoparticles inside of them were identified through HR-TEM.

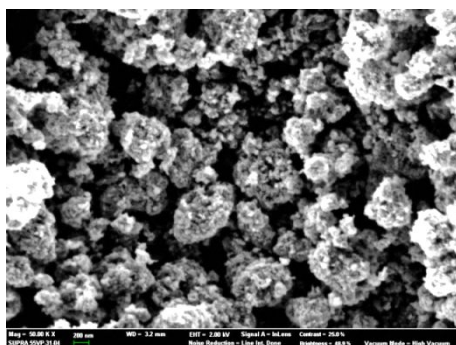


**Figure 3.4** FE-SEM images of  $\text{TiO}_2$  nanoparticles

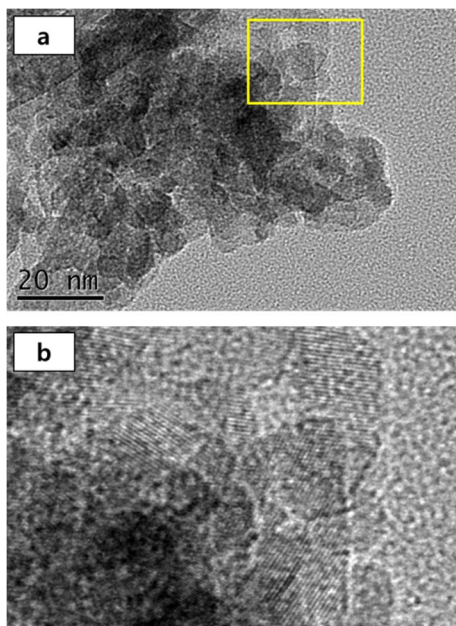


**Figure 3.5** HR-TEM images of  $\text{TiO}_2$  nanoparticles: (a) agglomerated  $\text{TiO}_2$  nanoparticles, and (b) crystalline  $\text{TiO}_2$  nanoparticles (detail view of box in Figure 3.5(a))

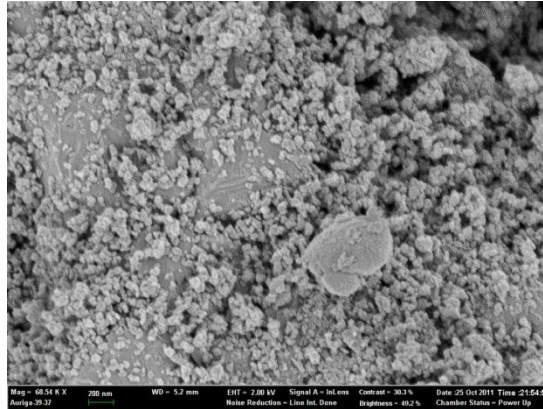


**Figure 3.6** FE-SEM images of Al<sub>2</sub>O<sub>3</sub> nanoparticles

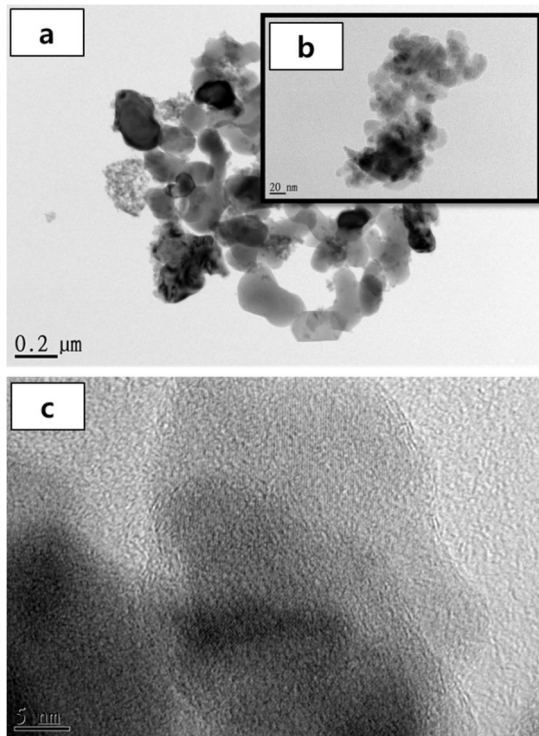


**Figure 3.7** HR-TEM images of Al<sub>2</sub>O<sub>3</sub> nanoparticle: (a) agglomerated Al<sub>2</sub>O<sub>3</sub> nanoparticles, (b) magnified view of 20 nm particles, and (c) crystalline structure of Al<sub>2</sub>O<sub>3</sub> nanoparticles

### **3.3.3 Ceramic: Aluminum oxide, Al<sub>2</sub>O<sub>3</sub>**

The Al<sub>2</sub>O<sub>3</sub> is another particle which has application in several areas due to its high hardness, high compressions strength, and resistances to abrasion, chemical attack, and thermal shock, high dielectric strength, bio-compatibility and so on [85-89]. With these superior properties, Al<sub>2</sub>O<sub>3</sub> coatings are widely used for catalyst, corrosion resistance film and so on [90, 91]. Al<sub>2</sub>O<sub>3</sub> is able to adopt as not only electrical insulators for integrated circuits but also as a tunnel barrier for the fabrication of superconducting devices such as single electron transistors and superconducting quantum interference devices.

Al<sub>2</sub>O<sub>3</sub> particles with diameters of 20 nm and 200 nm are used for ceramic deposition, as shown in Figure 3.6-7. The manufacturer is Contronics corp (New York, NY, USA). From Figure 3.7 of HR-TEM, it is identified that nanoparticles have two different sizes of around 20 nm and 200 nm.

## **3.4 Deposition of metal and ceramic films**

### **3.4.1 Overview**

Sn, TiO<sub>2</sub> and Al<sub>2</sub>O<sub>3</sub> particles were deposited on the silicon substrate. To evaluate the deposition tendencies of each particle, the effect parameters of feed rate and stand of distance (SoD) were controlled.

### **3.4.2 Experimental conditions**

With these experimental conditions, the deposition experiments were implemented three times for each particle on silicon (100) substrate. Two effective parameters of the feed rate and SoD were investigated here. The experimental conditions are listed in Table 3.43. And Figure 3.8 explains two

parameters.

**Table 3.4** Experimental conditions of NPDS for Sn, TiO<sub>2</sub> and Al<sub>2</sub>O<sub>3</sub>

Parameter	Value
Carrier gas	Air
Relative air pressure (MPa)	0.3
Vacuum (MPa)	-0.095
Powder feeder	TSI 3400A
Feed rate ( $\mu\text{m}/\text{sec}$ )	25, 50 and 100
SoD (mm)	2, 3 and 4

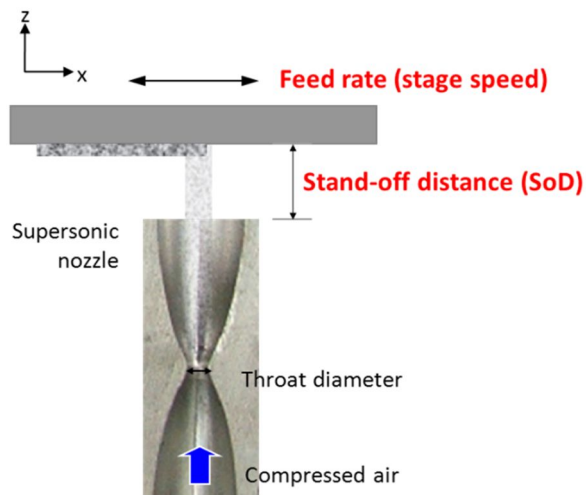


**Figure 3.8** Description of two parameters, the feed rate and SoD, in NPDS

### 3.4.3 Films thicknesses of metal and ceramic

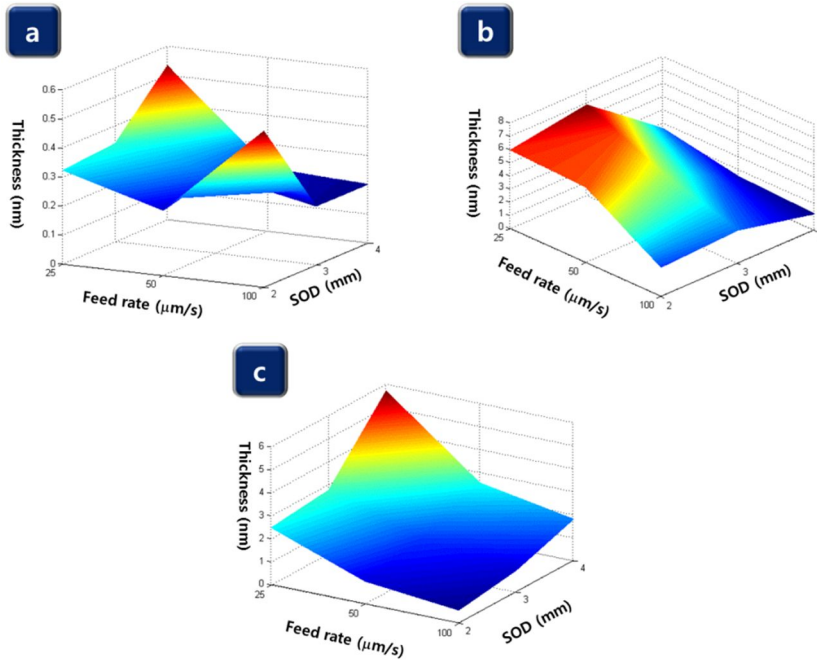


**Figure 3.9** Film thicknesses of metal and ceramic films: (a) Sn, (b)  $\text{TiO}_2$  and (c)  $\text{Al}_2\text{O}_3$  as functions of the feed rate and SoD

Figure 3.9(a-c) represents the deposition results of three particles of Sn,  $\text{TiO}_2$  and  $\text{Al}_2\text{O}_3$ , respectively. In Figure 3.9(a), overall Sn films were not formed with uniform tendency. This non-uniform tendency might be generated by the variances of particle sizes in the range of  $2 \sim 20 \mu\text{m}$ . These observations indicated that that random sized particle within above ranges can be flowed into the air tube and nozzle. Particularly, random sized particles might be critically influenced by the nozzle which causes the supersonic flow velocity. The flow velocity and the impact velocity were greatly governed by the particle size in [92]. However, there was one unique characteristics of deposition. Especially in Sn films, when the feed rate of  $50 \mu\text{m/s}$  was applied the uniform thicknesses were formed without influence of SoD. Generally the

higher thicknesses of Sn particle were formed when slow feed rates were applied.

In Figure 3.9(b), the lower feed rate was applied, the higher TiO<sub>2</sub> film was formed. Lowering of feed rate means that the large number of particles was supplied onto the substrate. Thus, the thickness of TiO<sub>2</sub> films was directly influenced by the particle supply concentration. The lower SoD was applied, the higher TiO<sub>2</sub> film was formed. It explains that the lower SoD prevented the loss of flowed particles at the exit of nozzle when impacting with the substrate.

In Figure 3.9(c), the higher feed rate was applied, the lower Al<sub>2</sub>O<sub>3</sub> film was formed like TiO<sub>2</sub> film. The higher SoD was applied, the higher Al<sub>2</sub>O<sub>3</sub> film was formed in contrast to the TiO<sub>2</sub> film.

For each case, the minimum thickness of Sn, TiO<sub>2</sub> and Al<sub>2</sub>O<sub>3</sub> films were 202 nm, 505 nm and 1,800 nm, respectively.

**Table 3.5** Physical properties and their measurement method

Category	Property	Method
Strength of film	Hardness	Nanoindentation
	Elastic Modulus	
Bonding of film	Adhesion	Peel-out by tape
	Work of adhesion	Contact angle
Microstructure of film	Phase	XRD

### 3.5 Characterization of metal and ceramic films

#### 3.5.1 Overview

The success of any technique depends on the application of resulting films as engineering films. Therefore, films deposited by NPDS were examined

with physical properties such as bond strength, phase transition, strength of film and so on. In order to characterize physical properties of films deposited by NPDS, here, the several analytical techniques were utilized as shown in Table. 3.5.

### 3.5.2 Strength of films

For the verification of the strength of films, including Sn, TiO<sub>2</sub> and Al<sub>2</sub>O<sub>3</sub>, the MTS XP (MTS Systems Corporation Inc.) was utilized. It has the maximum load of 500 mN and resolution of 50 nN. The Vickers hardness and elastic Modulus were measured by nanoindentation. For the quantitative comparison, mechanical properties (hardness and elastic Modulus) of bulk material and thin film formed by other thin film processing were investigated as shown in Table 3.6. Even though three films were not formed in the atomic and molecular level, they showed quite good hardness and elastic modulus.

**Table 3.6** Hardness and Elastic Modulus of metal and ceramic films

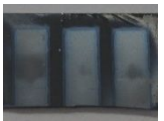
Material	Property (GPa)	Bulk	Thin film (NPDS)	Thin film (Other processes)
Sn	Hardness	350	0.613	-
	Elastic Modulus	50	24.397	-
TiO <sub>2</sub>	Hardness	880	0.238	0.1 (PVD) [93] 4.0 (CVD) [94]
	Elastic Modulus	230	5.687	20.0 (PVD) [93]
Al <sub>2</sub> O <sub>3</sub>	Hardness	1,175	0.024	9.5 (PVD) [95] 12.3 (ALD) [96]
	Elastic Modulus	300	3.456	150 (PVD) [95] 12.3 (ALD) [96]

PVD (physical vapor deposition), CVD (chemical vapor deposition) and ALD (atomic layer deposition)

### 3.5.3 Bonding of films

The bonding force between film and substrate should be verified to check the availability as an engineering film in the criteria of thin films. In thin films, the nanoscratch test is very usual. However, the scratch tip can be contaminated or damaged in case of films deposited by NPDS because their formation is somewhat different, not perfect solid like CVD or PVD films. Thus, two methods, the peel-out by adhesive tape and the contact angle measurement, were utilized for the definition in qualitatively and quantitatively.

**Table 3.7** Peel-out test by adhesive tape

	Before peeling	After peeling (1 time)		After peeling (30 times for Sn and Al <sub>2</sub> O <sub>3</sub> and 10 times for TiO <sub>2</sub> )	
Sn					
TiO <sub>2</sub>					
Al <sub>2</sub> O <sub>3</sub>					

#### 3.5.3.1 Peel-out test by adhesive tape

The adhesive tape is very useful and easy to qualify the bonding force of thin film. Here, the qualitative analysis by adhesive tape was performed for Sn, TiO<sub>2</sub> and Al<sub>2</sub>O<sub>3</sub>. Except for TiO<sub>2</sub> film, Sn and Al<sub>2</sub>O<sub>3</sub> films represented the

good adhesive performances, as shown in Figure 3.7. After detaching 30 times the adhesive tape from the films, only the small amount of particles was torn off. In case of Sn, few particles were detached from the film. In case of Al<sub>2</sub>O<sub>3</sub>, most of detached particles were at the first detachment test, and after first detachment only few particles were removed from the film. In contrast to TiO<sub>2</sub>, it did not represent the good bonding quality. Half of particles in the film were removed from the film after 10 times detachment.

### 3.5.3.2 Work of adhesion

The work of adhesion using the contact angle measurement was implemented to quantify the adhesion of films deposited by NPDS.

Theory of contact angle of liquid droplet on a flat surface in terms of Equation 3.1 set by Young [97].

$$\sigma_{sv} - \sigma_{sl} = \sigma_{lv} \cdot \cos \theta \quad \text{Equation 3.1}$$

where  $\sigma$  refers to the interfacial tension and the subscripts  $sv$ ,  $sl$  and  $lv$  indicate solid/vapor, solid/liquid and liquid/vapor interfaces, respectively.

Equation 3.1 was improved by Dupre (Young-Dupre equation,) to give the work of adhesion, which means that the work required making a separation of the liquid from the solid (Equation 3.2).

$$W_{sl} = \sigma_l \cdot (1 + \cos\theta) \quad \text{Equation 3.2}$$

The adhesive energy between a solid and a liquid can be separated into interaction between the dispersive components of two phases and interactions

between the polar components of the two phases with accordance to Equation 3.3.

$$W_{sl} = 2 \cdot \left[ (\sigma_l^d)^{\frac{1}{2}} \cdot (\sigma_s^d)^{\frac{1}{2}} + (\sigma_l^p)^{\frac{1}{2}} \cdot (\sigma_s^p)^{\frac{1}{2}} \right] \quad \text{Equation 3.3}$$

Where  $\sigma_l^d$  and  $\sigma_s^d$  represent the dispersive components and  $\sigma_l^p$  and  $\sigma_s^p$  represent the polar components of the surface energy for liquid and solid.

Summing up with Equations of 3.1-3 yields the Fowkes surface free energy as written in Equation 3.4.

$$\sigma_l \cdot (1 + \cos\theta) = 2 \cdot (\sigma_s^d \cdot \sigma_l^d)^{\frac{1}{2}} + 2 \cdot (\sigma_s^p \cdot \sigma_l^p)^{\frac{1}{2}} \quad \text{Equation 3.4}$$

The Owen-Wendt model extended from Fowkes equation can be expressed by two equations of Young (Equation 3.1) and Good (Equation 3.5)

$$\sigma_{sl} = \sigma_s + \sigma_l - 2 \cdot (\sigma_s^d \cdot \sigma_l^d)^{\frac{1}{2}} - 2 \cdot (\sigma_s^p \cdot \sigma_l^p)^{\frac{1}{2}} \quad \text{Equation. 3.5}$$

Equation 3.5 combined with Equation 3.1 gives following Owen-Wendt model.

$$\frac{\sigma_l \cdot (1 + \cos\theta)}{2 \cdot \sqrt{\sigma_l^d}} = \frac{\sqrt{\sigma_l^p}}{\sqrt{\sigma_l^p}} \cdot \sqrt{\sigma_s^p} + \sqrt{\sigma_s^d} \quad \text{Equation 3.6}$$

where subscripts  $l$  and  $s$  are for liquid and solid interface, respectively. This equation has the form of  $y = ax + b$  with  $y = \sigma_l \cdot (\cos\theta + 1)/2\sqrt{\sigma_l^d}$ ,  $a = \sigma_s^p$ ,  $x = \sigma_l^p/\sigma_l^p$ , and  $b = \sigma_s^d$ . In order to calculate the surface energy from Owen-Wendt model, at least two probing liquids requires to get the values of  $\sigma_s^d$  and  $\sigma_s^p$ . From the contact angle measurement based on

Owen-Wendt model,  $\sigma_s^d$  and  $\sigma_s^p$  and the surface free energies,  $\sigma_s$ , of each film were calculated in Table 3.8.

The work of adhesion between film and substrate can be calculated by the contact angle measurement and harmonic mean equation, which us given by [98].

$$W_{12} = 4 \cdot \left( \frac{\sigma_{s1}^d \sigma_{s2}^d}{\sigma_{s1}^d + \sigma_{s2}^d} + \frac{\sigma_{s1}^p \sigma_{s2}^p}{\sigma_{s1}^p + \sigma_{s2}^p} \right) \quad \text{Equation 3.7}$$

where subscripts  $d$  and  $p$  are dispersion and polar component of surface tension of solid,  $\sigma$ , respectively. And subscripts 1 and 2 represent the substrate and three films, respectively

**Table 3.8** Contact angles, surface energy values and work of adhesion of Sn, TiO<sub>2</sub> and Al<sub>2</sub>O<sub>3</sub> films (W: water and E: ethanol)

	Contact angle ( $\theta$ )	Dispersive component ( $\sigma_s^d$ , mN/m)	Polar component ( $\sigma_s^p$ , mN/m)	Surface free energy ( $\sigma_s$ , mN/m)	Work of adhesion ( $W_{12}$ , mJ/m <sup>2</sup> )
Si	83.7 (W)	9.99	14.28	24.27	-
	0 (E)				
Sn	84.9 (W)	8.27	15.23	23.50	47.58 (Sn/Si)
	0 (E)				
TiO <sub>2</sub>	24.2 (W)	88.28	1.19	89.46	40.28 (TiO <sub>2</sub> /Si)
	0 (E)				
Al <sub>2</sub> O <sub>3</sub>	5.5 (W)	102.49	0.62	102.49	38.78 (Al <sub>2</sub> O <sub>3</sub> /Si)
	0 (E)				

The strangest work of adhesion was appeared in the interface of Sn/Si. This was accorded with the result of peel-out test qualitatively. Even though  $\text{Al}_2\text{O}_3$  film was stronger than  $\text{TiO}_2$  film in the peel-out test, the  $\text{Al}_2\text{O}_3$  film had the lower value of work of adhesion. This might be originated from the porosity of  $\text{TiO}_2$  film which would be dealt in the chapter 6.

### 3.5.4 Microstructural property

As an engineering film, microstructural stability of product, before and after the deposition is the most useful criteria as it has to be applied in its original physical property for its intended functional purpose. Here the microstructural properties of three materials, including Sn,  $\text{TiO}_2$  and  $\text{Al}_2\text{O}_3$ , were investigated through XRD before and after NPDS deposition.

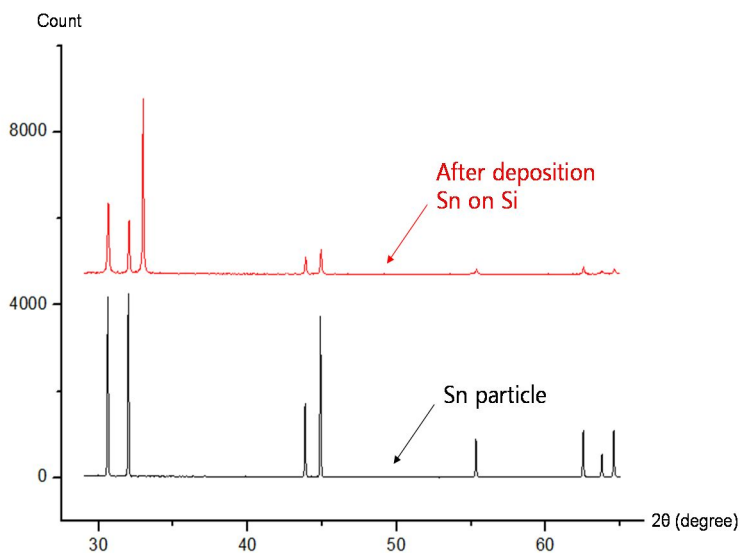


**Figure 3.10** XRD results of Sn: before and after deposition

As seen in Figure 3.10, overall the microstructure was the same as before and after depositing Sn particle by NPDS. However, the  $\text{SnO}_2$  peak at the angle of  $34^\circ$  was appeared. This might be caused by the oxidization of the

deposited film.

In case of TiO<sub>2</sub> nanoparticles, the XRD was implemented with 2θ from 20° to 60°. Before depositing TiO<sub>2</sub> nanoparticles via NPDS, the anatase phase of TiO<sub>2</sub> nanoparticle showed angular characteristics of 25.28°, 27.80°, 48.04°, 53.89°, and 55.06°, as shown in Figure 3.11. TiO<sub>2</sub> nanoparticle purchased from Nanoarmor has contents of 97 % of anatase and 3 % of rutile phases' nanoparticles. Because of 3 % of rutile phase of TiO<sub>2</sub> nanoparticle, the small peaks were appeared at rutile angles partially. Namely, it means that anatase phase of TiO<sub>2</sub> nanoparticle does not change its physical characteristic after high velocity particle deposition process.

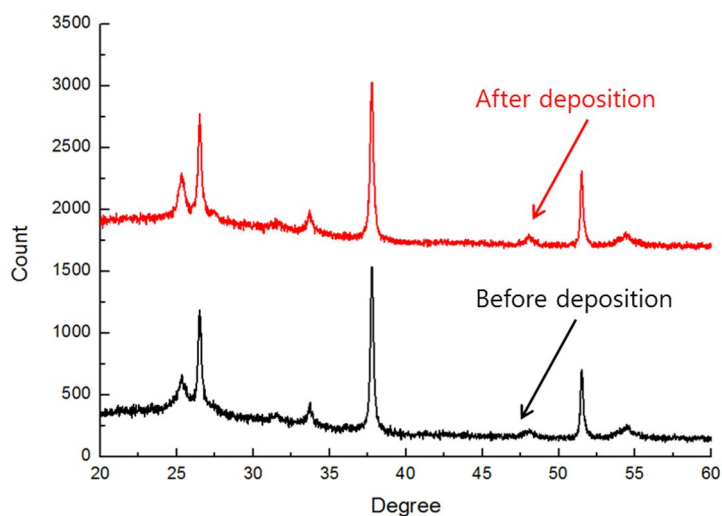


**Figure 3.11** XRD results of TiO<sub>2</sub>: before and after deposition

In case of Al<sub>2</sub>O<sub>3</sub>, shown in Figure 3.11, the phase of the Al<sub>2</sub>O<sub>3</sub> powder revealed peaks for polycrystalline  $\alpha$ -Al<sub>2</sub>O<sub>3</sub>. The substrate indicated a single crystallization peak for the (0001) plane. The deposition results showed diffraction peaks for both the substrate and  $\alpha$ -Al<sub>2</sub>O<sub>3</sub>. The diffraction peaks at 31° and 33 ° can be seen only in  $\delta$ -Al<sub>2</sub>O<sub>3</sub> or  $h$ -Al<sub>2</sub>O<sub>3</sub>.  $\eta$ -Al<sub>2</sub>O<sub>3</sub> was normally obtained after sintering from 800 °C to around 1000 °C. This result confirms

that the temperature was instantly increased when the particles were broken to a smaller size, and then deposited on the substrate using NPDS.

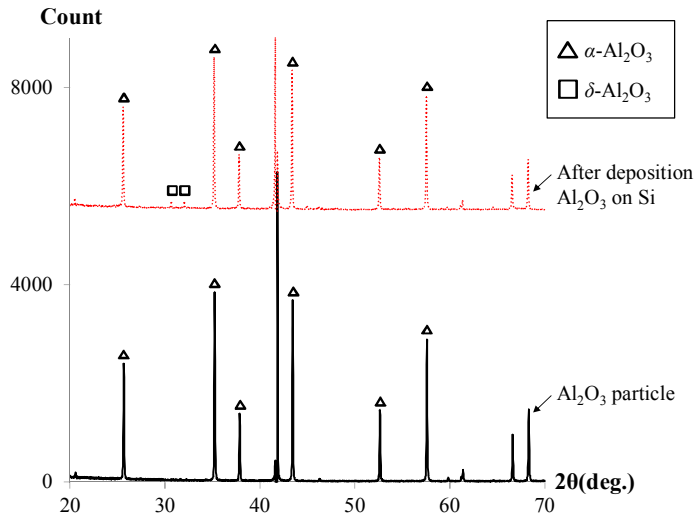


**Figure 3.12** XRD results of Al<sub>2</sub>O<sub>3</sub>: before and after deposition

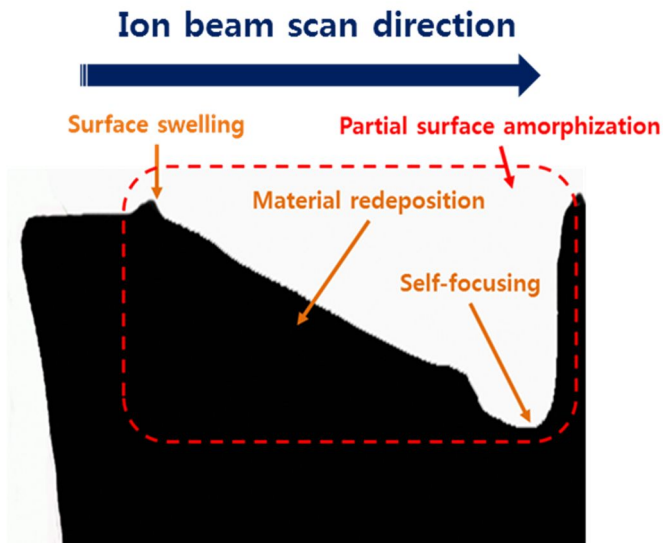
# 4 Nanostructuring by FIB

## 4.1 Overview

Precision nanostructuring via FIB had been realized by FIB with various parameters for milling and deposition (Focused ion beam induced deposition, FIBID or FIB-CVD) for the developments of various functional structures and devices [55, 99-101]. In the criteria of FIB fabrication a variety of nanoscale effects could be took place by the ion-solid interactions [55, 102-104]. Recent review article in [55, 63] explains a variety of approaches with the aim of the higher precision in FIB processing with the comprehensive physical and chemical concerns. As written in this review, many researchers had been improved the precision of FIB fabricated structures by focusing on the ion energy, dwell time and so on. Except for these kinds of parametric researches, the precision of FIB fabrication could be improved by accommodating the tool path concept from the convention mechanical machining process such as a milling [52, 105, 106]. The comprehensive understanding of nanoscale phenomena (Figure 4.1) which can improve the geometric precision and accuracy should be investigated in order to generate the adequate ion beam path for certain target geometries.

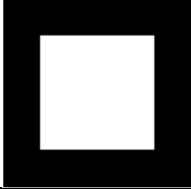
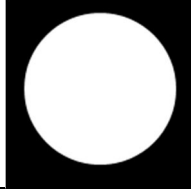
For the purpose of understanding of nanoscale phenomena in FIB and improving the geometric precision/accuracy, three types of target geometries were suggested in Table 4.1. On the basis of Table 4.1, first of all, the advanced scan method was developed by extending the current FIB parameters against the conventional scan method to increase the manufacturability and remove the defect in FIB fabrication. Two scan methods were compared with the experiment and simulation. In order to understand the physical and chemical phenomena in FIB, the 2D pocket,

shown in Table 4.1, was fabricated using the conventional scan method with the consideration of the dwell time and the beam overlap. And their effects were analyzed in physically and chemically. Then, the ion beam paths were generated to improve the precision and accuracy of 2.5D pocket with advanced scan method. Finally, the scan strategy with the advanced ion beam path was developed for the fabrication of 3D pocket. The ion beam paths generated for 2.5D/3D, which is useful for 3D printing process, were taken into consideration of FIB induced defective nanoscale phenomena.



**Figure 4.1** 2D illustration of nanoscale phenomena induced by ion-solid interactions: representative surface morphology of FIB milled structure influenced by the various nanoscale phenomena such as surface amorphization, material redeposition, self-focusing and material swelling.

**Table 4.1** Target geometries for nanostructuring by FIB

	2D pocket	2.5D pocket	3D pocket
Top view			
Cross-section view			

## 4.2 Definition of FIB parameters

The FIB parameters for nanofabrication were categorized into five systematically; (1) ion beam parameter, (2) processing parameter, (3) ion beam path parameter, (4) evaluation parameters, and (5) relative parameter. The detail explanation will be done as following sub-sections. Notably, the relative parameters were extended from current FIB parameters.

### 4.2.1 Ion beam parameters

The ion beam parameter can be defined as ion beam quantity and quality determined by the focusing system after emission of ions from liquid metal ion source: 1) ion energy, 2) ion current (emission current), 3) probe current and 4) probe diameter.

### 4.2.2 Processing parameters

The processing parameter can be determined by the deflection system of FIB. After being determined of ion beam condition, this processing parameter

can be controllable: 1) scan size, 2) scan resolution (pixel size), 3) dwell time, 4) beam overlap, 5) ion dose (number of scan) and 6) refresh time.

#### **4.2.3 Ion beam path parameters**

The ion beam path parameter is most important issue in this research. This deals with how the ion beam can be controlled and moved: 1) scan style and 2) scan strategy.

#### **4.2.4 Evaluation parameters**

The evaluation parameter is required to indicate the performance of fabrication result: 1) processing time, 2) material removal rate (sputtering yield), 3) precision, 4) accuracy and 5) side effect.

#### **4.2.5 Relative parameters**

The relative parameter is newly suggested in this research in order to get more efficiency of FIB fabrication. These parameters deal with the relationship of each parameter: 1) ion beam irradiation time, 2) ion beam travel time, and 3) ion beam irradiation enhancement factor.

### **4.3 Material**

All experiments which were done in this section used single crystalline silicon substrate because it had very flat surface (RMS surface roughness around 0.1 nm measured by atomic force microscope (AFM)) and also it had been investigated from many researchers for various applications. The single crystalline silicon had the orientation of <100>.

## 4.4 Instrumentation

Including the FIB system which build-up for nanoscale 3D printing process, shown in Figure 2.11, another FIB system was also used for nanofabrication. It was SMI 3050 (SII Nanotechnology Inc.), as shown in Figure 4.2. This FIB system adopts the gallium ion source of which energy up to 30 kV, and its minimum image resolution is 4 nm at 30 kV. This system also included the gas injection system for tungsten and carbon deposition.

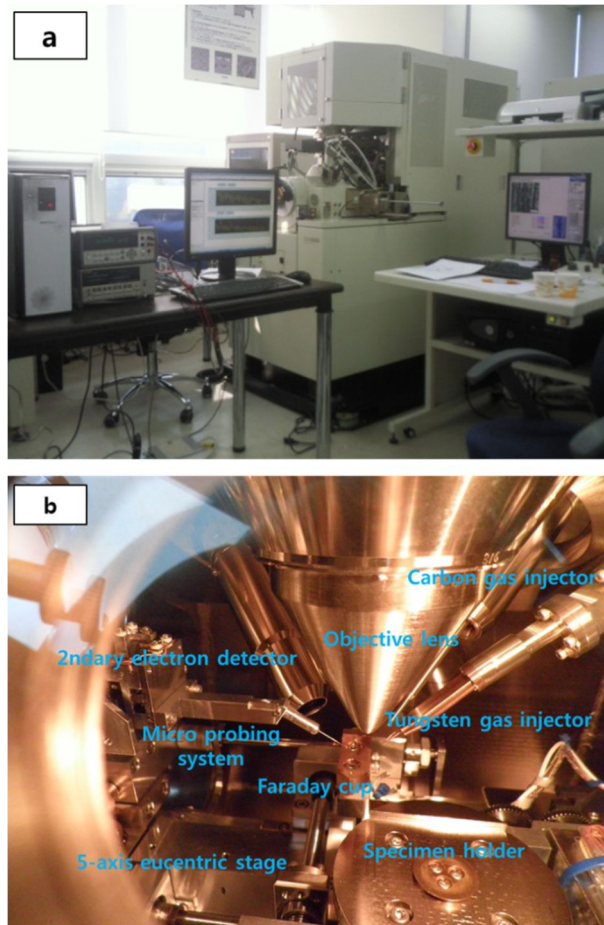


**Figure 4.2** SMI 3050 (SII Nanotechnology Inc.) with (a) *in situ* Monitoring system and (b) inside of main processing chamber.

## 4.5 Modeling of scan method

The SMI 3050 system not only provides the normal raster but also the vector scan. When utilizing the vector scan, the raster scan can be controlled by '*dot-to-dot*' and '*line-to-line*'. From now on, it is called scan style which express the how ion beam moves. The description of scan style is illustrated in Figure 4.3 for the explanation of scan style in case of the raster scan. According to the each scan style, the processing time can be calculated from Equation 4.1-2. And these equations can be categorized into terms in Table 2. In these equations, the first term deals with the ion beam irradiation time on a targeted area, and last two terms deals with the ion beam travel time which represent that unwanted ion beam irradiation on targeted and untargeted areas due to the beam blanking. Namely, if the ion beam travel time is increased, the total processing time is increased. If this ion beam travel time is not excluded, then the miscalculation of ion dose and efficiency will happen. Thus, the scan style depicted in Figure 4.3(b) was developed and suggested with the aim of the minimization of unwanted ion beam irradiation generated in Figure 4.3(a).

However, figure 4.3(b), advanced scan method using the scan style of dot-to-dot, caused the beam positioning error at the end of scan point before returning back to its scan start point when the screening experiments were performed as shown in Figure 4.4(a). In order to overcome this ion beam positioning error at the right pixel, intentionally the area blanking was applied as shown in Figure 4.4(b). Accordingly, the scan method was modified from Figure 4.3(b) to Figure 4.5.

Processing time

$$\begin{aligned}
 &= (n_{dot} \cdot t_d \cdot N_{scan}) + \{(t_b \cdot (n_{row} - 1) \cdot N_{scan})\} \\
 &+ \{(N_{scan} - 1) \cdot t_a\} \qquad \qquad \qquad \text{Equation 4.1}
 \end{aligned}$$

Processing time

$$\begin{aligned}
 &= (n_{dot} \cdot t_d \cdot N_{scan}) + \{(t_p \cdot (n_{dot} - 1) \cdot N_{scan})\} \\
 &+ \{(N_{scan} - 1) \cdot t_a\} \qquad \qquad \qquad \text{Equation 4.2}
 \end{aligned}$$

Where  $n_{dot}$ ,  $n_{row}$ ,  $t_d$ ,  $t_p$ ,  $t_b$ ,  $t_a$ ,  $N_{scan}$  represent the number of dot, the number of row, dwell time, point blanking time, line blanking time, and area blanking time, the number of scan, respectively.

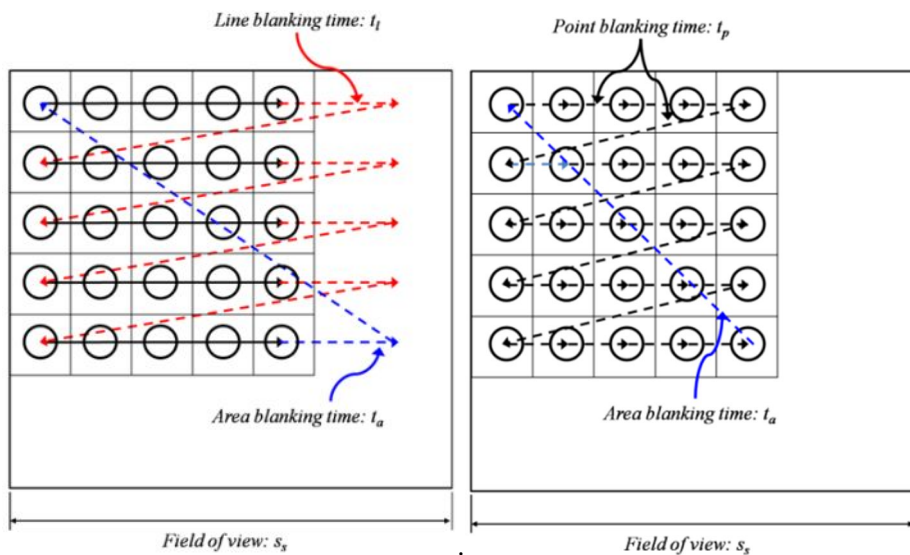


**Figure 4.3** Two types of scan style for the development of raster scan: (a) normal raster scan (synchronized with scan signal when imaging) and (b) raster scan with dot-to-dot.

**Table 4.2** Relative parameters according to the scan style in the raster scan

	Conventional scan	Dot-to-dot scan
<b>Ion beam irradiation time (A)</b>	$n_{dot} \cdot t_d \cdot N_{scan}$	$n_{dot} \cdot t_d \cdot N_{scan}$
<b>Ion beam point blanking time (B)</b>	-	$t_p \cdot (n_{row} - 1) \cdot N_{scan}$
<b>Ion beam line blanking time (C)</b>	$t_l \cdot (n_{row} - 1) \cdot N_{scan}$	-
<b>Ion beam area blanking time (D)</b>	$(N_{scan} - 1) \cdot t_a$	$(N_{scan} - 1) \cdot t_a$
<b>Ion beam total travel time (E)</b>	C+D	B+D
<b>Ion beam irradiation enhancement factor (F)</b>	A/E	A/E

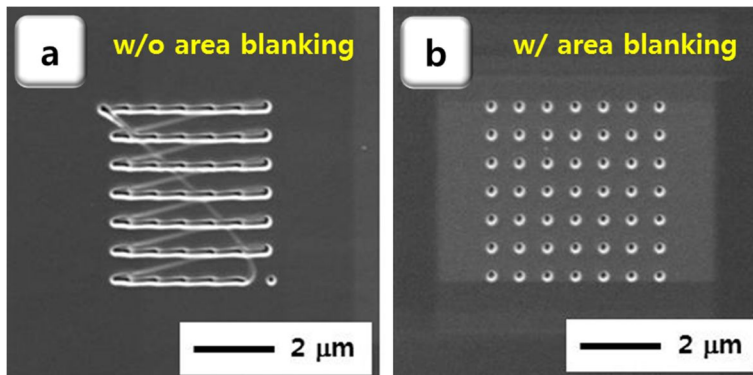


**Figure 4.4** Ion beam tracking in the raster scan utilized with dot-to-dot scan style: (a) without area blanking time and (b) with area blanking time



1,000 ~ 50 %, and the fixed ion dose of  $1.4E+35 \cdot I_p \text{ ions/cm}^2$ . The results were shown in Figure 4.6.

The results of simulation indicated that the processing time influenced by the dwell time and the beam overlap could not too much influenced by the scan style. In case of scan ion beam irradiation enhancement factors shown in Figure 4.6a<sub>2</sub> and Figure 4.6b<sub>2</sub>, however, their results were highly influenced by the scan style. Accordingly, it means that the processing time could also be improved by utilizing the new scan style of dot-to-dot.

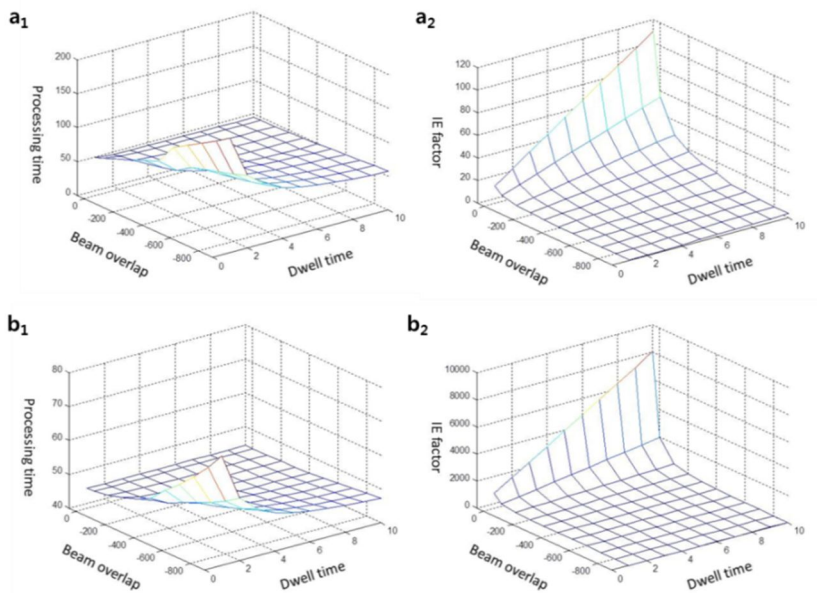


**Figure 4.6** Simulation of the effect of both dwell time and beam overlap to the ion beam irradiation enhancement factor (F) and the processing time (total ion beam processing time (E)) according to the scan styles of conventional raster scan (a<sub>1-2</sub>) and dot-to-dot scan (b<sub>1-2</sub>)

#### 4.6 Understanding of nanoscale phenomena

As simulated before section, the dwell time and the beam overlap had

remarkable influences to the relative parameters involved with time consuming issue. Excluding this time consuming issue, here, nanoscale phenomena induced by the dwell time and the beam overlap were investigated with the adoption of conventional scan method, Figure 4.3(a), to understand the defect generation in FIB nanostructuring because the understanding of them is very important to get high precision and accuracy in FIB nanostructuring.

#### **4.6.1 Influence of dwell time**

##### **4.6.1.1 Overview**

Ion-solid interactions in FIB have been reported to induce a variety of surface and sub-surface morphological effects at the nanoscale [63, 104, 107]. These well-known nanoscale effects relate to material redeposition, self-focusing, and surface amorphization (often can swell the surface), as depicted in Figure 4.1; (1) *Material redeposition* (inside the structure): the sputtered atoms (neutral atoms and ions) ejected from the surface tend to redeposit into the already sputtered surface, (2) *Self-focusing* (inside edge of the structure): secondary sputtering process that originates from ion reflection by the sidewall of trench and (3) *Surface amorphization* (inner and outer-sides of the structure): incident ions of insufficient ion energy, not exceeding the surface binding energy of target atoms can be buried in the target surface by displacing the target atoms, resulting in the defect generation or volumetric expansion [51, 63, 108, 109]. These effects not only favor deterioration of the surface quality by introducing surface irregularities and unwanted ion doping near the surface through microstructural damage but also affect the sputtering yield, particularly in TEM sample preparations [110-112]. Sputtering yield has been investigated extensively with numerous studies reporting changes in sputtering yield as a function of FIB processing parameters as particularly dwell time on a variety of targets [105, 113]. In contrast to previous work, the investigation dealt in here focuses on complex morphological, compositional and physicochemical characteristics close to the surface which is influenced by the dwell time which cause scan speed variation.

Here, six microstructures were fabricated by increasing the dwell time from 1 to 1,000  $\mu\text{sec}$ , resulting in the decrease of scan speed using the raster scan. The surface morphologies were observed using FE-SEM, SIM and confocal microscopy and compositions were analyzed with energy dispersive X-ray spectroscopy (EDXS) and wavelength dispersive spectroscopy (WDS). Further, the surface physicochemical microstructure was elucidated by *Raman* surface mapping. The resulting nanoscale effects including two directional material redeposition, self-focusing, and surface amorphization, were investigated by both surface imaging and analytic methods.

#### 4.6.1.2 Experiment

The experimental conditions are listed in Table 4.3 and the raster scan strategy shown in Figure 4.3(a) was utilized. The stability of the ion current of 3,027 pA was approximately 0.1 %<sub>p-p</sub>. In order to clearly visualize the FIB induced nanoscale phenomena when sputtering the silicon (100) target, the dwell time was varied from 1 to 1,000  $\mu\text{sec}$  since the dwell time is a well-defined parameter resulting in a number of nanoscale effects including the material redeposition among others discussed above. The dwell time difference resulted in changes in the scan speed such that increase in the applied was dwell time correlated with a decrease in the scan speed.

**Table 4.3** Experimental conditions

Parameters	Conditions
Ion sources	Gallium
Ion energy (kV)	30
Target	Si (100)
Ion current (pA)	3,000
Scan routine	Raster
Scan size ( $\mu\text{m}^2$ )	20 x 20
Dwell time ( $\mu\text{s}$ )	1, 200, 400, 600, 800 and 1,000
Ion dose (ions/ $\text{cm}^2$ )	$5.7 \times 10^{20}$

The surface morphologies and chemical compositions of FIB induced

microstructures were measured with FE-SEM (SUPRA 55VP, Carl Zeiss), SIM (SMI3050, SII Nanotechnology) and WSI (NT9100, Veeco) and analyzed with EDXS (Bruker, xflash 4010) and WDS (EPMA-1600, Shimadzu). Spatial Raman mapping was performed using a confocal laser *Raman* microscope (RAMANplus, Nanophoton) to analyze the surface physicochemical microstructure of the products. The wavelength of the excitation laser was 532 nm and the engaged power of the line beam was kept below 1.5 mW to ensure the removal of additional annealing effects.

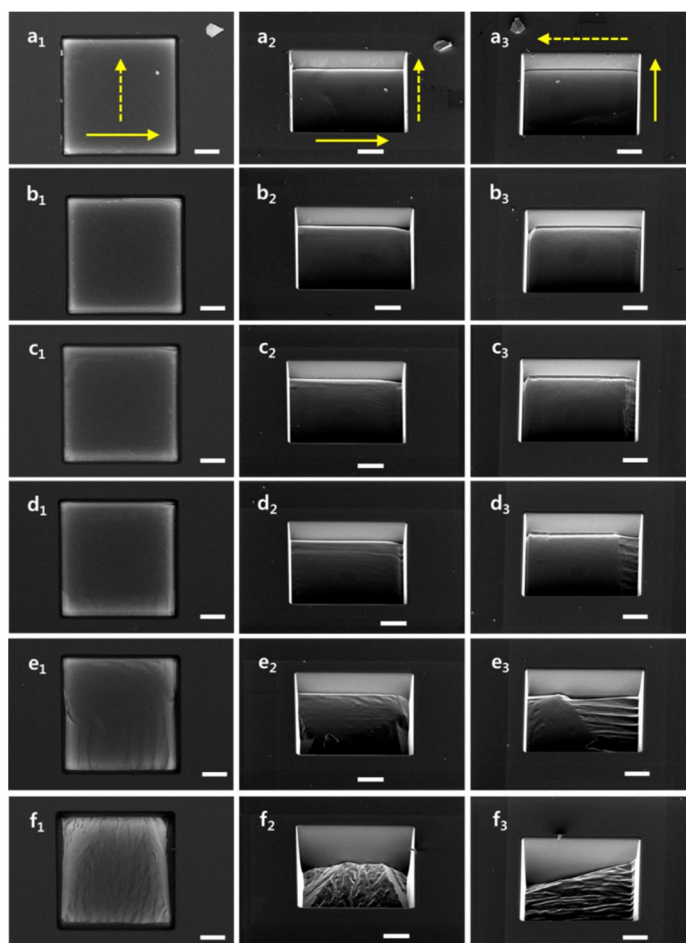


**Figure 4.7** FE-SEM images of FIB milled microstructures: ( $a_1\sim f_1$ ) plain view, ( $a_2\sim f_2$ ) 45° tilt view and ( $a_3\sim f_3$ ) 45° tilt view which are rotated 90° to the counterclockwise from ( $a_2\sim f_2$ ). The continuous arrow indicates the horizontal scan direction and the dotted arrow indicates the vertical scan direction.

#### 4.6.1.3 Surface morphology

SIM imaging can be applied for surface morphology observations because it is particularly useful for direct morphological changes after milling of microstructures by FIB and exploits the high contrast sensitivity to surface morphology and crystallites (ion channeling) properties. However, the crystallographic structure of these crystallites cannot be observed by SIM because of limitations affecting the atomic resolution similar to the TEM. It is also disadvantaged by low resolution, surface damage and ion implantation over SEM even though it utilizes an extremely low ion current around 1 pA. For this reason, FE-SEM was used for secondary electron imaging with high spatial resolution. These FIB induced microstructures are shown in Figure 4.7.

As shown in Figure 4.7, material redeposition is seen to occur as a function of dwell time (scan speed) against the scan direction from left to right and changes in the material redeposition were correlated with the dwell time such that decreased material redeposition was observed when the dwell time was decreased. The smallest dwell time of 1  $\mu$ sec resulted in a flat bottom surface as shown in Figure 4.7(a). However, when the dwell time exceeded 200  $\mu$ sec, the *horizontal* material redeposition was observed visually. This type of 2-dimensional materials redeposition has been investigated by others previously authors [113-115]. Unlike previous observations [114, 116] in the present study when the dwell times were measured over 800  $\mu$ sec and the material redeposition was not predictable with the same manner reported in elsewhere, due to the occurrence of very complex surface morphologies, as shown in Figure 4.7(e and f). It has been reasoned that the complex material redeposition observed under these conditions is a result of scan speed variation between *horizontal* and *vertical* scans. To investigate this further, the scan speed was decreased from 7.49, 0.40, 0.20, 0.13, 0.10 and 0.08 nm/ $\mu$ sec *horizontally* and it was decreased in 300.00, 1.60, 0.80, 0.53, 0.40, and 0.32 nm/ $\mu$ sec. However, for each dwell time cases the *vertical* scan speed was much slower than the *horizontal* scan speed (by the factor of 1/25). Although the ion beam scan in the *vertical* direction was discrete, the material redeposition occurred at much slower speeds as can be seen for dwell times corresponding to 800 and 1,000  $\mu$ sec. SEM images in Figure 4.7 also shows that

changes in the surface morphology of the whole FIB induced microstructures cannot be captured in its entirety. Therefore, confocal microscopy was applied to visualize the entire range of surface morphologies by 3-dimensional (3D) imaging as shown in Figure 4.8. The phenomenon of 3D complex material redeposition was easily discernible in Figure 4.7. In Figure 4.7(e), however, the surface morphology was somewhat different to Figure 4.7(f). Conventionally, the surface swelling has been shown to occur around the outside edges by forming nanoscale rims by surface amorphization or defect generation before amorphization. In this present investigation, a new phenomenon was revealed by considering the extended defect formation rather than localized regions [117], The analysis showed the surface swelling was extended within the microstructure as shown in Figure 4.7(e) resulting in protrusion of the ion beam direction. At 1,000  $\mu\text{sec}$  dwell time, material redeposition in *vertical* direction was dominant compared to the *horizontal* direction, suggesting stronger material deposition during the *vertical* scan mode (Figure 4.7(f)).

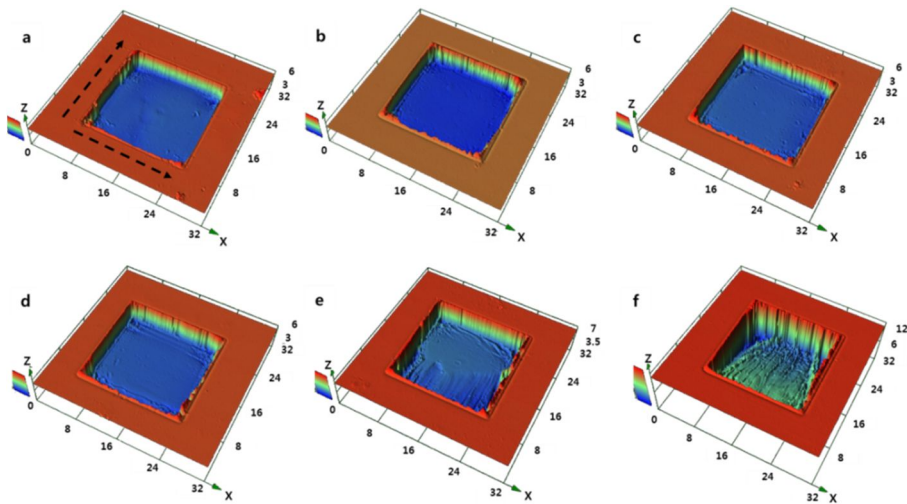


**Figure 4.8** 3D optical profiles of FIB milled microstructures: (a) 1  $\mu\text{sec}$ , (b) 200  $\mu\text{sec}$ , (c) 400  $\mu\text{sec}$ , (d) 600  $\mu\text{sec}$ , (e) 800  $\mu\text{sec}$ , and (f) 1,000  $\mu\text{sec}$  of dwell times (two arrows express the ion beam scan directions in horizontal and vertical).

In addition to the redeposition effects, surface amorphization and self-focusing phenomena was also observed in the present investigation (Figure 4.7 and 4.8). It is

noteworthy here that in both results, the swelled volumes were observed at the outer edges of the microstructures. The area of material swelling was darker and smooth compared to the pure silicon site shown in Figure 4.7, and the volumetric differences of material swelling was clearly observable in Figure 4.8. Both Figure 4.7 and 4.8 also demonstrated that, swelling volume was increased by increasing the dwell time. This material swelling was originated by the doping of gallium ion near/under the surface by softening the near surface lattice in the amorphized state. Additionally, the diffusion induced deposition with the help of the weak ion flux at the tail of the Gaussian-shaped ion beam can assist the volumetric expansion. However, it is known that this diffusion induced deposition is much less in usual [118].

In contrast, the inner edges of the bottom regions were brighter than the microstructural centers [(Figure 4.7(a<sub>1</sub>~f<sub>1</sub>)). This indicated that the self-focusing took place periodically every four edges by the secondary sputtering of the inclined walls. Typically, such bright areas were too narrow to observe using confocal microscopy due to the limitation of lateral resolution as shown in Figure 4.8.

**Table 4.4** Overall chemical compositions of six FIB microstructures

<b>Dwell time [μs]</b>	<b>Si [at %]</b>	<b>Ga [at %]</b>	<b>O [at %]</b>
<b>1</b>	96.2	1.43	2.37
<b>200</b>	96.12	1.33	2.55
<b>400</b>	96.26	1.12	2.62
<b>600</b>	96.35	1.11	2.55
<b>800</b>	96.53	1.00	2.47
<b>1,000</b>	96.76	1.17	2.08

#### **4.6.1.4 Compositional characteristic**

In order to investigate the compositions, EDXS as the most versatile tool for compositional analysis was initially applied. The averaged chemical compositions are shown in Table 4.4. In general, the chemical composition of silicon was increased and that of gallium was decreased by increasing the dwell time. The oxygen content

results from the oxidation of the surface by exposure to the atmosphere and its value was neglected in this study.

The EPMA analysis was implemented to take advantage of acquiring precise quantitative of chemical analysis from the surface morphologies primarily by the wavelength dispersive spectroscopy (WDS) over EDXS analysis. Figure 4.9-10 show the 3D compositional map for silicon and gallium, respectively, as chemicals of interest. Figure 4.9 represents the silicon compositional map and the scan end lines (top and right edges) which shows the overall weak silicon signal. Furthermore, the intensity of silicon on the opposite side of scan direction (Figure 4.9) increased to the diagonal direction (from *top-right* to *bottom-left*) as a function of dwell time. This indicates a higher amount of material redeposition towards a direction opposite to that of the ion beam movement both vertically and horizontally. However, the intensity of silicon appeared stronger against the vertical direction due to a lack of signal intensity in lateral direction at the maximum dwell time of 1,000  $\mu\text{sec}$ . Furthermore, the weak silicon compositions appeared around the edges inside the microstructures. This event is driven by the *self-focusing effect* which occurs due the accumulation of the gallium ion in this region and causes the reflection of the incident ions against the inclined sidewalls.

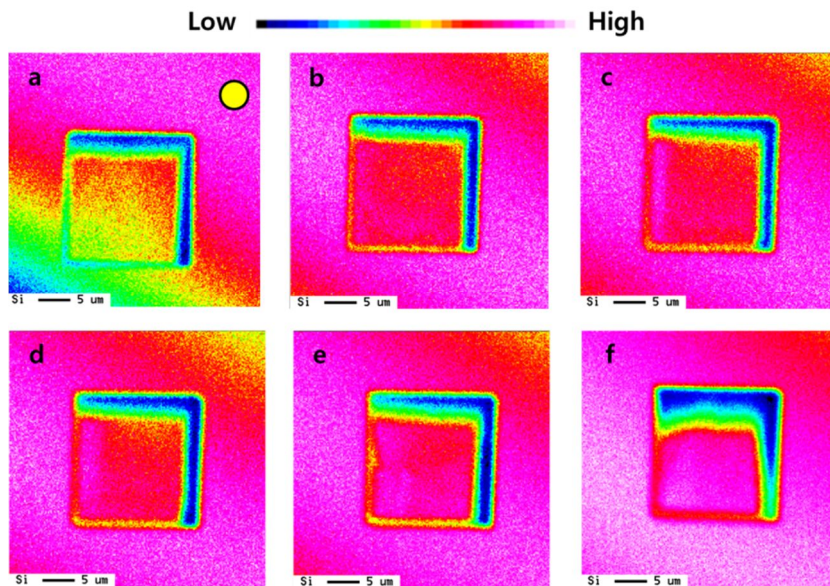


**Figure 4.9** 3D compositional mapping of silicon using EPMA: (a) 1  $\mu\text{sec}$ , (b) 200  $\mu\text{sec}$ , (c) 400  $\mu\text{sec}$ , (d) 600  $\mu\text{sec}$ , (e) 800  $\mu\text{sec}$  and (f) 1,000  $\mu\text{sec}$  of dwell times.

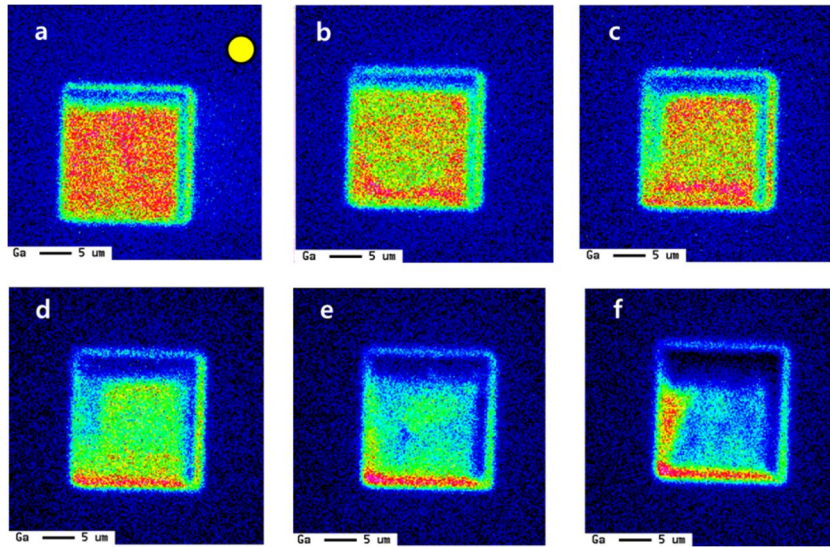


**Figure 4.10** 3D compositional mapping of silicon using EPMA: (a) 1  $\mu\text{sec}$ , (b) 200  $\mu\text{sec}$ , (c) 400  $\mu\text{sec}$ , (d) 600  $\mu\text{sec}$ , (e) 800  $\mu\text{sec}$  and (f) 1,000  $\mu\text{sec}$  of dwell times.

Except for the intensity of silicon itself, the high intensity region of silicon was reduced by increasing the dwell time. It was obvious that the depth of microstructure influenced the detection of intensity signal against the detector position, of which position is expressed in the Figure 4.9 and 4.10 with the yellow circle.

In contrast to Figure 4.9, the composition of gallium was decreased with incremental increase in dwell time. In case of Figure 4.10(a-c), the doped gallium ions were distributed fairly even on the ion beam in the irradiated region because the sputtered silicon atoms were relatively less compared to the other three higher dwell time measurements or indeed may have been balanced with the gallium ions on the surface. This may be reasoned by considering the doping of gallium which occurs successively over numerous cycles with the fastest scan speed. This suggests that the newly redeposited silicon atoms were resputtered repeatedly with increasing ion beam strength (ion dose resulting from the increase in the number of scans). Using the transport and range of ions in matter (TRIM) simulation, the ion range which generated target atom displacement was calculated for dwell times of 1  $\mu\text{sec}$  (minimum) and 1,000  $\mu\text{sec}$  (maximum) with the surface sputtering mode. In both cases, the lateral damages caused by ion irradiation were significantly different, but the cross-sections were marginally different as demonstrated by the maximum target

atom displacements at both dwell times respectively. It can be inferred that the short dwell time is only insufficient in milling the surface, but also leads to reduced sputtering of silicon atoms that uniformly cover the surface indicating homogeneous gallium dopant distribution, as shown in Figure 4.10(a-c).

Unlike our previous explanations for silicon intensities, the gallium intensity of four inner edges of microstructures of Figure 4.10(a-c) seemed different, indicating the lower intensity of gallium. In detail, the gallium intensity at the right and top region was much less than the left and bottom region. This directly indicates that the position of detector influences the signal. We therefore deduce that, the intensities of gallium at the left and bottom edges were bona fide intensities that were not influenced by the position of the detector. More interestingly, the gallium intensities in Figure 4.10(a-c) on the bottom plane were higher than the inside edges which were influenced by the *self-focusing effect*. On the contrary, the other three events in Figure 4.10(d-f) were totally opposite. In Figure 4.10(d-f), the gallium intensities at the left and bottom edges were higher than the intensities of the bottom planes of the microstructures. It is obvious to state that the *self-focusing effect* has a significant influence on the microstructure when the material redeposition takes place abruptly. However, this result also includes one more mechanism induced by the material redeposition. It meant that the material redeposition of silicon had a responsibility of shadowing the gallium implantation. This will be explained again in the next section with the result of physic-chemical analysis.

In Figure 3 in [113], a severer case of material redeposition was observed in comparison to events using controlled dwell time measurements at single (1,000  $\mu\text{s}$  of dwell time) and multiple scan (10  $\mu\text{s}$ ) durations. Measurements derived from Figure 3 in [113] were used to determine the chemical contrast differences between the pure and redeposited silicon beneath the platinum coated region.

So far, variation in the chemical compositions inside the microstructures has been explained based upon observational differences. In addition to these observations, surface swelling outside of microstructures was also monitored through the compositional analysis (WDS). Small amounts of silicon were detectable from the outer edges of microstructures in Figure 4.9 because gallium ions were embedded on the outside edges as a result of surface swelling with defects and amorphization (by three mechanisms explained in the introduction). This correlation also revealed higher

amount of gallium detected at the outer edges as shown in Figure 4.11. Moreover, the highest amount of gallium was detected at the center of the rim in Figure 4.11.

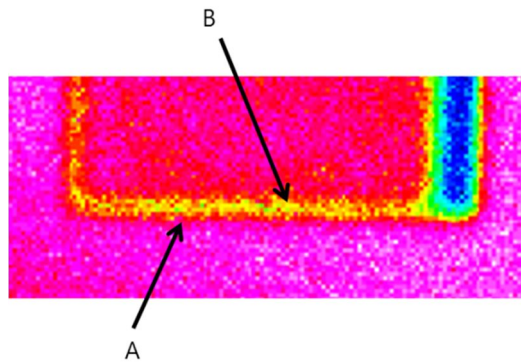


**Figure 4.11** The detail view of Figure 4.9(c): the area A indicates the region where the material swelling occurs, and the area B indicates the region where the self-focusing effect occurs.

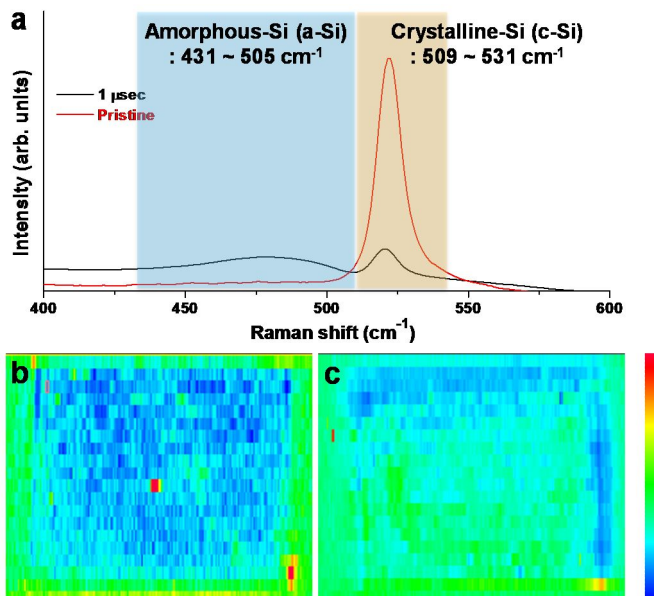


**Figure 4.12** (a) Raman spectra of pristine and FIB milled microstructures on the silicon (100) wafer with 1  $\mu\text{sec}$  of dwell time. Spectroscopic Raman mapping of FIB milled microstructures on the silicon (100) wafer with (b) 1  $\mu\text{sec}$  and (c) 400  $\mu\text{sec}$  of dwell time. Color bar displays relative intensity ( $I_{c-Si}/I_{a-Si}$ ); top (red) and bottom (blue) means high and low intensity, respectively.

#### 4.6.1.5 Physicochemical characteristic

*Raman* spectroscopy is a powerful technique used to identify the physicochemical microstructural changes of silicon after ion irradiation [116, 119, 120]. The *Raman* surface mapping was performed with a 532 nm excitation laser on the surface of the FIB milled microstructure on silicon (100) wafers, as shown in Figure 4.12 (1 and 400  $\mu$ sec of dwell time). The peak of the bulk crystalline silicon (*c*-Si) had a sharp and nearly *Lorentzian* band centered at 520  $\text{cm}^{-1}$  whereas the amorphous silicon (*a*-Si) exhibited a downward and broadened band shift near 475  $\text{cm}^{-1}$ . The spectrum of the pristine Si (Figure 4.12(a)) clearly indicated the presence of a highly crystalline *defect-free* state. However, the irradiation of the gallium ion led to induced surface amorphization, and this observation is consistent with previously reported transitions by ion implantations [116, 120]. Surface mappings ( $I_{c-Si}/I_{a-Si}$ ) can aid the elucidation of the different microstructural changes as a function of dwell time as shown in Figure 4.12(b). Figure 4.12(b) (1  $\mu$ sec of dwell time) shows the uniform surface amorphization irrespective of the irradiating region in accordance with the surface profile and compositional analysis of Figure 4.9-10. In contrast, the FIB milled microstructure generated by applying a dwell time of 400  $\mu$ sec exhibited inhomogeneous surface amorphization, i.e. the amorphization regions were shadowed by high amounts of material redeposition by sputtered silicon atoms composed of low defects which indicated the dominant *c*-Si (#1 in Figure 4.13(c)). This occurred because of preferential material redeposition generated against the scan. In combination with the preferential redeposition of sputtered silicon atom on the initially irradiating regions, the results suggest that the sputtered silicon atoms have been less affected by the gallium ion implantation and consequently retained the pristine crystallinity. These suggestions were further supported by the distinguishable characteristics of the *Raman spectra* at each irradiating region shown in Figure 4.13(a). At the lower dwell time of 1  $\mu$ sec (Figure 4.13(b)), all *Raman spectra* showed a mixture pattern of *a*-Si and *c*-Si and indicated uniform gallium ion distribution from repetition of both sputtering and redeposition as confirmed by surface profile and composition analysis. In contrast, at a higher dwell time of 400  $\mu$ sec (Figure 4.13(c)) resulted in the transition from dominant *c*-Si (scan start point: #1) to mixture of *a*-Si and *c*-Si (scan end point: #4) and demonstrated that the material redeposition of

sputtered silicon atoms and gallium ion implantation preferentially occurred at initial and endpoints respectively. Our observations thus demonstrates that implantation, sputtering, and redeposition during FIB milling are *dwell time-dependent* and occurs without any change in dose, species and ion energy. This suggests conclusively that the microstructure and the resultant morphology may readily controlled by processing parameters.

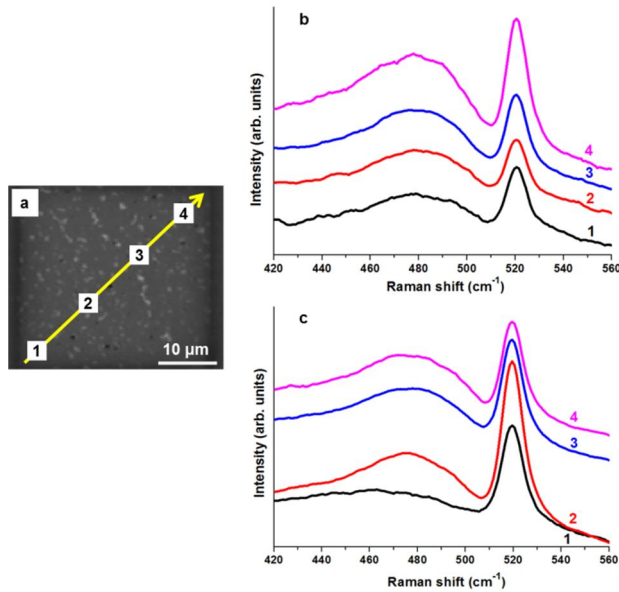


**Figure 4.13** (a) Four different regions, marked by labels, for obtaining the *Raman* spectrum. Characteristic *Raman spectra* of each zone of FIB milled wafers with (b) 1 μsec and (c) 400 μsec of dwell time.

#### 4.6.1.6 Summary

In this study, FIB induced microstructures were fabricated by varying the dwell time, resulting in differences of scan speed, and their morphologies, compositions and physicochemical characteristics were investigated 3-dimensionally by utilizing high resolution imaging and analytical methods such as FE-SEM, confocal microscope, EDXS, WDS and Raman spectroscopy. Based on the surface morphologies of microstructure influenced by various nanoscale phenomena such as material redeposition, self-focusing, and surface amorphization those were generated when the

sputtering was preceded, the composition and microstructural transformations were investigated and discussed with the various evidences comprehensively. In summary, the material redeposition event was took place not only morphologically, widely investigated by many researchers, but also in chemically and microstructurally in the localized microstructures by the variance of dwell time.

## **4.6.2 Influence of beam overlap**

### **4.6.2.1 Overview**

As pointed out in previous Section 4.4, the beam overlap can make a big variation of processing time, resulting in the number of scan variation. Therefore, the parametric study as a function of beam overlap was implemented in this section. In case of beam overlap, the scanning path trace is very important. Thus, FIBID, not FIB sputtering, was adopted to investigate the physical phenomena induced by the beam overlap. Of course, this investigation of FIBID could present much more ion beam induced phenomena which were not dealt in the section 4.6.1 (the influence of dwell time).

In case of FIBID process may include four steps as follows: First, the gas molecules are delivered onto the substrate through the gas injector system (GIS). Second, the primary ion beams initiate to dislocate the surface atom by the nuclear collision, and distributes the excited surface atoms (ESAs). Third, these ESAs dissociate the adsorbed gas molecules. Finally, volatile particles are removed through the vacuum system, while localized solid deposits such as carbon, tungsten, and platinum remain fixed on the surface of the substrate in the form of a thin film [55, 63, 121, 122].

Herein, the conventional scan method (Figure 4.3(a)) was used to make a localization of gas molecules of  $C_{14}H_{10}$  from GIS, and the surface morphologies and deposition rates as a function of beam overlap were

observed and investigated. In addition, the defectives that are originated from the intrinsic ion beam characteristics and the scan method were discussed.

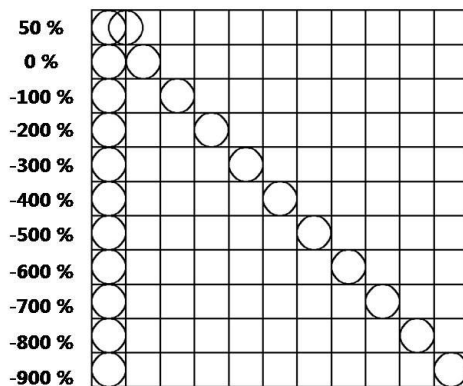


**Figure 4.14** Schematics of the ion beam processing as a function of beam overlap. The pixel size was 30 nm, and the probe diameter was 31 nm as measured by the knife edge method (simplified to 30 nm).

#### 4.6.2.2 Experimental conditions

For all experiments, the ion current was 11.8 pA, as measured in a Faraday cup by a pico-amperemeter (6517A, Kithley instrument), and phenanthrene gas molecules were used to localize the carbon. The probe diameter was measured through the knife edge method as approximately 31 nm. To simplify the experimental design when controlling the beam overlap, we assumed the probe diameter to be 30 nm. The energy of the gallium liquid metal ion source was 30 KeV, the field of view was 24  $\mu\text{m}$ , and the dwell time was 1  $\mu\text{sec}$ .

For this study, a raster scan was used, and the pixel size was changed with a fixed 0% overlap. The pixel sizes used were 300 nm, 270 nm, 240 nm, 210 nm, 180 nm, 150 nm, 120 nm, 90 nm, 60 nm, 30 nm, and 15 nm. The 0 % overlap combined with these pixel sizes resulted in beam overlaps of: -900 %, -800 %, -700 %, -600 %, -500 %, -400 %, -300 %, -200 %, -100 %, 0 %, and 50 %, respectively. A schematic of the ion beam processing for these

experiments is shown in Figure 4.14.

#### **4.6.2.3 Ion/solid and ion/gas molecule interactions**

Most of FIB induced nanoscale phenomena is well included in FIBID. Therefore, the FIB induced phenomena will be discussed with FIBID. In milling and deposition, one of the clearest features in the images is the delocalization of pattern size. This delocalization was much severe in case of FIBID than FIBM. The delocalization mechanisms were considered for a stationary ion beam. In this case, the localization of the structure was larger than the incident ion beam diameter. This deposit delocalization could have been produced by at least four mechanisms: (1) the range effect of ESAs by the ion flux distribution (due to the Gaussian distribution) [63, 121, 123], (2) ions scattered by gas phase precursor molecules prior to interaction with the solid substrate [63, 124], (3) secondary electron transition in the sample prior to emission [63, 124], and (4) surface diffusion [63, 118, 124]. The delocalization caused by (3) and (4) is negligible compared with that caused by (1) and (2). In most cases, ESAs, which are dependent on the range of the ion distribution, dominated the dissociation of adsorbed gas molecules and consequently delocalized the deposits.

#### **4.6.2.4 Surface morphology**

A raster scan routine with continuous and discrete processes was used by changing the beam overlap for FIBID in 2  $\mu\text{m}$  square boxes with a fixed ion dose of  $1.0 \times 10^{17}$  ions/cm<sup>2</sup>. The experiments showed a variety of surface morphologies, as shown in Figure 4.15-16.

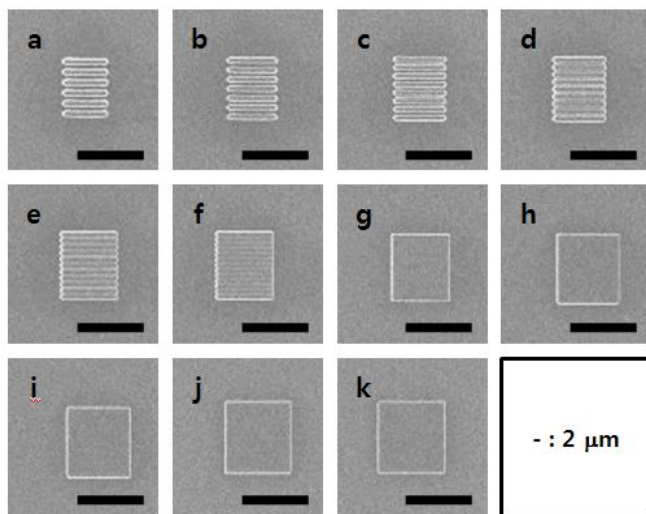


**Figure 4.15** Top views of SIM images: the carbon using phenanthrene gas molecules was deposited as a function of beam overlap; a: -900 %, b: -800 %, c: -700 %, d: -600 %, e: -500 %, f: -400 %, g:-300 %, h:-200 %, i:-100 %, j: 0 %, and k: 50 %.

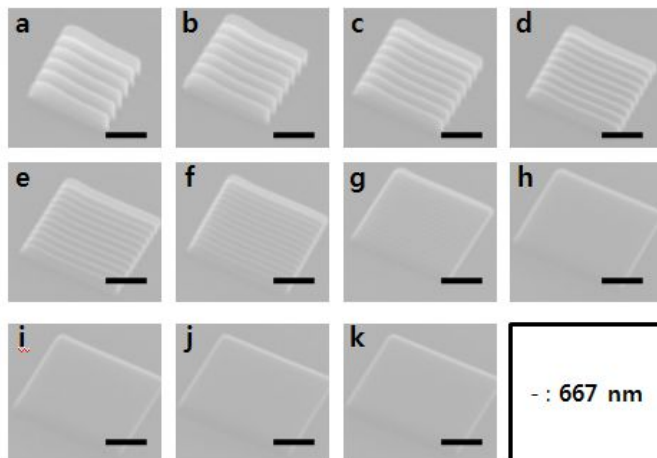


**Figure 4.16** Tilt views of SEM images: Top view of SIM images: the carbon using phenanthrene gas molecules was deposited as a function of beam overlap; a: -900 %, b: -800 %, c: -700 %, d: -600 %, e: -500 %, f: -400 %, g:-300 %, h:-200 %, i:-100 %, j: 0 %, and k: 50 %

When the raster scan was used, the delocalization occurred with many more complexes, as shown in Figure 4.15-17. The widths and lengths changed from their defined 2  $\mu\text{m}$  square boxes as the beam overlap was altered. Specifically, all widths and lengths were less than 2  $\mu\text{m}$  before -100 % and -600 % of beam overlap was reached, respectively. These localizations occurred for two reasons. First, the pixel sizes were different for each square. As explained previously, the pixel sizes were changed from 300 nm to 15 nm to increase the beam overlap from -900 % to 50 %. As a result, the ion irradiation area was restricted. Hence, both the width and length increased continuously as the pixel size decreased (or the beam overlap increased). Second, the gas depletion rate changed with the scan speed in the raster scan routine. The scan speed was decreased with the pixel size as follows: 6  $\mu\text{sec}/\text{line}$ , 7  $\mu\text{sec}/\text{line}$ , 8  $\mu\text{sec}/\text{line}$ , 9  $\mu\text{sec}/\text{line}$ , 11  $\mu\text{sec}/\text{line}$ , 13  $\mu\text{sec}/\text{line}$ , 16  $\mu\text{sec}/\text{line}$ , 22  $\mu\text{sec}/\text{line}$ , 33  $\mu\text{sec}/\text{line}$ , 66  $\mu\text{sec}/\text{line}$ , and 133  $\mu\text{sec}/\text{line}$ , as the beam overlap was increased from -900 % to 50 %. The increase in scan speed caused the gas molecules to dissociate faster. The dissociation was also affected by the raster scan. Because the raster scan caused differences between the width and the length, the adsorbed gas molecules were depleted quickly and continuously from left to right, but slowly and discretely from top to bottom.

In addition, above two reasons influenced the surface morphologies, as shown in Figure 4.16, which changed the localization (deposition) on the left side. Here, the ESAs dissociated more replenished gas molecules, resulting in thicker deposition. This enhanced localization occurred between -900 % and -400 %, when the gas depletion was fast. It accelerated when more single scans were used.

The beam overlap also influenced the divisions of deposits in the vertical direction. These divisions appeared when the beam overlaps were -900 %, -800 %, -700 %, -600 %, -500 %, and -400 %, as illustrated in Figure 4.15~17. The number of divisions was 6, 7, 8, 9, 11, and 13, i.e., the same as the pixel number in the vertical direction. Although the pixel numbers in the vertical

and horizontal directions were the same, divisions were only revealed in the vertical. The ion beam moved continuously in the raster scan routine used in this study. This continuous effect had a dominant influence, even in the smallest beam overlap of -900 %, by depositing horizontal lines. As shown in Figure 4.15~17, no divisions were apparent in the horizontal direction. Moreover, the length of each division increased as the beam overlap decreased from -400 % to -900 %. The measured lengths of each division were 137 nm, 152 nm, 167 nm, 182 nm, 197 nm, and 213 nm for beam overlaps from -400 % to -900 %. Furthermore, decreasing the beam overlap from -400 % to -900 % caused the scan number to increase. Thus, the delocalization was enhanced at local region. However, the divisions of -400 %, -500 %, and -600 % were somewhat different from those of -700 %, -800 %, and -900 %. As shown in Figure 4.15~17, the latter group of cases showed distinct divisions, whereas the former group did not, because the tail of ESAs that was produced by the Gaussian distribution of the ion beam was merged in adjacent rows. This effect increased with the beam overlap, whereas the length of each division for -600 %, -500 %, and -400 % decreased.

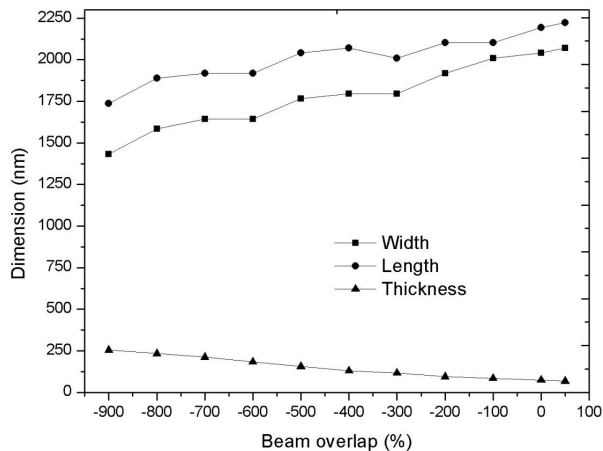


**Figure 4.17** Measured dimensions (width, length, and thickness) and deposition rate as a function of beam overlap.

#### 4.6.2.5 Deposition rates as a function of beam overlap

The deposition rate is an important parameter for the evaluation of FIBID products because it is related to the throughput of FIB induced processing. It is shown as a function of beam overlap in Figure 4.18~19. Overall, it increased as the beam overlap was increased from -900 % to 50 %. The fundamental cause for the increase in deposition rate was the decrease in processing time. The processing time decreased with the scan number. When the scan number was decreased, processing time was reduced by minimizing the ion beam travel time. The ion beam travel time increased with the refresh time. Two types of refresh time occurred: a line refresh time of 16  $\mu\text{sec}$  and an area refresh time of 27  $\mu\text{sec}$ . Although the refresh times were not addressed here, the ion beam had to move to the next irradiation point for each line and area. The cumulative effect of these two refresh times increased when more than a single scan was used. We can compare the two extreme cases where beam overlaps of -900 % and 50 % were applied to a single scan, for example. The times for a single line scan were 6  $\mu\text{sec}$  for -900 % and 133  $\mu\text{sec}$  for 50 %. The line refresh time took a fixed value of 16  $\mu\text{sec}$ , whereas a single area scan took 36  $\mu\text{sec}$  for -900 % and 17,689  $\mu\text{sec}$  for 50 %. The area refresh time was fixed at 27  $\mu\text{sec}$ . This meant that the ion beam had to scan many more times to provide the same amount of ions when a beam overlap of -900 % was used. From this point of view, the increase in scan number, which was determined by the number of irradiation points for a single scan, could play a critical role in decreasing the deposition rate with processing time. The number of irradiation points decreased exponentially with the beam overlap. The processing time inevitably increased with the pixel-to-pixel movement time.

The volumetric changes in Figure 4.19 gave more useful information. Although the deposition rate increased with the beam overlap, the deposition volume started to decrease for beam overlaps over -700 %. The increase in

deposition rate from -700 % to -600 % was determined by the fact that the decrease in processing time was higher than that in volume. The deposition rate was almost saturated for beam overlaps from -600 % to -200 % by the linear correlation between the decrease of both volume and processing time. At less than -200 % beam overlap, the processing time was decreased more than under the other conditions, and the increase in deposition rate resulted finally from -200 % to 50 % of the beam overlap.

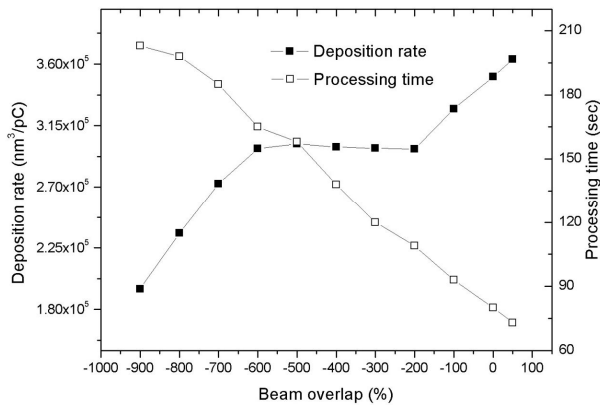


**Figure 4.18** Deposition rate and processing time as a function of beam overlap.

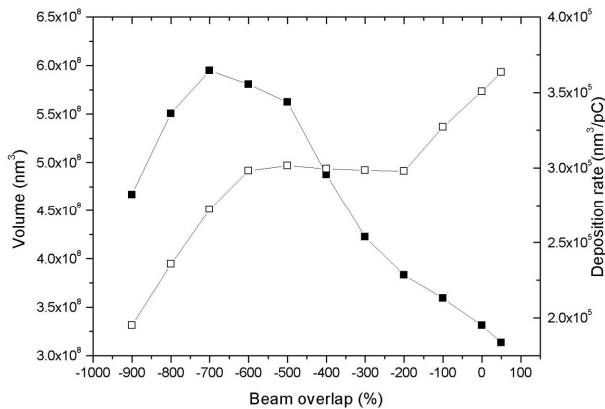


**Figure 4.19** Volumetric changes and deposition rate as a function of beam overlap.

The competition between deposition and sputtering can be seen in Figure 4.19. The volume decreased after it reached a maximum value at -700 % beam overlap. This explained why the deposition became weaker than the sputtering. The distinct division of deposits revealed only -900 %, -800 %, and -700 %, and the divisions were initiated to merge with adjacent lows from -600 % beam overlap. Eventually, the ion beam dissociated the gas molecules uniformly, and hence formed a flat deposition surface. This occurred for beam overlaps under -400 %.

During merging, the localization was in a precursor limited regime [63, 124]. In this regime, the deposition was still dominant. Its importance began to decline as the beam overlap increased from -600 % to 50 % due to an increase in the sputtering. Distinct divisions occurred in the ion beam limited regime. The deposition volume increased because more gas molecules disassociated from -900 % to -700 % beam overlap when the gas flow rate from the GIS was fixed. Finally, the FIBID processing converted the ion beam limited regime into the precursor limited regime at -700 % of the beam overlap.

#### **4.6.2.6 Summary**

Here the influence of beam overlap, which can affect defects generation in FIB fabrication, by conventional scan method was investigated with the help of FIBID.

The delocalization as a function of beam overlap was dependent on the pixel size and the gas depletion rate. When the conventional scan method was used, the continuous effect caused rapid gas depletion, and hence pixel widths that were shorter than their lengths. The increase in scan speed enhanced the localization by replenishing the gas molecules discretely.

In the extremely small beam-overlap cases of -900%, -800%, and -700%, distinct divisions were created. These divisions began to disappear once the

beam overlap was greater than -700% due to the long range dissociation area effect of the ESAs.

The deposition rate increased with the beam overlap because the processing time decreased faster than the deposition volume. Full dissociation occurred at -700% beam overlap. Moreover, competition between deposition and sputtering was observed after full dissociation was reached. This competition became particularly evident when dissociation areas were merged with adjacent rows.

## **4.7 Ion beam path for FIB fabrication**

### **4.7.1 Overview**

The FIB processing adopts the raster scan, described in Figure 4.3(a), for the creation of micro- and nanostructures like other energy beam assisted material processing such as the electron and laser beams. However, the raster scan was not the best way of structuring with the highest precision in FIB fabrication, as reported in [105]. Here, various types of ion beam paths were generated to fabricate the 2.5D target geometry of axis-symmetric structure (hollow circular geometry) with the understanding of nanoscale phenomena discussed in Sections 4.5-6.

### **4.7.2 Generation of ion beam path**

The advanced ion beam paths were suggested by controlling the ion beam paths, as shown in Figure 4.20. Tseven types of scan strategies were generated by utilizing the point-to-point scan style, described in the previous section. Using scan strategies depicted in Figure 4.21, the prerequisite experiments were performed to observed the ion beam path. In order to observe more specifically, the FIBID was applied to this prerequisite experiments. The results were shown in Figure 4.22.

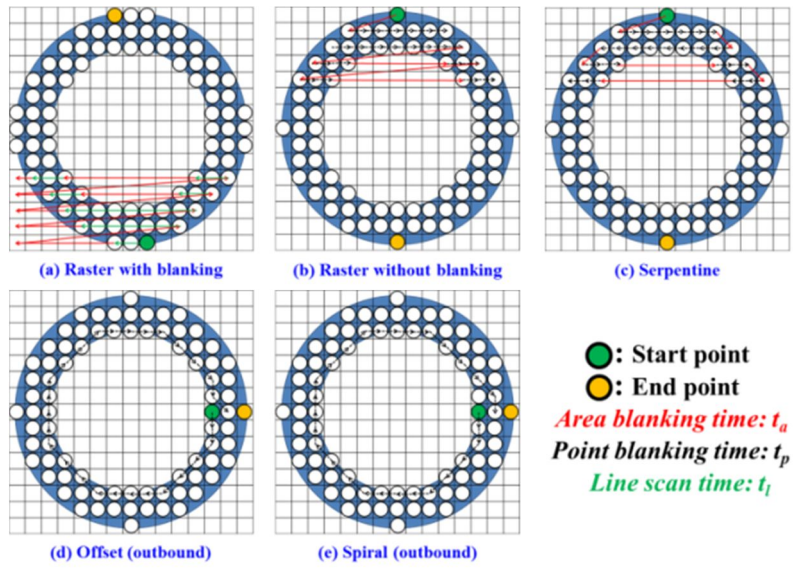


**Figure 4.20** Five types of ion beam paths for hollow circular geometry

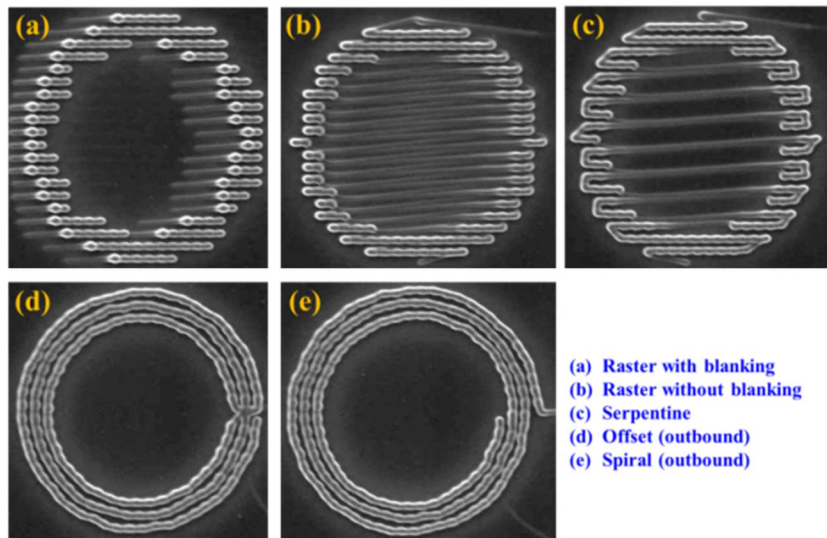


**Figure 4.21** Traces of ion beam paths, depicted in Figure 4.20, by FIBID

### 4.7.3 Experimental conditions

**Table 4.5** Experimental conditions

<b>Parameters</b>	<b>Conditions</b>
Ion specie	Gallium
Accelerating voltage (KeV)	30
Target	Silicon (100)
Ion current (pA)	93
Dwell time ( $\mu$ sec)	5 and 500
Field of view ( $\mu$ m)	24
Pixel size (nm)	30
Beam size (nm)	60
No. of scan	25,000

Through the screening experiments, it is very obvious that ion beam trace affected by the high energetic ion beam can have effects on fabricated geometry. For real experiments, the experimental conditions illustrated in Table 4.5 were applied. Two types of dwell time were also investigated with combination of ion beam path.

### 4.7.4 Surface morphology

The fabrication results according to seven ion paths were shown in Figure 4.22. It can be easily found out the influence of ion beam paths. One of the distinct facts was that the raster scan with/without blanking and the serpentine scan were influenced by the discrete movement of ion beam, resulting in the uneven surfaces along the inner and outer edges. In contrast to these results, the uneven surfaces were not appeared in the offset and spiral scans because ion beam moved along the edges of inner and outer circles in the target geometry.

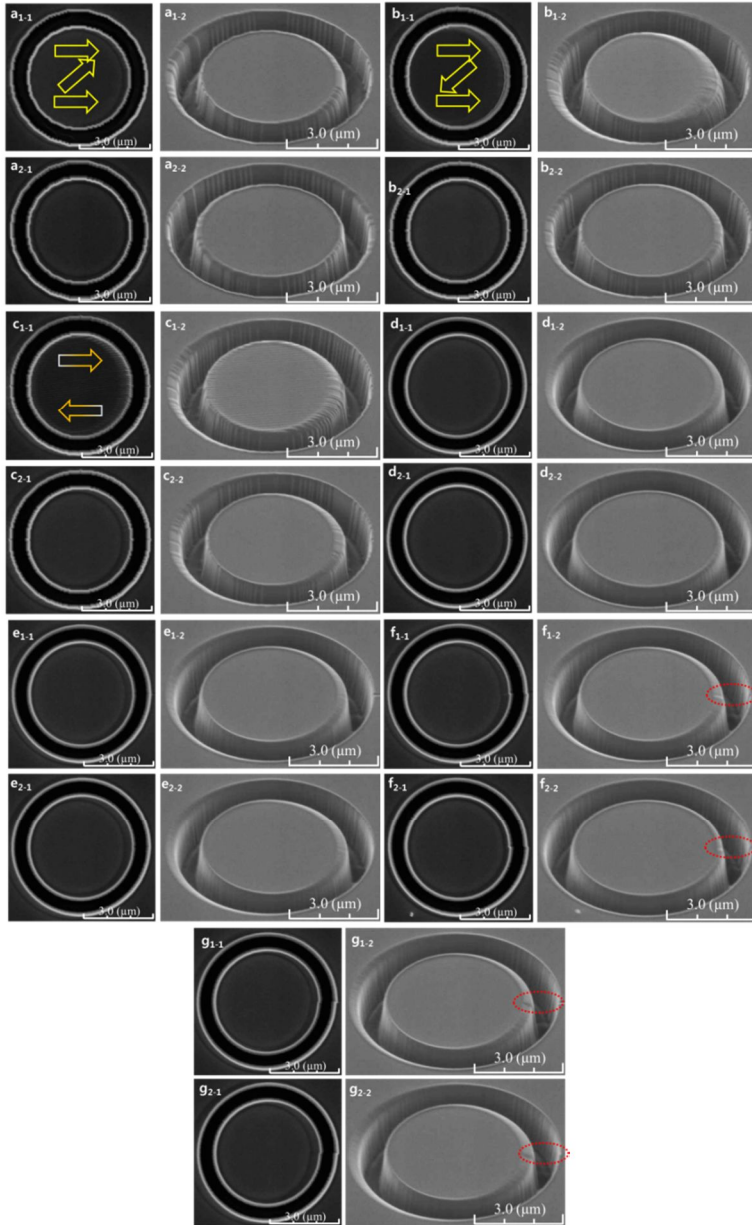


**Figure 4.22** Fabrication results of seven types of scan strategies: (a) raster scan with beam blanking, (b) raster scan without beam blanking, (c) serpentine scan, (d) offset scan (inbound), (e) offset scan (outbound), (f) spiral scan (inbound), and (g) spiral scan (outbound). The former subscripts 1 and 2 represent the 5  $\mu$ sec and 500  $\mu$ sec dwell time, respectively.

Furthermore, the inner edges in raster and serpentine scans were damaged when ion beam moved back to left side to initiate the scan from left side to right side. Even though the surface integrity along edges was good for both the offset and spiral scan, there was a defective structure detected in only case of the spiral scan because its scan start position was different with the scan end point. This difference was well described in Figure 4.21.

The influence of dwell time difference was not clearly showed compared to the influence of ion beam path. One of clear facts was that the damage along the inner edges were reduced with the increment of dwell time because the No. of scan was naturally decreased, as discussed in the section.4.5

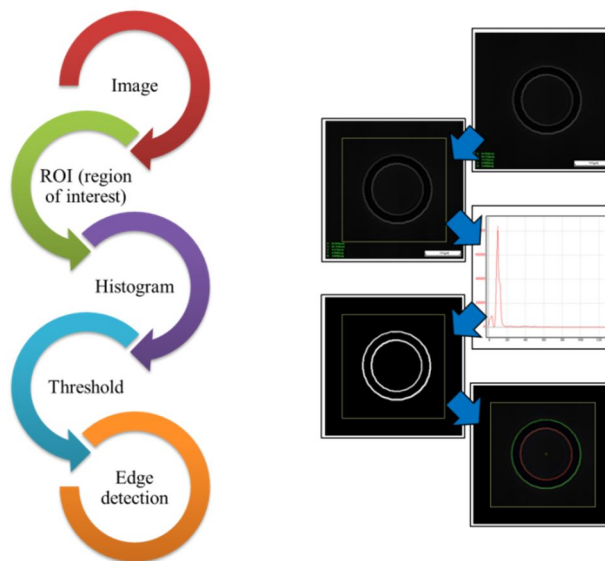


**Figure 4.23** Image processing algorithm for the precision and accuracy measurements of the hollow circular structure

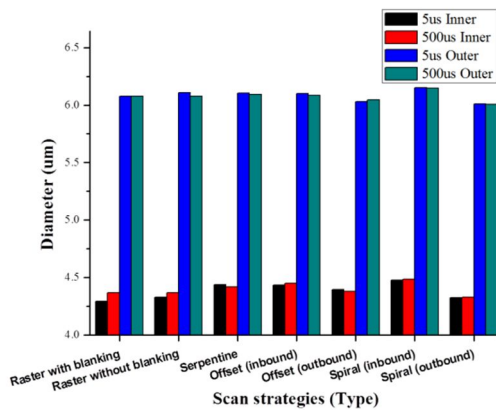
#### 4.7.5 Evaluation of geometrical precision and accuracy

Figure 4.23 represents the image processing algorithm used to measure the

geometrical accuracy and precision. The Otsu's method was used to get threshold value in the region of interest [125]. Then, the edges along the circle on top and bottom surface were detected and measured their numerical values. In terms of accuracy, the roundness of inner and outer diameter on top and bottom surface and the concentricity on top and bottom surface were measured. In terms of precision, the dimensions of inner and outer diameter on top and bottom surface was measured.

#### 4.7.6 Evaluation of geometrical precision

Precisions of inner and outer diameters on top/bottom surfaces were shown in Figure 4.24 and 25. On top surface, as shown in Figure 4.24, the inner diameter was usually smaller than the targeted diameter of 4.5  $\mu\text{m}$ , and the outer diameter was usually bigger than the targeted diameter of 6  $\mu\text{m}$ . These tendencies were the results influenced by the localization of ion beam. These tendencies were totally inversed on bottom surface, as shown in Figure 4.25 because the structures were narrowed by applying more ion dose, resulting in the slant walls in the direction of depth. There were no significant influences of the ion beam path and the dwell time detected, as shwon in Figure 4.24 and 25.



**Figure 4.24** Precision of inner and outer diameters on top surface

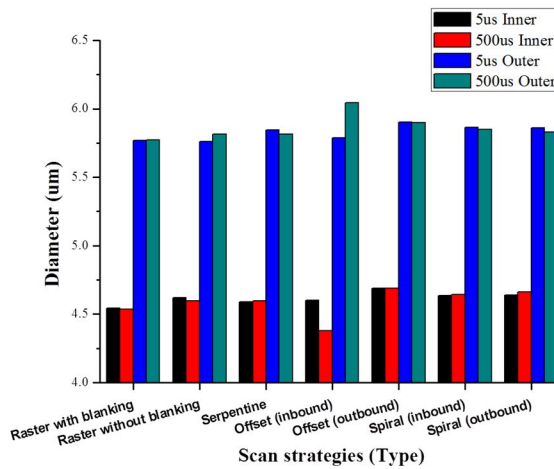


**Figure 4.25** Precision of inner and outer diameters on top surface

#### 4.7.7 Evaluation of geometrical accuracy

Unlike results in precision, the accuracies were quite influenced by both ion beam path and dwell time, as shown in Figure 26-31. In Figure 4.26 and 27, the roundnesses of inner and outer diameters on the top surface were improved by utilizing offset and spiral scans compared to raster and serpentine scans because the offset and spiral did not include the linear discrete ion beam movements, as discussed in the previous sections. Furthermore, the return of ion beam discussed in the section 4.7.4 degraded the accuracies of raster and serpentine scans. This degradation of surface morphology is easily found out in Figure 4.22(a-c). On the contrary, the roundnesses of inner and outer diameters on the bottom surface did not have the same tendency. It might be caused by the enhancement of nanoscale phenomena like material redeposition and self-focusing at the edges on the bottom surface.

In case of concentricity, the concentricity was very accurate as shown in Figure 30 and 31. Most critical results were based on the nanoscale defective phenomena, resulting in the complexes of concentricity on the bottom surface.

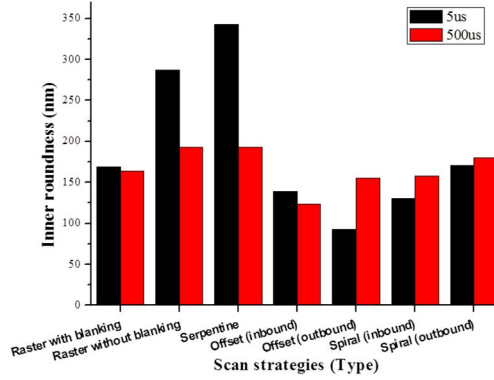


Figure 4.26 Roundness of inner diameter at top surface

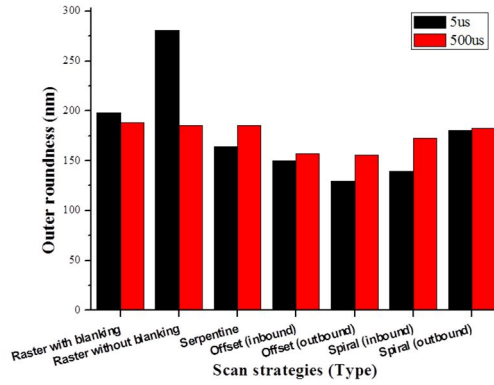


Figure 4.27 Roundness of outer diameter at top surface

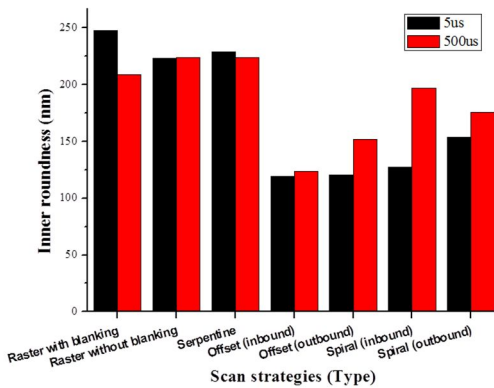


Figure 4.28 Roundness of inner diameter at bottom surface

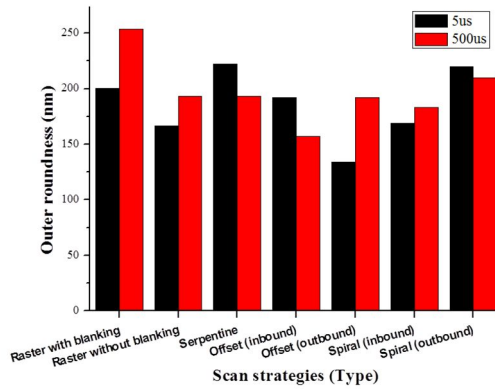


Figure 4.29 Roundness of outer diameter at bottom surface

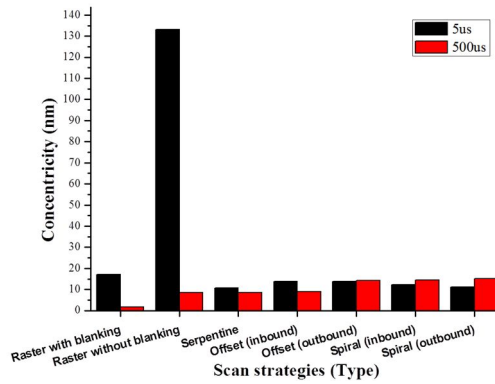


Figure 4.30 Concentricity between inner and outer circles at top surface

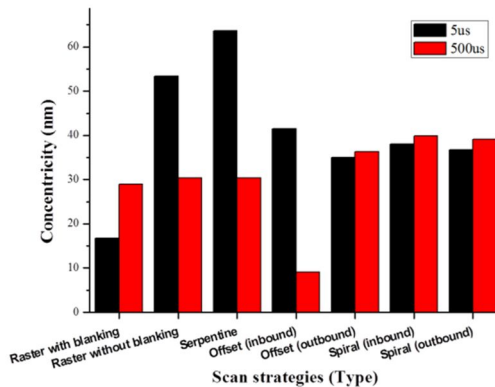


Figure 4.31 Concentricity between inner and outer circles at bottom surface

### 4.7.8 Summary

Through a series of experiments influenced by the different types of ion beam paths, the geometrical precision and accuracy had been influenced. With the comparison of surface morphologies of fabricated structures, it is much clearer that the geometrical precision and accuracy can be optimized by controlling the ion beam path after selection of optimum ion beam processing parameters such as dwell time and bema overlap.

## 4.8 Advanced fabrication strategy for 3D nanostructures

### 4.8.1 Overview

The 3D fabrication methodology can reduce the complexity of process design. For example, Figure 4.32 describes the reduction of complexity in process design. This indicates that if a serial process is possible with FIB after full deposition of multilayer with two more materials it can reduce the process design complexity. Currently, two methodologies (Figure 3.33(a) and (b)) have been introduced for fabricating mentioned 3-D by Vasile *et al.* [126, 127] and Fu *et al.* [128]. Vasile *et al.* introduced a profile control by controlling the dwell time on the pixel, while Fu *et al.* employed two-dimensional (2-D) slice-by-slice method.

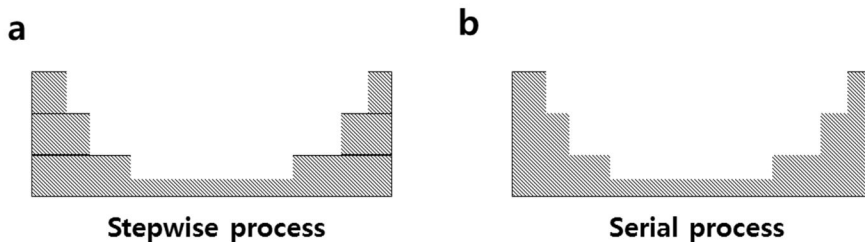


**Figure 4.32** Comparison of complexity of process design: (a) stepwise process and (b) serial process

Here, the 2D slice-by-slice method developed by Fu *et al.* [128] was modified by repeating the ion beam scan of entire discrete slices over a thousand times to fabricate a circular conical shape. It was combined this with a spiral scan, which has been applied to produce accurate circular patterns [105], as a part of the vector scan instead of using a raster scan. In addition, the ion beam conditions and processing parameters were chosen carefully. Consequently, circular conical structures as a mould were fabricated as a function of ion dose for dwell times of 0.5, 1.0 and 2.0  $\mu\text{s}$ , and their dimensions and etch rate (sputtering yield) were evaluated. In addition, a full 3D geometry was replicated from PDMS and PUA for the verification of its geometry.

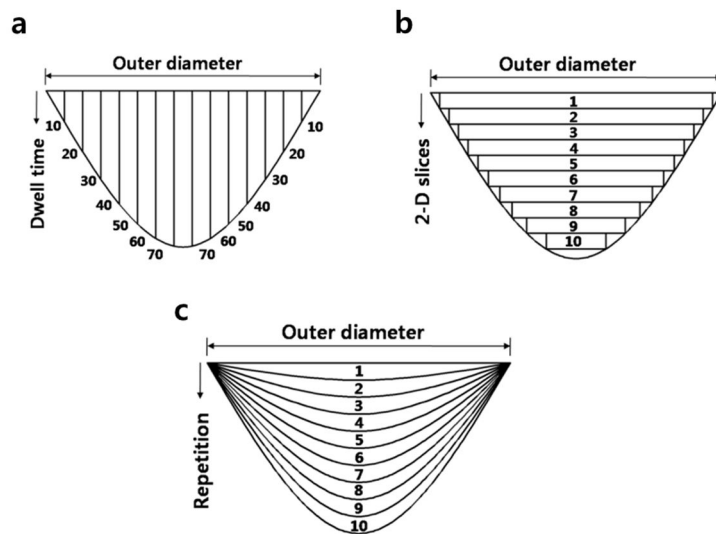


**Figure 4.33** Three different methodologies for 3D geometry: a) Vasile's method: sputtering by changing the dwell time on the pixel, b) Fu's method: sputtering the sequential 2D slice by slice, and c) continuous slicing method (CSM): it is modified by repeating the Fu's method continuously by reducing the ion dose for each one slice, while the total ion dose is the same as Fu's method.

### 4.8.2 Fabrication strategy

The scan strategy is determined by both the target geometry and scan method. For example, a circular pattern has a better quality with a more vertical sidewall, while a spiral scan reduces material redeposition [105]. In this study, we developed a continuous slicing method (CSM), which was modified from Fu *et al.* [128], combined with an ion beam path that spirals inward, as illustrated in Figure 4.20 and 21(e).

This assumes four advantages when repeating a discrete process continuously: 1) the spiral scan results in almost the same material redeposition in the radial direction, unlike a raster scan; 2) stair-step structures are avoided because the proposed method does not use a discrete process, unlike the method of Fu *et al.* (Figure 4.33(b)); 3) it can reduce material redeposition by repeating the discrete 2D slice continuously, as shown in Figure 4.33(c), because it directly sputters the already sputtered region continuously; and 4) it can improve the sputtering yield as a function of the incident angle of ion beams compared with the method of Fu *et al.* [128] due to a self-focusing effect [129-131], while increasing the sputtering yield by repeating more scans because of the more inclined sidewall angle, as shown in Figure 4.33(c). This sputtering yield usually increases from  $0^\circ$  to  $80^\circ$  [108, 127, 130]. The simple comparison results for Figure 4.33(b) and (c) were shown in Figure 4.34(a) and (b), respectively. As seen in this figure, it was found that the CSM could easily improve the surface integrity.

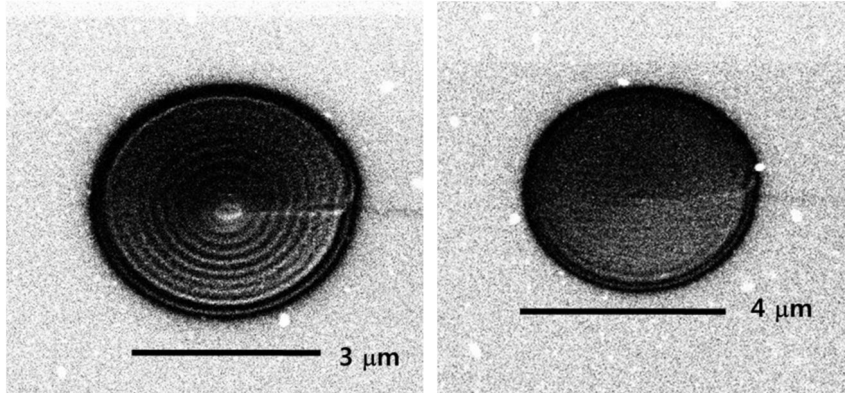


**Figure 4.34** Comparisons between Fu's method and CSM; (a) has stair-step structures (defective structure) and (b) has no defective structure

### 4.8.3 Geometry from micro-mould

To evaluate the fabricated 3D structure, the definition in Figure 4.35 was introduced. The diameters of all fabricated moulds were measured directly using scanning ion microscopy (SIM), and were approximately  $4\ \mu\text{m}$  for all moulds, as shown in Figure 4.35. Therefore, the diameter was not evaluated further here. For depth profiling, a 3D optical profiler (NX 9100; Veeco) was used. The depth and sputtering yield of 3D structures are shown in Figure 4.36, respectively. The fabricated depth increased linearly as a function of ion dose for all three dwell times is shown in Figure 4.36. For a dose of  $0.94 \times 10^{17}\ \text{ions/cm}^2$  and dwell time of  $2.0\ \mu\text{s}$ , an unexpected result occurred, which is explained later section. The sputtering yield decreased exponentially for all dwell times as shown in Figure 4.36.

As shown in Figure 4.35, a nanoscale rim edge was usually generated by the tail of the Gaussian ion beam [108]. In addition, material redeposition in a radial manner contributed to this rim. The height of the rim was not measured due to limitations of the 3D optical profiler.

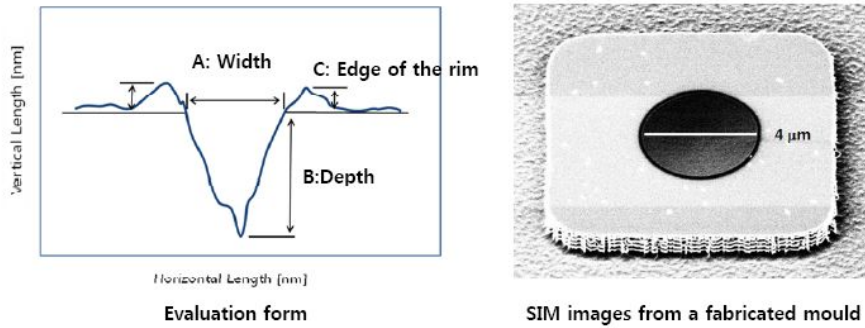


**Figure 4.35** Definitions for a fabricated mould, and the SIM image of a fabricated mould: all the fabricated moulds have a diameter of about 4  $\mu\text{m}$ .

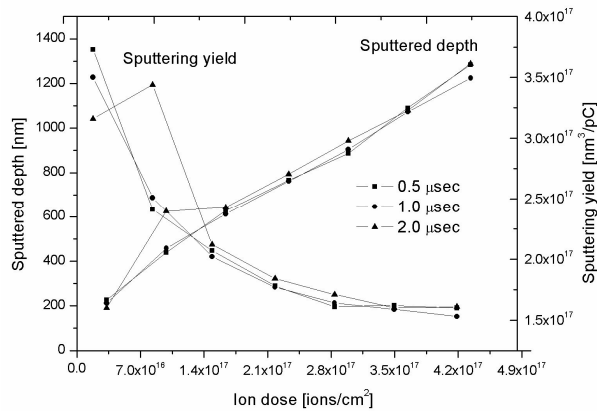


**Figure 4.36** Mould depth and sputtering yield as a function of ion dose for three specific dwell times of 0.5  $\mu\text{sec}$ , 1.0  $\mu\text{sec}$ , and 2.0  $\mu\text{sec}$ .

#### 4.8.4 Geometry from polymer replication

For evaluation of 3D geometry, the polymer replication was implemented. To build polymeric microstructures from the moulds, two types of polymer were used: PDMS and PUA. After preparing a silicon micro-mould, a mixture of 10:1 PDMS pre-polymer (Sylgard 184 silicon elastomer; Dow Corning) and curing agent was poured into the micro-mould and heated at 70  $^{\circ}\text{C}$  for 1

hour. The cured PDMS was then peeled from the mould. Figure 4.37 shows the resulting replica using a maximum ion dose of  $4.14 \times 10^{17}$  ions/cm<sup>2</sup>. The height of the replicated microstructure was much smaller than the depth of the fabricated mould, which was around 1283.25 nm (Table 4.6) due to difficulty in replicating the microscale structures.

PUA was used to obtain complete replication of a microscale 3D structure. This polymer was recently introduced for sub-100-nm patterning. After preparing a silicon micro-mould, the ultraviolet (UV)-curable precursor was dispersed in the mould and then cured by exposure to UV light for 20 s ( $\lambda = 250\text{--}400$  nm, dose = 100 mJ/cm<sup>2</sup>). As shown in Figure 4.38 and Table 3.5, polymeric microstructures were replicated successfully and had good physical integration. As mentioned in previous section, an unexpected result at a mould depth of 642.7 nm was observed. However, Table 4.6 confirmed that this datum was a measurement error as the height was 364.7 nm on measuring the replicated microstructure. Therefore, the height of the polymeric microstructures increased linearly, as shown in Table 4.6.

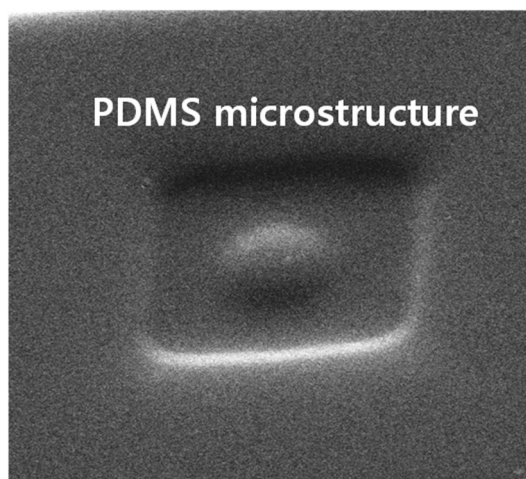


**Figure 4.37** Polymeric microstructure (PDMS) replicated from silicon micro-mould in case of highest ion dose case of  $4.13 \times 10^{17}$  ions/cm<sup>2</sup>, having a depth of 1283.25 nm.

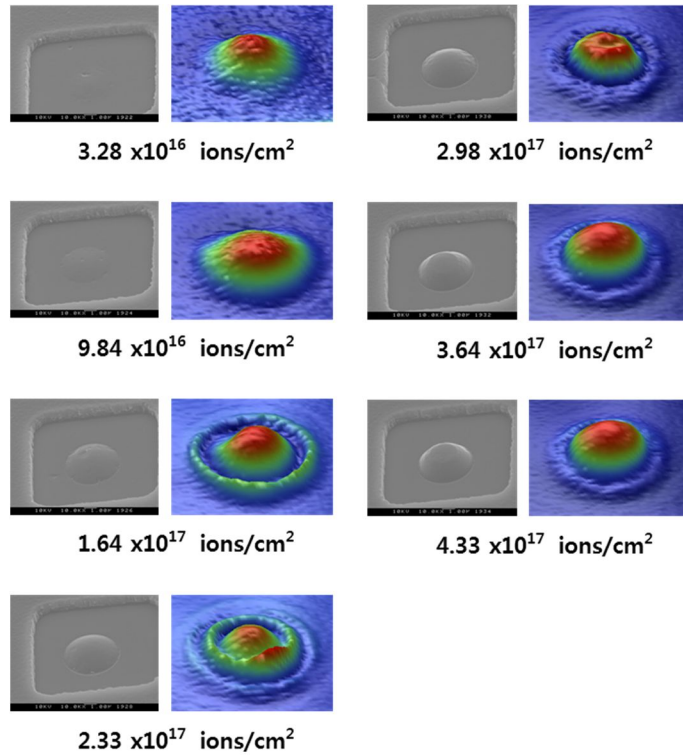


**Figure 4.38** 3D optical surface profiles replicated from PUA microstructures

**Table 4.6** Comparisons between fabricated moulds and replicated PUA microstructures

Ion dose (ions/cm <sup>2</sup> )	Dwell time (µsec)					
	0.5		1		2	
	Depth (nm)	Height (nm)	Depth (nm)	Height (nm)	Depth (nm)	Height (nm)
0.31E+17	225.95	209.5	212.1	205.2	191.6	189.5
0.94E+17	438.95	412.1	457.3	348.2	624.7	364.7
1.56E+17	627.9	622.2	611.65	607.8	642.65	620.6
2.23E+17	766.55	704.9	761.45	672.2	793.6	692.5
2.85E+17	886.7	767	904.1	804.5	943.5	838
3.48E+17	1090.6	1076.6	1073.2	1022.7	1079.5	1018.5
4.14E+17	1283.25	1227.4	1224.75	1146.7	1288.75	1237.1

#### 4.8.5 Summary

The scanning strategy that combines a continuous slicing method with a spiral scan has four potential advantages: it results in the redeposition of almost the same amount of material in a radial direction, avoids forming steps, reduces material redeposition and enhances sputtering. With this strategy, a microscale mould with a circular conical structure was fabricated on a silicon substrate as a function of ion dose for dwell times of 0.5, 1.0 and 2.0  $\mu\text{s}$ . The depth of the mould increased as a function of ion dose for all dwell times, while the sputter yield decreased. Dwell time had no specific effect. Using the fabricated moulds, PDMS and PUA polymeric microstructures were replicated. The experiments showed that PDMS is not suitable for circular conical structures at a microscale, while PUA gave almost perfect replicas from the fabricated silicon moulds. Using PUA, the resolution of a circular conical polymeric structure was tested, but a more careful replication experiment is needed to define the maximum resolution exactly.

# 5 Nanostructuring by 3D printing process

## 5.1 Overview

In this chapter, the nanostructuring by nanoscale 3D printing process has been investigated by proving the manufacturing capability of 3D nanostructures with multimaterials with two processes of both NPDS and FIB. In the regime of nanoscale 3D printing process, building 3D nanostructures with multimaterials has to take into considerations of the two precision and two accuracy issues, as pointed out at the end of the section 2. On the basis of Figure 3.2 in section 2, these target geometries were extended and proposed to depict the 3D printing process, as shown in Figure 5. 1.

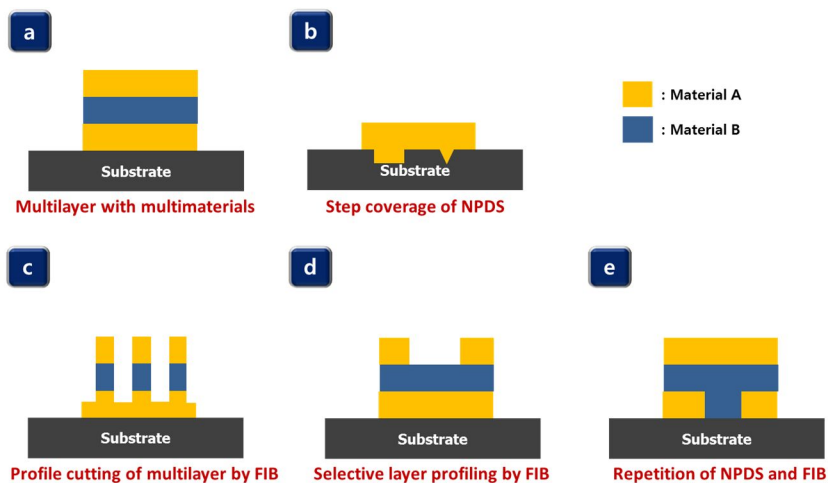


**Figure 5.1** Target geometries for depicting the nanoscale 3D printing process integrated by NPDS and FIB

Based on Figure 5.1, herein, the multilayer structures with multimaterials, nanoscale profiling of multilayer structures by FIB, selective profiling of

multilayer structures and repetition of both NPDS and FIB processes were implemented.

## 5.2 Multilayer structure with multimaterials

Sn (metal) and  $\text{Al}_2\text{O}_3$  (ceramic) were deposited as a nanoscale multilayer structure on Si substrate using NPDS. The order of deposition was Sn,  $\text{Al}_2\text{O}_3$  and Sn on the substrate (Sn/ $\text{Al}_2\text{O}_3$ /Sn on Si). Particles used in here were illustrated in the Section 3. This sandwich structure can be used as a nanoscale conductor; Figure 5.2 shows a description of the multilayer structure with multimaterials.

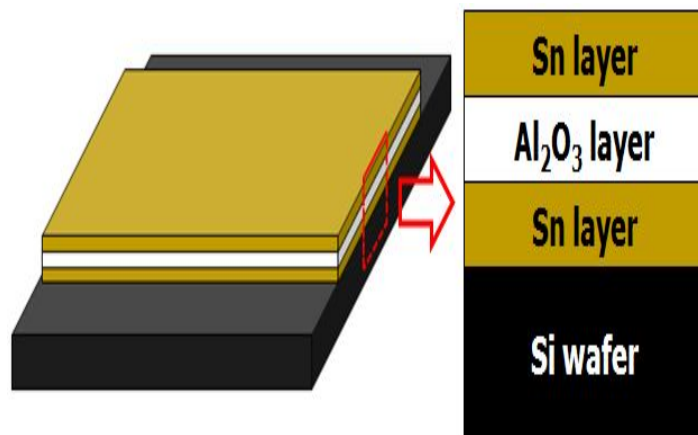


**Figure 5.2** Description of multilayer structure with multimaterials of Sn and  $\text{Al}_2\text{O}_3$  by NPDS

Table 5.1 lists the process parameters used to deposit both powders. A converging-diverging nozzle with throat dimensions of  $1 \times 1 \text{ mm}^2$  and exit dimensions of  $1 \times 3 \text{ mm}^2$  was utilized. Both particles were successfully deposited using the same process parameters.

**Table 5.1** Experimental conditions for multilayer structure with multimaterials

Parameter	Value
SoD (mm)	5.0
Compressor pressure (MPa)	0.4
Chamber pressure (MPa)	0.002 ~ 0.005
Feed rate (mm/s)	0.05
Flow rate (l/min)	15 ~ 20
Carrier gas	Air

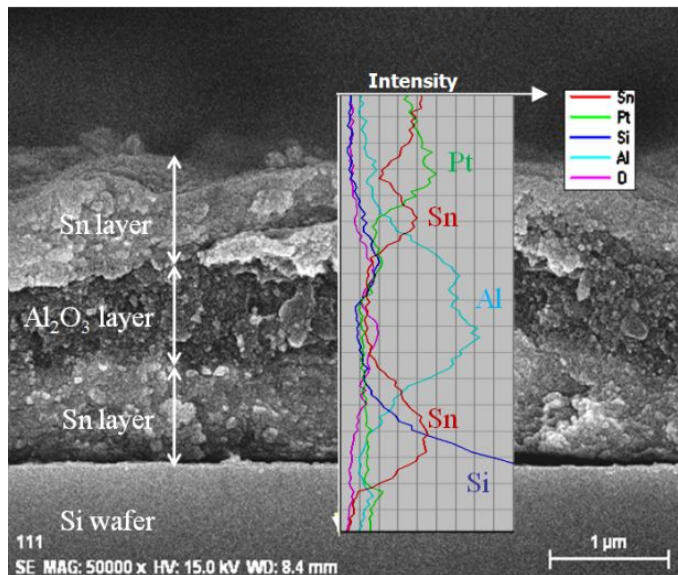


**Figure 5.3** FE-SEM image of a cross-section of multilayer system, Sn/Al<sub>2</sub>O<sub>3</sub>/Sn on Si, with the line EDS result.

The dense film was deposited as shown in Figure 5.3. Figure 5.3 shows a cross-section image of the Sn/Al<sub>2</sub>O<sub>3</sub>/Sn on Si. The multilayer had a thickness of about 2.2 μm. The top layer of the multilayer structure can be distinguished by cracking due to specimen fracture, but the rest of the border between the Al<sub>2</sub>O<sub>3</sub> and Sn layers was indistinguishable. To confirm the components of

each layer, EDXS along a line presented the inset of Figure 5.3. In the substrate, measurements revealed that the intensity of Si was dominant, with large amounts of Sn in the first layer, Al in the middle layer, and Sn and platinum (Pt) in the top layer. This Pt was used as a conductive coating for FE-SEM without a charging effect. When a high energetic electron beam (15 keV) was scanned across the cross section of Sn/Al<sub>2</sub>O<sub>3</sub>, the contrasts of each layer became different due to the material dependent secondary electron yield, and the layers could be distinguished by the FE-SEM image.

### 5.3 Step coverage of NPDS in the nanostructured substrate

The step coverage of NPDS is very important to check the capability of layering up of multimaterials in the FIB profiled nanostructure. This step coverage of NPDS was investigated using the nanostructured substrate fabricated by FIB.

#### 5.3.1 Fabrication of nanostructured substrate by FIB

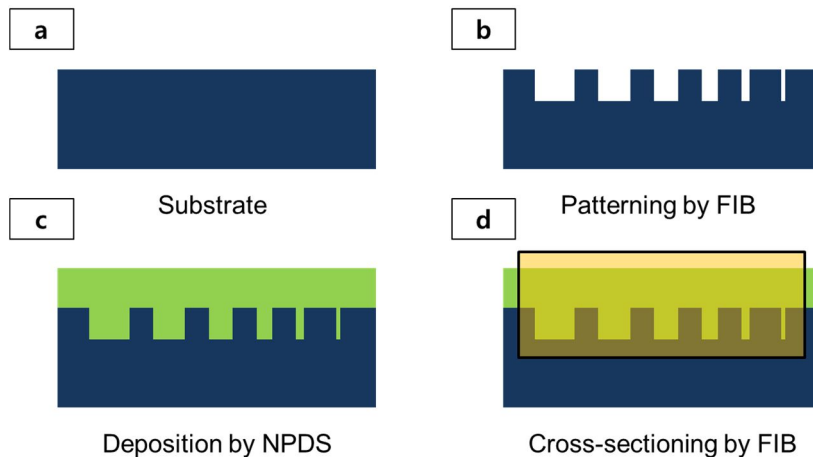


**Figure 5.4** Experimental procedures for metal and ceramic nanofabrication on patterned substrate

**Table 5.2** Experimental conditions for nanostructured substrates

Parameter	Value
Ion species/energy	Ga @ 30 kV
Probe current	90 and 270 pA
Dwell time	2 $\mu$ sec
Beam overlap	0
Field of view	24 $\mu$ m
Pattern width	1,000, 800, 600, 400, 200, 100
Ion dose	1.33, 2.68, 4.03, 5.37, and 6.72 x $10^{18}$ ions/cm <sup>2</sup>

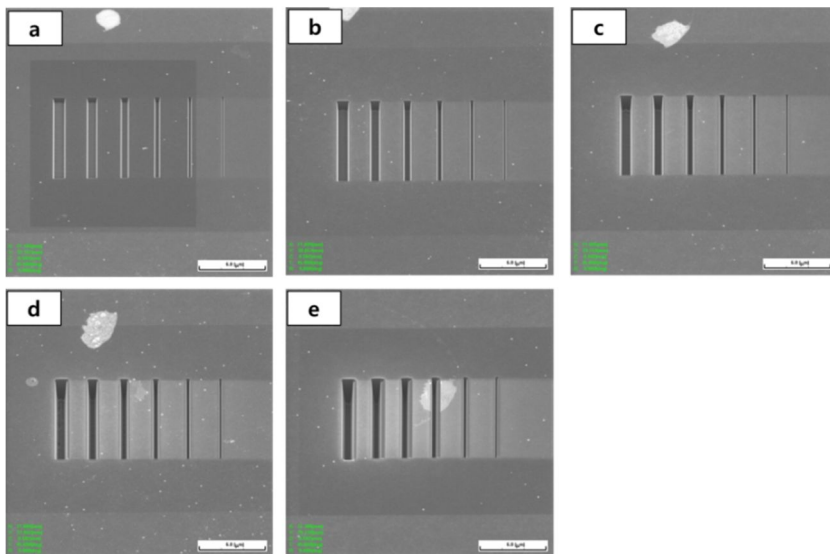


**Figure 5.5** FIB fabricated nanoscale patterns on silicon substrates as function of pattern width and ion doses (for depth control)

### 5.3.2 Deposition of metal and ceramic films by NPDS

For the metal and ceramic particles' deposition, the Sn, TiO<sub>2</sub> and Al<sub>2</sub>O<sub>3</sub> were adopted, and they were deposited with the experimental conditions in

Table 5.2

**Table 5.3** Experimental conditions for metal and ceramic deposition on the nanostructured substrate

Parameters	Conditions	Parameters	Conditions
Material	Sn	Feed rate	0.025 mm/s
Nozzle	1 x 3 mm <sup>2</sup>	Stand-off distance	3 mm
Input pressure	0.3 MPa	Temperature	23.5°C
Chamber pressure	-0.097 MPa	Humidity	57%

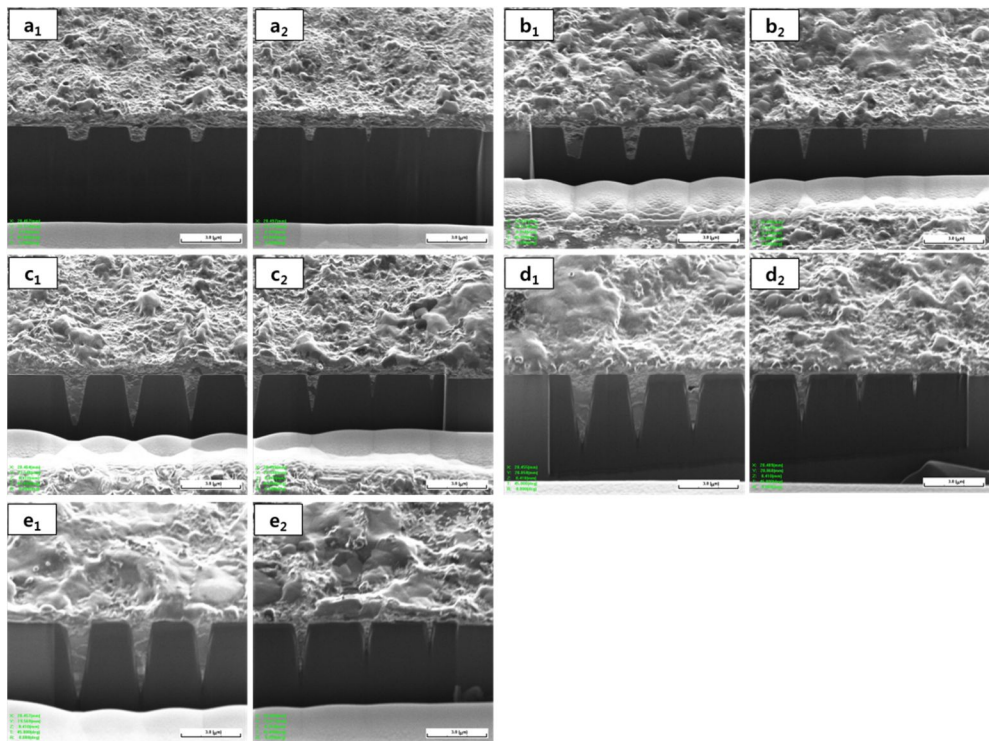


**Figure 5.6** Cross-sections of Sn metallic film on the nanostructured Si substrate: the applied ion doses were increased from (a) to (e) as following; 1.3, 2.7, 4.0, 5.3, and  $6.7 \times 10^{18}$  ions/cm<sup>2</sup>.

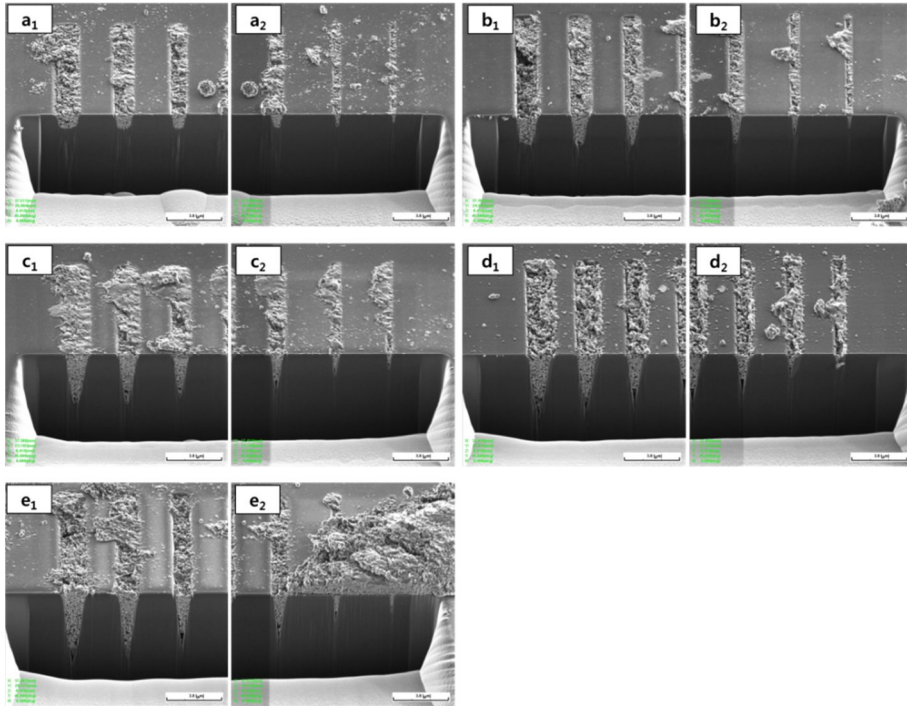


**Figure 5.7** Cross-sections of nanoporous structures of TiO<sub>2</sub>: the applied ion doses were increased from (a) to (e) as following; 1.3, 2.7, 4.0, 5.3, and 6.7 x 10<sup>18</sup> ions/cm<sup>2</sup>.

### 5.3.3 Surface morphology of metallic and ceramic nanostructures

The FIB cross-section technique was utilized to check the step coverage of metal and ceramic particle deposition by NPDS. Cross-sections for metal and ceramic films were shown in Figure 5.6-8. These images were taken by SIM. In these figures, it was found out that metal and ceramic particles were deposited well inside the nanostructured substrates, even in the highest dose case. Especially, the Sn particle, which is much bigger than the nanostructures, were also covered the nanostructured substrate with densely. The different contrasts in any Sn structures were originated from the crystallographic differences by the plastic deformation (see Chapter 6). On

the contrary, there were small portion of porous region observed in case of ceramic films of  $\text{TiO}_2$  and  $\text{Al}_2\text{O}_3$ , as shown in Figure 5.7-8. The detailed explanation of interfaces of each film in metal and ceramic films on nanostructured substrates were dealt in the Chapter 6.

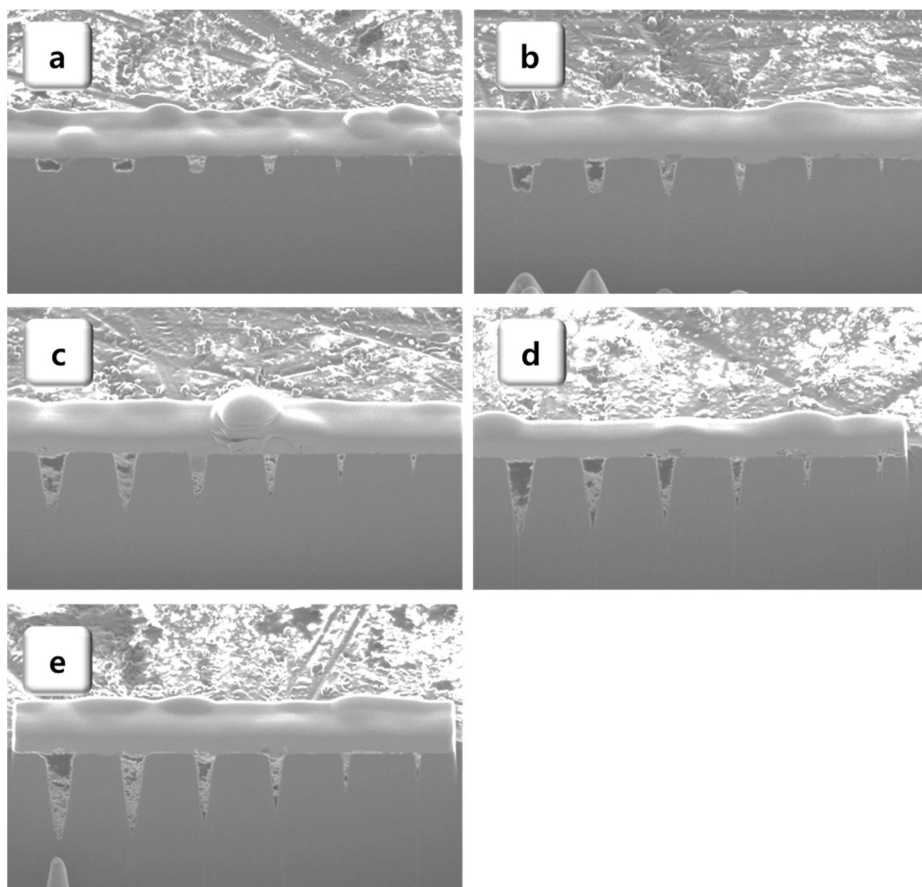


**Figure 5.8** Cross-sections of nanoporous structures of  $\text{Al}_2\text{O}_3$ : the applied ion doses were increased from (a) to (e) as following; 1.3, 2.7, 4.0, 5.3, and  $6.7 \times 10^{18}$  ions/ $\text{cm}^2$ .

The function of ion dose with the width of nanostructured pattern was shown in Figure 5.9. The variation of ion dose resulted in the variation of depth of nanostructured pattern. In the lowest ion dose case, the depths in

nanostructured patterns were not significantly influenced by the widths of nanostructured patterns. This resulted in the quite uniform depth of nanostructured pattern. However, the depths were initiated to make variations by increasing the ion dose, and this variation had critical influenced on the smallest pattern width because the nanoscale phenomena, discussed in the Chapter 4, took place and highly influenced in the smaller nanostructure. In summary, the depth of nanostructured pattern was increased by increasing the ion dose and the width of nanostructured pattern.

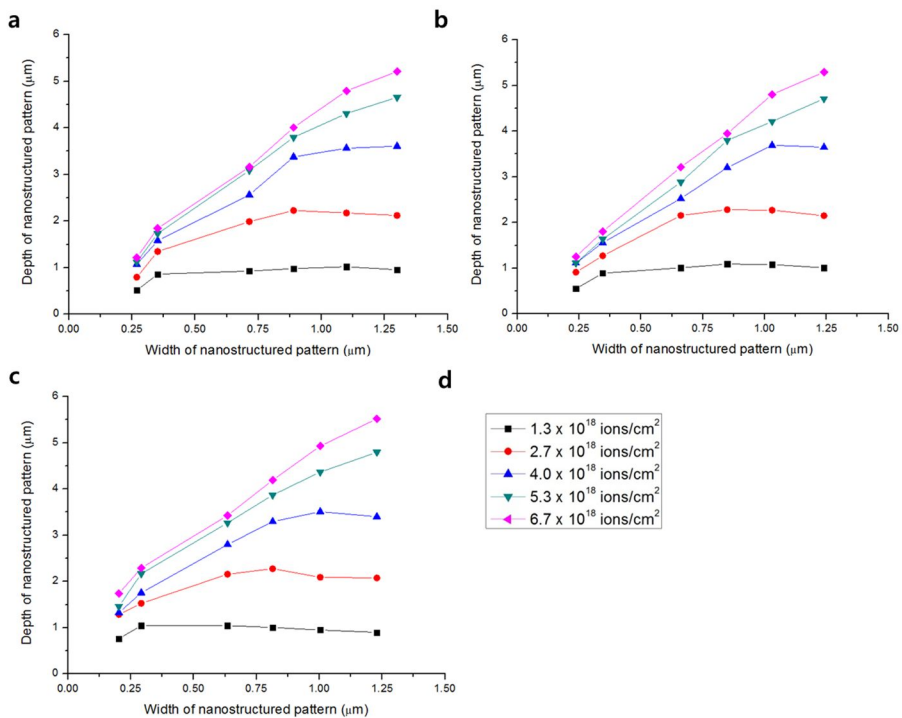


**Figure 5.9** Depths as functions of widths and ion doses in the nanostructured patterns: (a) Sn, (b) TiO<sub>2</sub>, and (c) Al<sub>2</sub>O<sub>3</sub>.

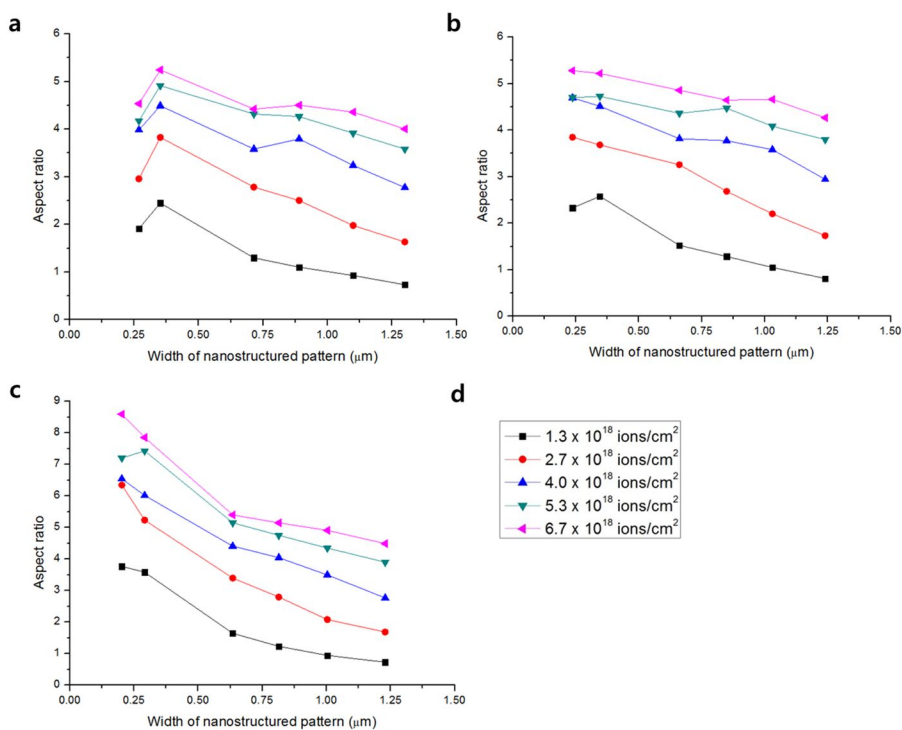


**Figure 5.10** Aspect ratios functions of widths and ion doses in the nanostructured patterns: (a) Sn, (b) TiO<sub>2</sub>, and (c) Al<sub>2</sub>O<sub>3</sub>.

### 5.3.4 Aspect ratio of metal and ceramic nanostructure

From the results in Figure 5.9, the aspect ratios for each particle were given in Figure 5.10. From Figure 5.10, normally the high aspect ratio was appeared in the lowest ion dose of  $1.3 \times 10^{18}$  ions/cm<sup>2</sup> except for Sn case (Figure 5.10(a)). The maximum aspect ratios of Sn, TiO<sub>2</sub> and Al<sub>2</sub>O<sub>3</sub> were 5.3, 5.4 and 6.8, respectively. Actually it can be stated that the types of particle materials and NPDS itself were not make a variation in the aspect ratio because all the particles were well deposited inside the nanostructured substrate. Thus, the difference of the aspect ratio was originated from the results of FIB nanostructuring because the precision and accuracy could be differed even though the same process parameters were applied. This difference was also

highly influenced by the defective phenomena in FIB. Thus, it can be assumed that the NPDS can create the high aspect ratio structure more than this experiment if the substrate is well prepared with high aspect ratio.

#### 5.4 FIB profiling of multilayer structure with multimaterials

Normally FIB can remove any solid target, but it is important to test the machinability of multilayer structures deposited by NPDS. For this experiment, ion beams were irradiated under conditions of 30 kV of gallium ion energy, 270 pA of ion current, and 5  $\mu$ s of dwell time. FIB can etch a profile based on an image. Line and rectangular shapes were used for profile cutting, as shown in Figure 5.11. The processing time was less than 10 min for complete profile cutting.

Line and rectangular extrusions were fabricated as shown in Figure 5.12-13. Both results revealed a clear borderline of Si wafer, and three layers could be distinguished. Some small flaws were observed on the top layer of the line shape. For the rectangular shape, carbon deposition in FIB was carried out to protect the top layer from the ion beam.

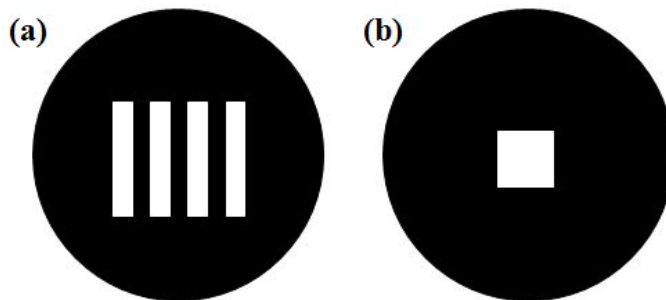


**Figure 5.11** Images used for FIB profile cutting: (a) line shape and (b) rectangular shape.

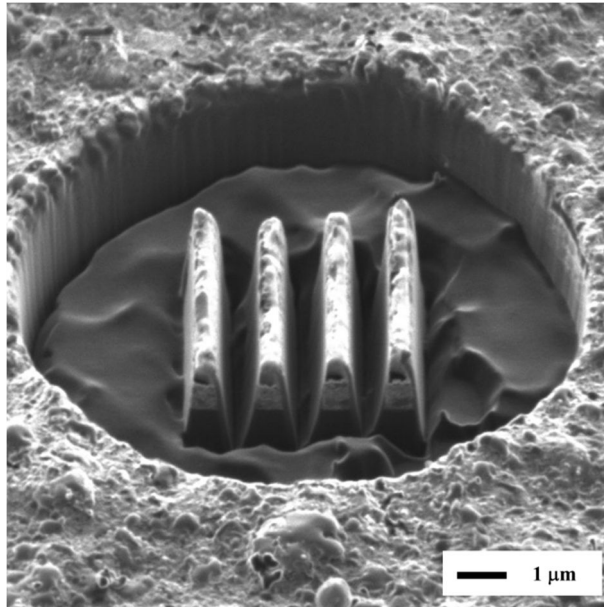


**Figure 5.12** Fabrication of nanowalls in the Sn/Al<sub>2</sub>O<sub>3</sub>/Sn on Si: it was observed at a 30° tilt angle in SIM.

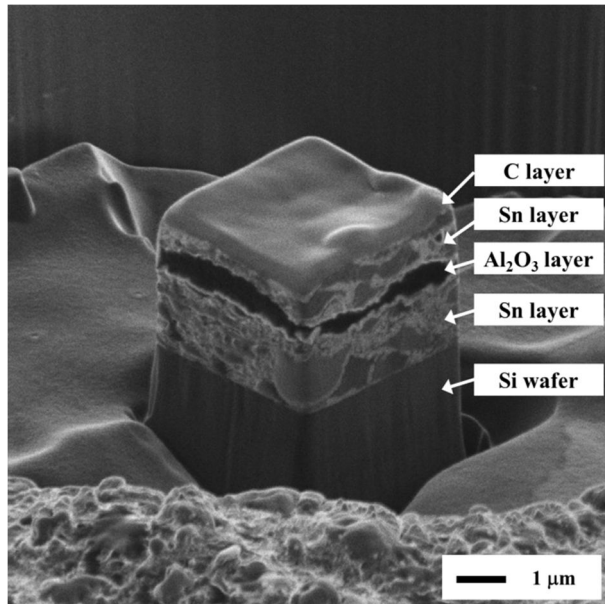


**Figure 5.13** Fabrication of micropillar in the Sn/Al<sub>2</sub>O<sub>3</sub>/Sn on Si: it was observed at a 45° tilt angle in SIM.

## 5.5 Selective FIB profiling of multilayered structure

As shown and discussed in Chapter 3, the NPDS deposited films had a lack of uniformity. This non-uniformity always brings about the difficulty of structuring of wanted structures. For instance, FIB sputtering brought about the irregularity of surface, as shown in Figure 5.14, because of the intrinsic characteristics, milling rate dependent on crystal and surface morphology, related to the electrical structure at the sharp apex. From this example it could find out that the milled depth was different even though the same amount of ion doses was applied evenly when milling the Sn film on substrate.

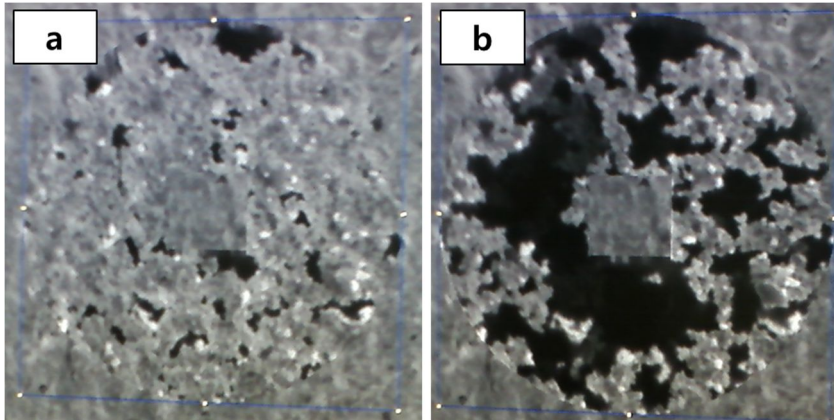


**Figure 5.14** Difference of FIB milling rate on Sn film deposited by NPDS

### 5.5.1 Algorithm for selective FIB profiling

In order to get over this difficulty, the selective FIB profiling method was suggested here. The conventional raster scan which synchronized with image scan signal can make the real time monitoring of FIB processing. With the adoption of the real time monitoring of FIB milling, the method which called as the selective profiling technique was proposed. The algorithm for the selective profiling technique is illustrated in Figure 5.15. Figure 5.16 is the

example of definition of milling area in the process of FIB milling. The right-top bitmap image can be used for selective FIB profiling. Principal mechanism of this method is the redefinition of sputtering region from the contrast difference. This contrast difference can tell differences of depth profile information in qualitatively. Figure 5.14 is one of the examples of contrast difference.

Furthermore, one of the leading advantages of this contrast based real time monitoring is that it can make a distinct each layer in the multilayered systems because the contrast different also comes from the secondary electron yield which based on the material characteristics. This kind of identification of distinct method is called ‘*end-point detection*’. This end-point detection method is very familiar in the field of the sputtering yield measurement for multilayered systems. However, it always depends on the secondary electron emission signal, not by the real time monitoring. Here, the real time monitoring of ion beam sputtering make sure that it can make the this method more concrete.

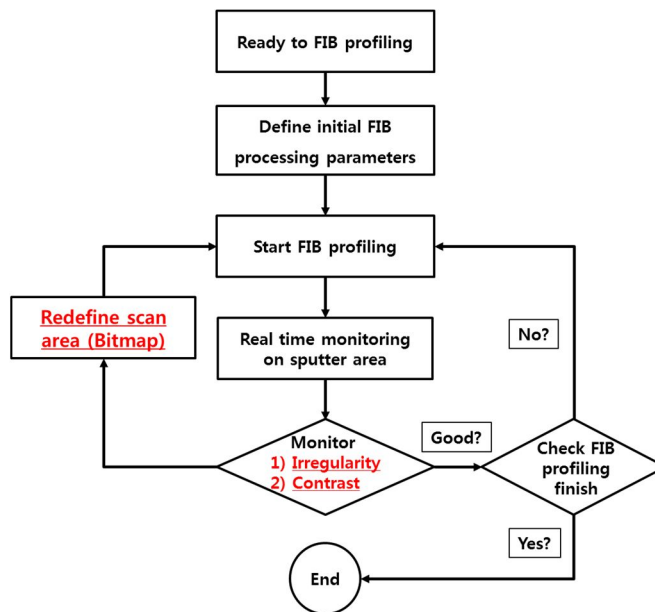


**Figure 5.15** Algorithm for selective FIB profiling

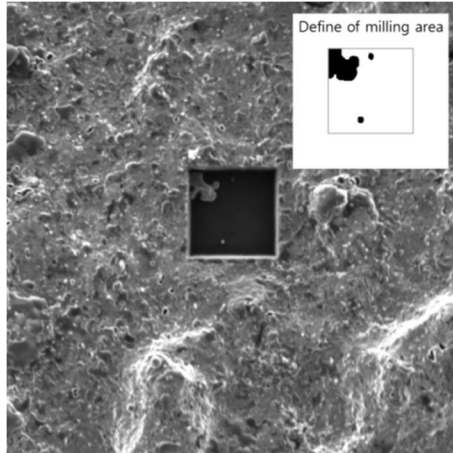


**Figure 5.16** Redefinition of FIB processing area for the selective FIB profiling

### **5.5.2 Selective FIB profiling on multilayer structures**

Basically, the selective FIB profiling was tried to attempt to create the flat surface in Sn/Si double layer system. For this experiment, the simple 2D pocket was profiled only Sn layer by minimizing the damage onto the Si layer. Based on the algorithm of Figure 5.15, the simple 2D pocket was fabricated in Figure 5.17. This displays the procedures of selective FIB profiling technique. Total twelve steps were applied to make the substrate flat by removing the Sn layer only. Before proceeding after steps, new material removal region was redefined by the contrast difference mechanism.

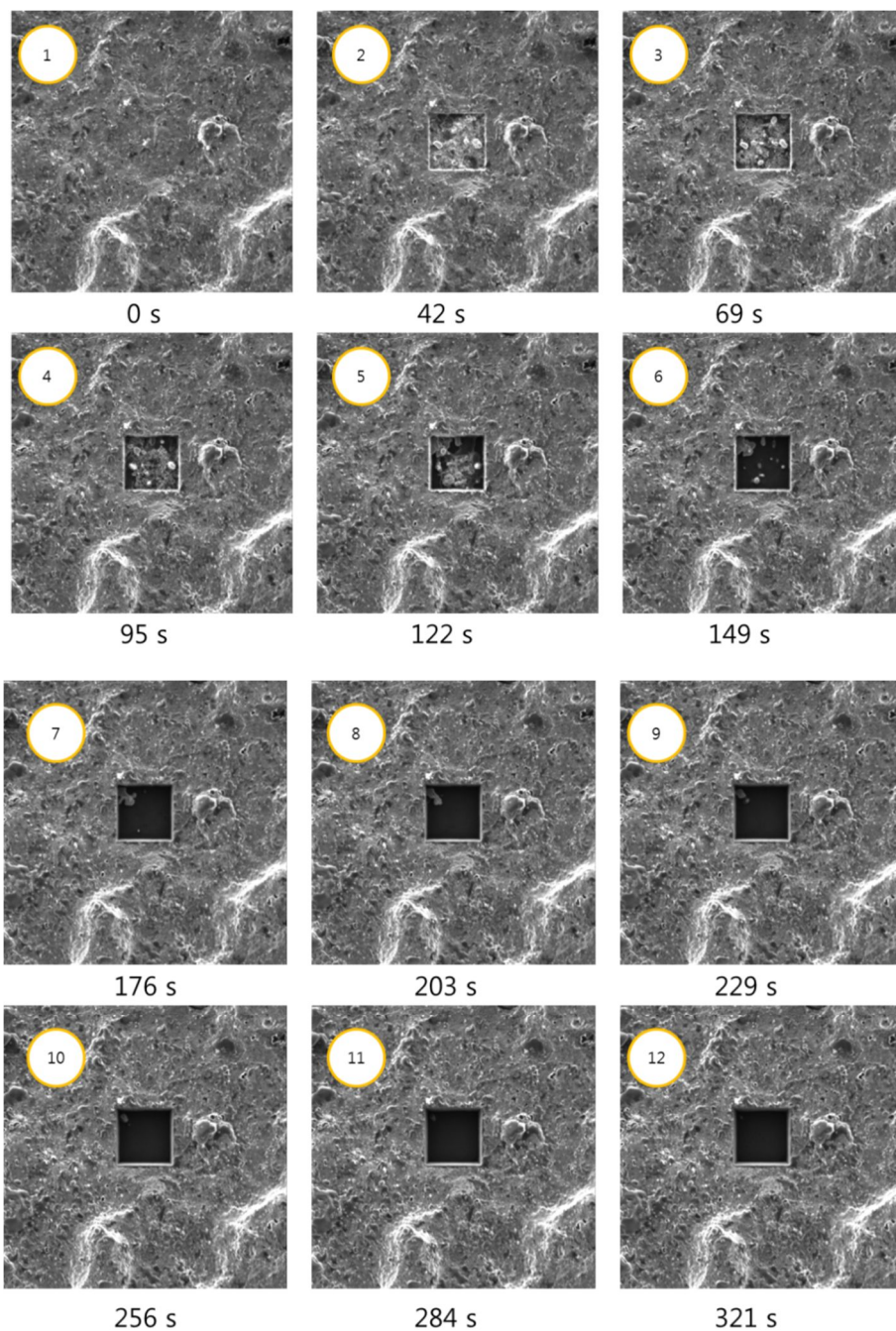


**Figure 5.17** Procedures for the selective FIB profiling on the irregular Sn surface

To this end, the parallel metallic electrodes were fabricated on dielectric film, as shown in Figure 5.18. In order to create two parallel electrodes of Sn on  $\text{Al}_2\text{O}_3$  insulation layer, the selective profiling method was applied. As seen in this figure, two electrodes of Sn on  $\text{Al}_2\text{O}_3$  were well constructed with minimized damages of  $\text{Al}_2\text{O}_3$ .

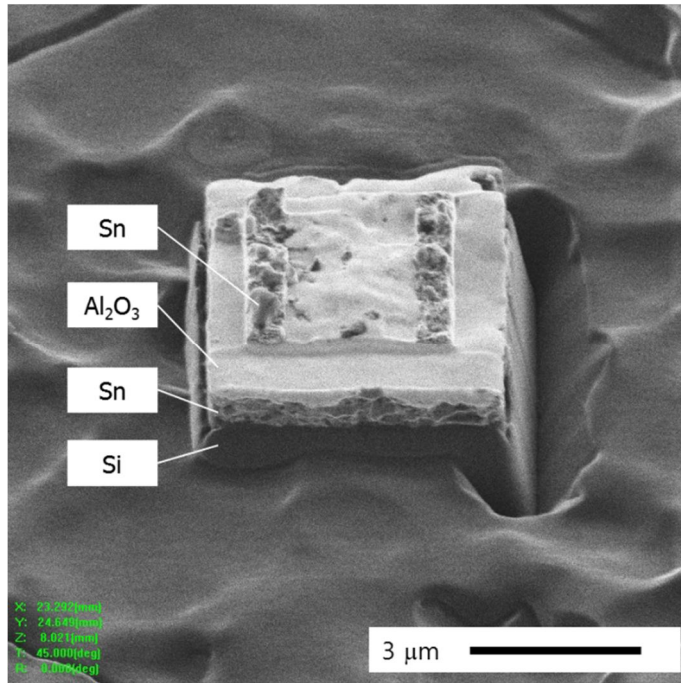


**Figure 5.18** Fabrication of metallic electrodes (Sn) on dielectric layer ( $\text{Al}_2\text{O}_3$ ) using selective FIB profiling technique

## 5.6 Hybrid nanofabrication via repeated procedure

The repeatability of deposition and profile cutting was confirmed through experiments. First, an Sn layer was deposited on Si wafer using NPDS, and then a simple pocket was etched using FIB. The first Sn layer was separated by the pocket. Second, an  $\text{Al}_2\text{O}_3$  layer was deposited, and the pocket was filled with  $\text{Al}_2\text{O}_3$ . This ceramic-filled pocket can act as an insulator. Finally, a Sn layer was formed. The result was evaluated using a cross-section

fabricated by FIB; Figure 5.19 shows a cross-section image. The different conductivity of each layer clearly revealed the layers using FIB scanning. The etched pocket was filled with an  $\text{Al}_2\text{O}_3$  layer, and the step coverage of NPDS was confirmed.

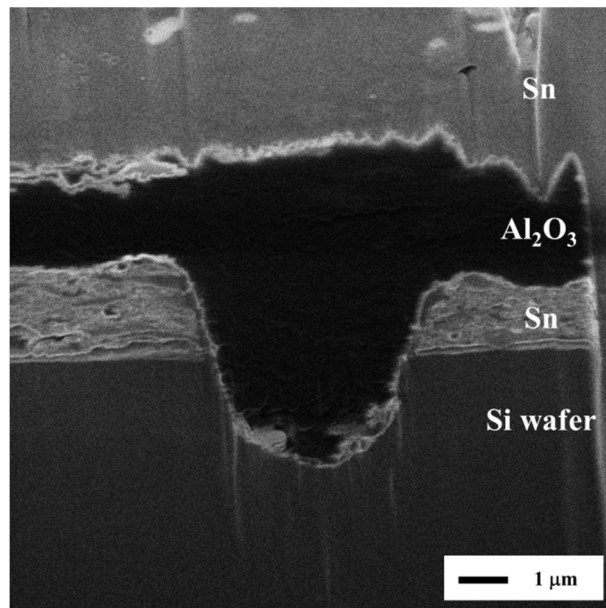


**Figure 5.19** Fabricated Sn/ $\text{Al}_2\text{O}_3$ /Sn/Si wafer structure with an  $\text{Al}_2\text{O}_3$  pocket.

# 6 Interface & Mechanism

## 6.1 Overview

In this chapter, interfaces between films and substrates were investigated in order to observe the adhesion states and adhesion/bonding mechanisms in NPDS. FIB cross-section technique and HR-TEM analysis were introduced for the characterization of interface and mechanism. After cross-sectioning of films by FIB, the SIM was also used to observe the rough microstructure. This SIM is very attractive to observe the microstructure of metallic materials because the ion channeling phenomenon by SIM reflects the crystalline structure of materials by showing the grains, particularly in metals [55]. For the TEM sample preparation of metal and ceramic films, the FIB *lift-off* technique was utilized. Here, all three films of Sn, TiO<sub>2</sub> and Al<sub>2</sub>O<sub>3</sub> on flat and nanostructured substrates were investigated for the verification of interface and bonding mechanism.

## 6.2 Interface and mechanism of metallic particle deposition

Metallic particle deformation had been investigated by many cold spray researches [132-135]. In these publications, the most metallic particles were adhered onto the substrates by the plastic deformation and jetting. Here the interface and mechanism of Sn particle on flat and nanostructured substrates were observed by the FIB cross-section technique, SIM and TEM analyses. The virgin Sn particle had been shown in Figure 3.3.

### 6.2.1 Interface between metallic (Sn) film and substrate

Interfaces between Sn film and silicon (100) substrate were presented in Figure 6.1 and 6.2. Each figure represented the Sn films on and inside the nanostructured surfaces, respectively. As shown in Figure 6.1, Sn particles were deposited on the surface with the good surface adhesion integrity without any empty spaces (Figure 6.1(b)). In this figure nano-sized grains and nanoparticles are clearly visible. In case of nano-sized grains they were formed by at least 3 mechanisms: (1) particle-to-substrate, (b) particle-to-particle, and (b) grain boundary sliding inside particles by the successive particle impact on the substrate with high pressure and temperature. In case of nanoparticles they existed on and below the substrate. In case of nanoparticles formed below the substrate surface were the implanted gallium induced by the nucleation, growth, and so on [136]. Originally, there were no any nanoparticles inside the Sn particle (Figure 3.3).

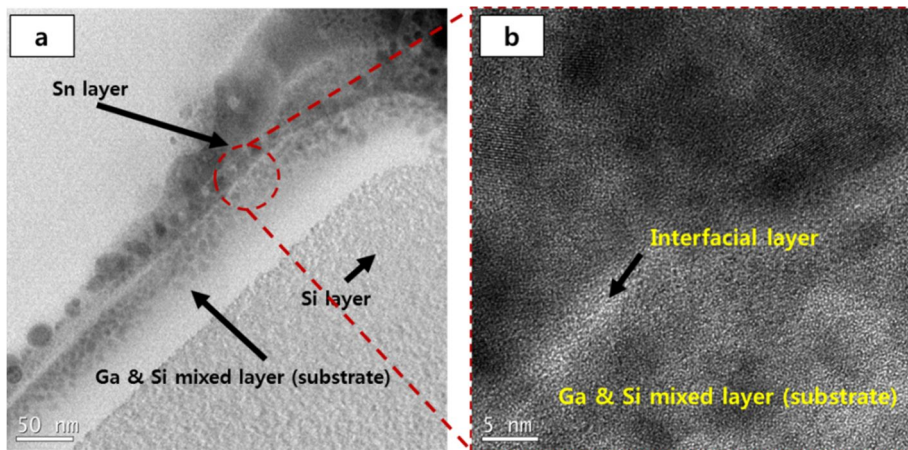


**Figure 6.1** Interface of Sn film on substrate

In case of Figure 6.2, it contains more interesting information of Sn metallic particle deposition by NPDS. It is very useful to see the Sn deposit through depth direction (two dotted arrows) because fewer particles were getting involved to this direction. Along the depth direction inside the

nanostructured substrate the number of particle-to-particle interactions was diminished because no more particles that were being flown could not be inserted inside the nanostructured substrate. Thus, it can indicate that the evolution of film was progressed by the sequences from Figure 6.2(c) to Figure 6.2(a). In Figure 6.2(b-c), the nano-sized grains were mostly formed by the grain boundary sliding generated by the adiabatic plastic deformation influenced with the help of the dislocation defects shown in Figure. 3.3, and also there existed small amount of nanoparticle near the nano-grains. This can explain how the nanoparticle forms in the Sn film. Accordingly, the large amount of nanoparticles was formed in Figure 6.2(a) by the successive particle-to-particle interaction. Most of nanoparticles in Figure 6.2(a) were found not only near the grain boundaries but also in the grains in contrast to Figure 6.2(b). There nanoparticles might be formed by the severe grain boundary sliding inside the particle with the abrupt temperature increment by the successive fracture.

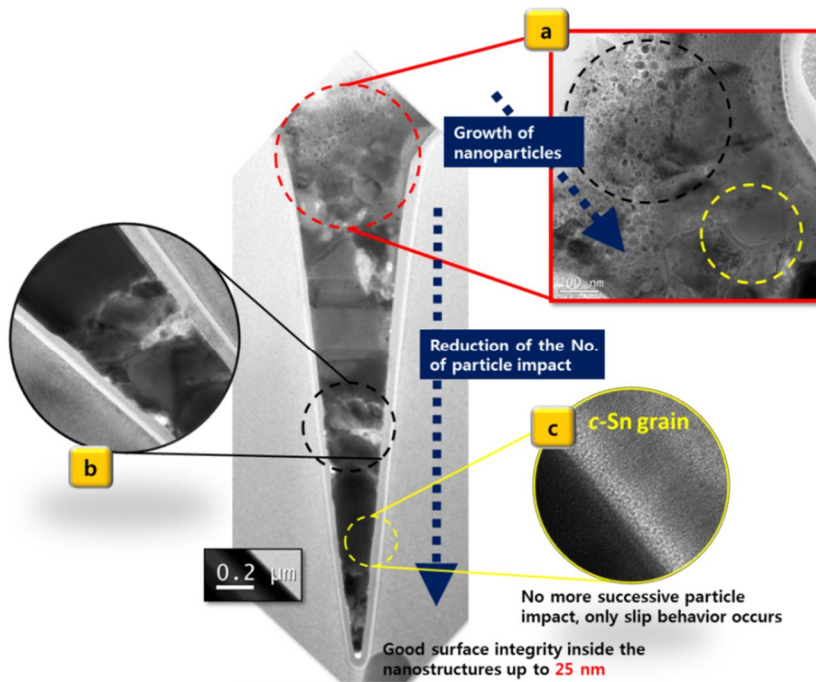


**Figure 6.2** Interface of Sn film inside the nanostructured substrate

### 6.2.2 Evolution mechanism of metallic film of Sn

In order to verify the bonding mechanism by the evolution of Sn particle in NPDS, the experimental model was suggested with three assumptions written in below;

**Assumption 1:** The film has the Gaussian profile

**Assumption 2:** The number of particle-to-particle interaction is different to the Gaussian profile from the center to the tail of it

**Assumption 3:** Metallic particle deforms by the plastic deformation by the impact

The experimental model was presented in Figure 6.3 which could express the assumption 1 and 2. The Gaussian shaped film means that the more particles impact at the center of film. Thus, more particles involve with deposition in the sequence of  $A > B > C$  in Figure 6.3.

For the assumption 3, the screening experiment was performed by observing the cross-section of particle before and after deposition on soft (PDMS) substrate, as shown in Figure 6.4. Figure 6.4(a) and (b) were the cross-sections of two Sn particles: one is 12  $\mu\text{m}$  and another is 2  $\mu\text{m}$  before deposition. As it was clear from two figures, there were no grains detected with the help of SIM. This was the same results in Figure 3.3 that was taken by the HR-TEM of Sn. However, there were several grains in Figure 6.4(c) and (d), which showed the small plastic deformation of metallic particles on soft substrate before the creation of film. It proved that the successive plastic deformation inside the particle by the particle deformation mechanism above get involved with the forming of Sn film.

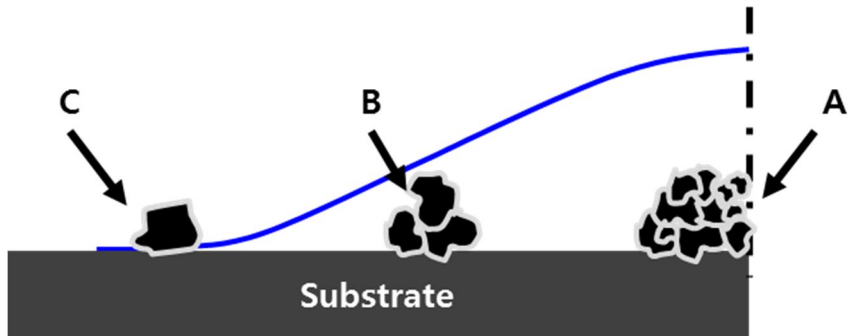


**Figure 6.3** The Gaussian shaped NPDS deposition

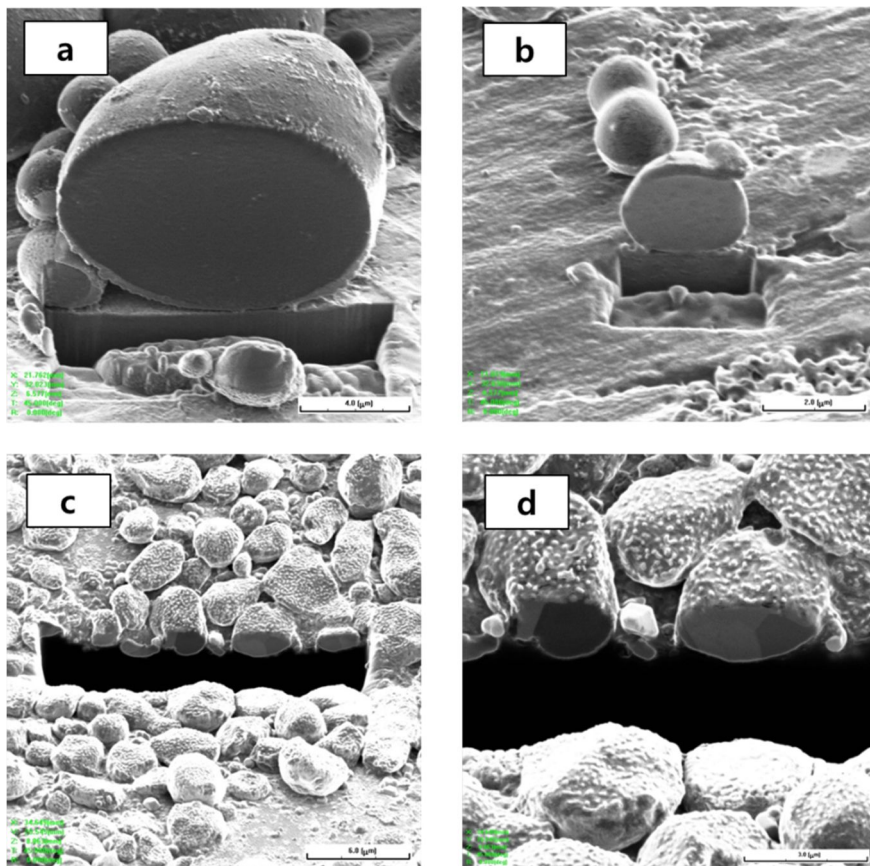


**Figure 6.4** Sn particle deposition: (a-b): before particle deposition on aluminum substrate and (c-d): after particle deposition on soft PDMS substrate

From each regions of A-C in Figure 6.3, the thin lamellas were taken by the FIB technique for both SIM and TEM, as shown in Figure 6.4. In Figure 6.5a<sub>1</sub>-c<sub>1</sub> of SIM, it can clearly show the film structure inside and between particles. By severing successive impaction of particles the microstructures inside the Sn film were much more complicated. The complexity was increased from the center (A) of film to the tail (C) of it because the more plastic deformation took place by experiencing more grain boundary sliding by the fracture as a result of particle impact. In Figure 6.5a<sub>2</sub>-c<sub>2</sub> of TEM, it was more complicated than Figure 6.5a<sub>1</sub>-c<sub>1</sub> of SIM. Through Figure 6.5a<sub>2</sub> it was found out that the nano-sized grains were easily generated by the only particle impaction onto the substrate. Furthermore, it can be inferred that the large amount of dislocational slip by the particle impaction took place.

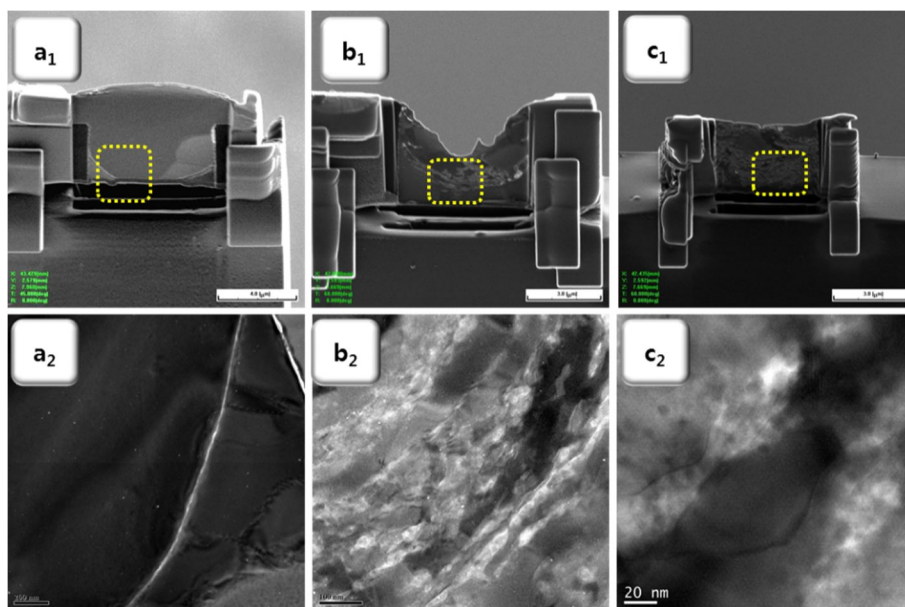


**Figure 6.5** The Sn thin lamella taken by FIB lift-off technique from the regions of A-C in Figure 6.3: (a) region A, (b) region B, and (c) region C in Figure 6.3. The subscriptions of 1 and 2 represent the SIM and TEM images, respectively.

In case of Figure 6.5c<sub>2</sub>, the many particle impacted case, numerous nanoparticles inside the film were found out. In order to find out the mechanism of nanoparticle generation, *in situ* heating was performed in TEM as shown in Figure 6.6 because the formation of nanoparticles were assumed that they were generated by the abrupt temperature increment. Through *in situ* TEM observation the nanoparticles were not formed inside the Sn film at the temperature of 350 °C, they were started to form around 400 °C, as shown in Figure 6.6(b). When the temperature was over 400 °C by reaching to 500 °C, the initially formed nanoparticles were grown as shown in Figure 6.6(c). It directly indicated that the increment of temperature brought about the formation of nanoparticles as it was assumed before. In summary, the evolution mechanism of Sn film deposition by NPDS can be explained from Figure 6.7.

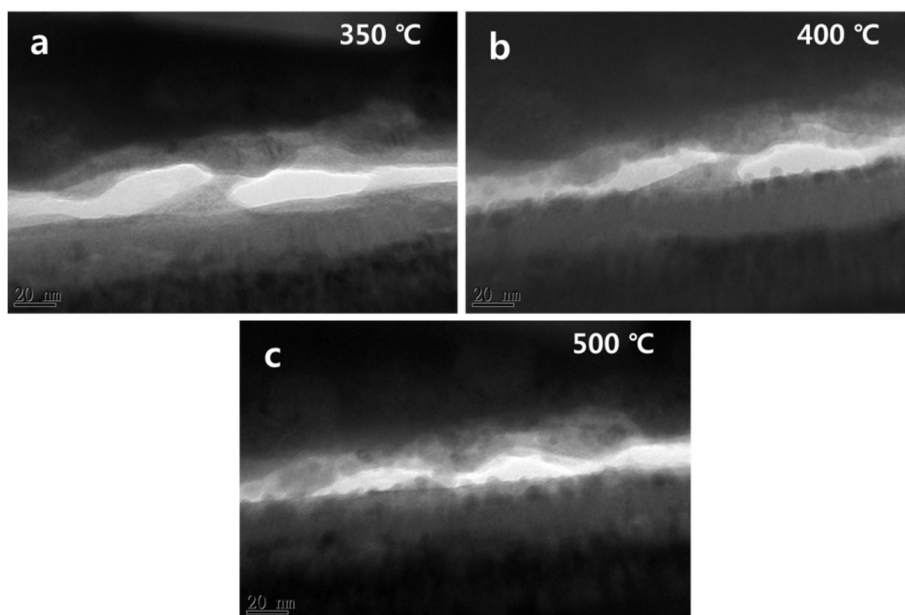


**Figure 6.6** Observation on the formation and the growth of nanoparticles in Sn films with *in situ* heating in TEM: (a) 350 °C, (b) 400 °C and (c) 500 °C.

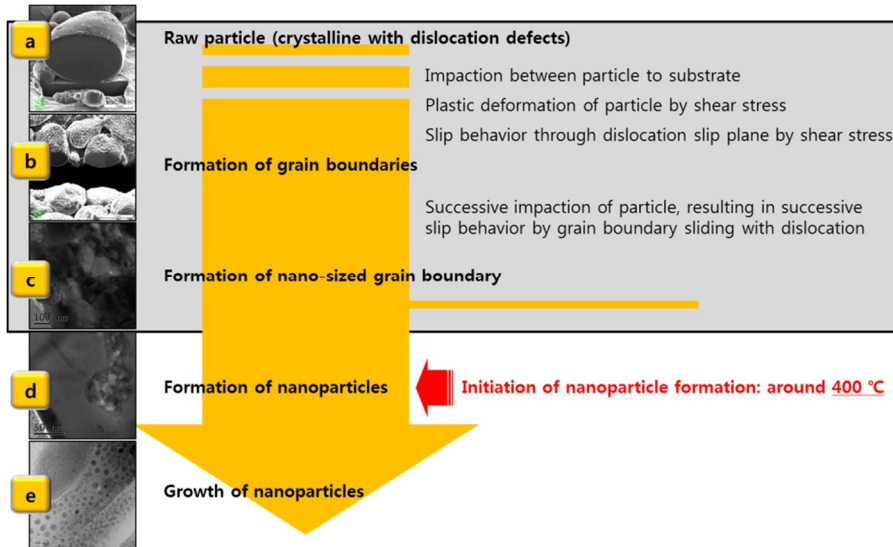


**Figure 6.7** Evolution mechanism of Sn thin film by NPDS

### 6.3 Interface and mechanism of ceramic particle deposition

The deposition mechanism of ceramic particles is known as fragmentation when they contact with substrate with high velocity [65]. This fragmentation for ceramic particle deposition was usually dealt with the aerosol deposition technology. However, the bonding mechanism had not been yet fully understood although the experimental and numerical works were implemented [137, 138]. In recent, the improvement for ceramic particle deposition mechanism for  $\text{Al}_2\text{O}_3$  was achieved through the numerical analysis with the accordance of experimental result in [65]. Here, the interface and bonding mechanism were investigated by taking TEM images of ceramic thin films of  $\text{TiO}_2$  and  $\text{Al}_2\text{O}_3$  on the substrate and inside the nanostructured substrate.

#### 6.3.1 Interface and mechanism of $\text{TiO}_2$ film

Here the FIB cross-section technique and HR-TEM analysis were also improvised to investigate the mechanism of ceramic particle,  $\text{TiO}_2$ , deposition. The interface is shown in Figure 6.8. Through HR-TEM analysis shown in

Figure 6.8, TiO<sub>2</sub> films were well bonded to the substrate and between particle and substrate there existed the amorphous layer by binding each other. This should be developed by the abrupt temperature increase when depositing nanoparticles of TiO<sub>2</sub>. This abrupt temperature increment was took place around the aggregated particle boundaries. Inside these boundaries, TiO<sub>2</sub> nanoparticles were existed as nanocrystalline materials.

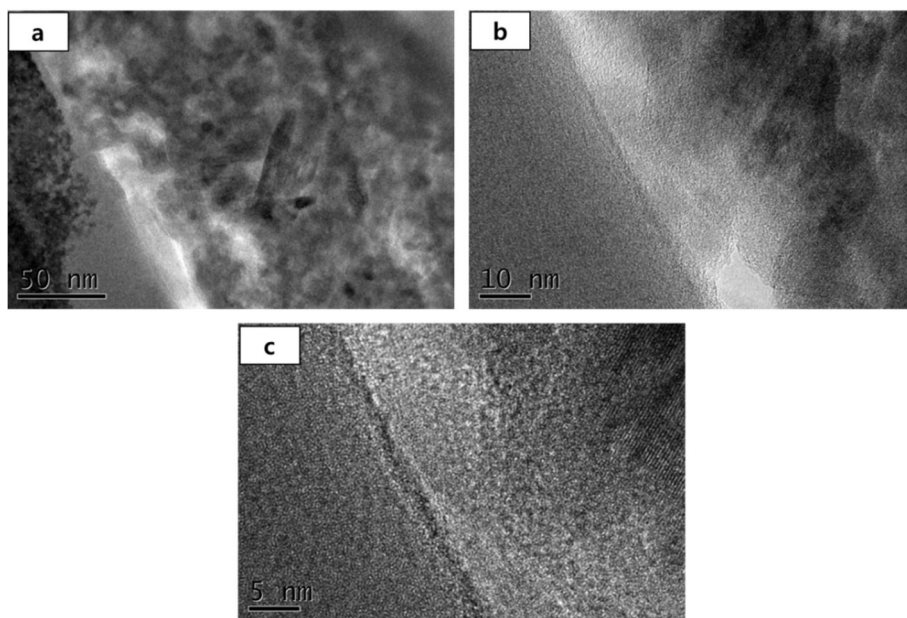


**Figure 6.8** HR-TEM images of nanoporous TiO<sub>2</sub> thin film: (a) interface between film and substrate, (b) amorphization of TiO<sub>2</sub> and (c) nanocrystalline TiO<sub>2</sub> particles

Unlike the TiO<sub>2</sub> film on the flat substrate, the TiO<sub>2</sub> film inside the nanostructured substrate was not densely packed as a solid film, as shown in Figure 6.9. It might be caused by the weak air flow pressure to pack TiO<sub>2</sub> nanoparticles inside the nanostructured substrate. However, the air flow pressure was limited from the plastic particle container, which is restricted of pressure of 0.3 MPa, in the aerosol generator. Hopefully, if the particle

container is placed to robust material and structure which can exert high pressure, nanoparticles like  $\text{TiO}_2$  can be densely packed inside nanostructured substrates. Evidently, the sparsely positioned agglomerated nanoparticles, shown in Figure 6.9(b) and (c), can show the formation of amorphous layer networks between agglomerated particles. From this evidences, it can be stated that the friction induced drastic temperature increment forms the amorphous layers at boundaries of individual nanoparticles and agglomerated particles of  $\text{TiO}_2$  when particles are being flown through air tubes and nozzle.

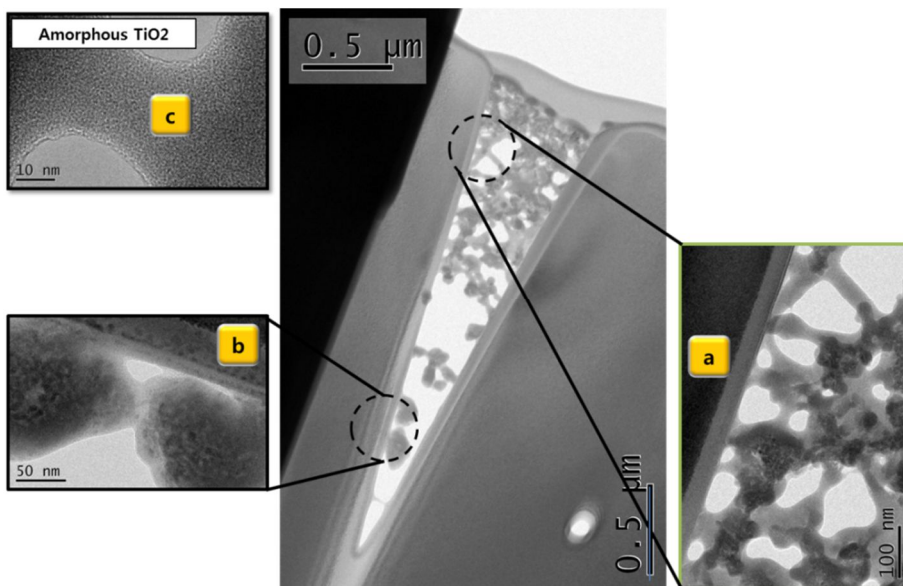
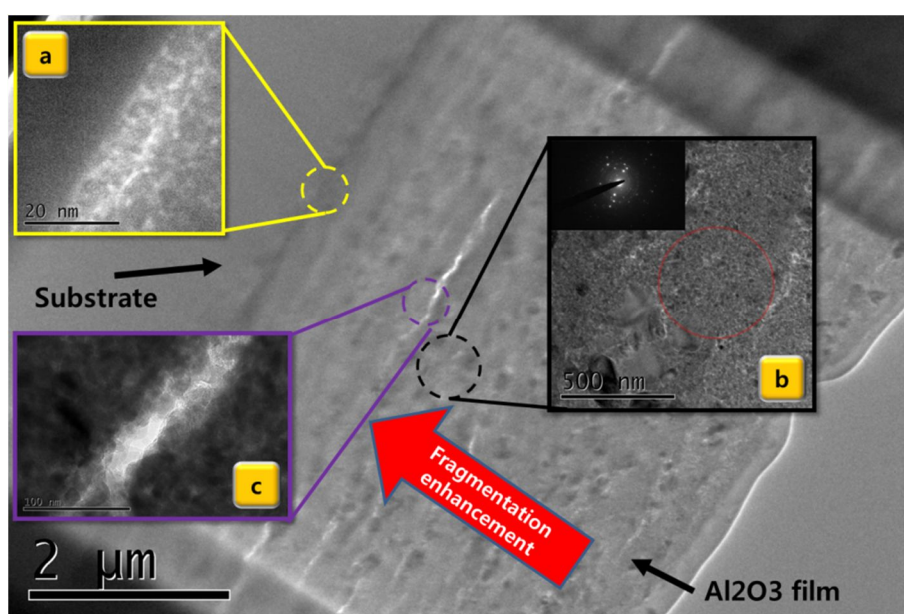


**Figure 6.9** HR-TEM images of nanoporous  $\text{TiO}_2$  structure inside the nanostructured substrate: (a) amorphous necking networks between aggregated particles, (b) adhesion interface: particle-to-particle and particle-to-substrate and (c) magnified view of amorphous necking network

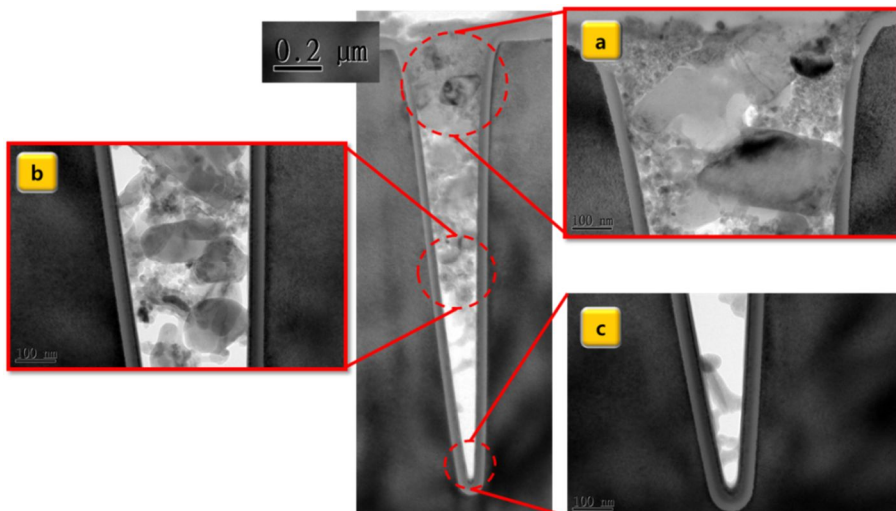
### 6.3.2 Interface and mechanism of $\text{Al}_2\text{O}_3$ film

Figure 6.10 shows the results of  $\text{Al}_2\text{O}_3$  film on the flat substrate. Overall, the  $\text{Al}_2\text{O}_3$  nanoparticle having two dimensional sizes (around 20 nm and 200

nm) were deposited well on the substrate. It was noticeable to focus on the Figure 6.10(a) where the  $\text{Al}_2\text{O}_3$  nanoparticles bonded with substrate together. The sizes of nanoparticle near the substrate surface were much smaller than the raw  $\text{Al}_2\text{O}_3$  nanoparticles of 20 nm. This nanoparticles' size was around 5 nm or less. It can state that the fragmentation of original nanoparticles was occurred when impacting with the substrate. This results is good agreement of [65]. Figure 6.10(b) explains that  $\text{Al}_2\text{O}_3$  kept their crystalline structure after being deposited. Figure 6.10(c) explains that  $\text{Al}_2\text{O}_3$  contains small porous region. Only the small fraction of porosity was observed in Figure 6.10(c).



**Figure 6.10** HR-TEM images of  $\text{Al}_2\text{O}_3$  thin film: (a) interface between film and substrate, (b) interface between particles in the middle of film and (c) low densification region with small porosity



**Figure 6.11** HR-TEM images of nanoporous  $\text{Al}_2\text{O}_3$  structure inside the nanostructured substrate: (a) near the top surface region, (b) near the middle surface region and (c) near the down surface region

# 7 Functional nanostructures

## 7.1 Overview

The multimaterial availability of NPDS can take huge benefits by adopting various materials as not only films and but also substrates. In this chapter one of smart materials, a shape memory alloy, was hired as a substrate to create the functional nanostructures as an application. Nitinol (TiNi) was accommodated as a shape memory alloy. The shape memory effect had been acknowledged that it could maintain its shape memory characteristic around 100 nm [139], and the ever-existing smallest shape recovery was demonstrated in [140] and [141] with 200 nm and 300 nm (bilayer: 140 nm TiNiCu and 160 nm of Pt), respectively. Here, TiNi were memorized to demonstrate the one-way and two-way motions. The nanoscale beams were fabricated by FIB using only TiNi itself to check the feasibility of nanoscale functional manipulation, as one of the processes in nanoscale 3D printing process. And the capability of NPDS deposition on smart material was tested.

## 7.2 Shape memory ally of TiNi

A shape memory alloy is the smart and the functional material which can memory its geometry. For instance, after a piece of SMA had been deformed from its original geometry, it turns back to original geometry by itself during heating (shape memory effect) [142, 143]. These extraordinary properties are based on a temperature-dependent martensitic phase transformation from a low-symmetry (martensite) to a highly symmetric crystallographic structure (austenite) upon heating [142, 143]. Shape memory effects have been found in

many materials, such as metals, ceramics and polymers. Among all these materials, TiNi based alloys have been extensively studied and found many commercial and academic applications [142, 144-146].

Here the NPDS was introduced to deposit particles on TiNi alloy as a substrate. The microstructure of TiNi is shown in Figure 4.8. It had an operating temperature of 90 °C.

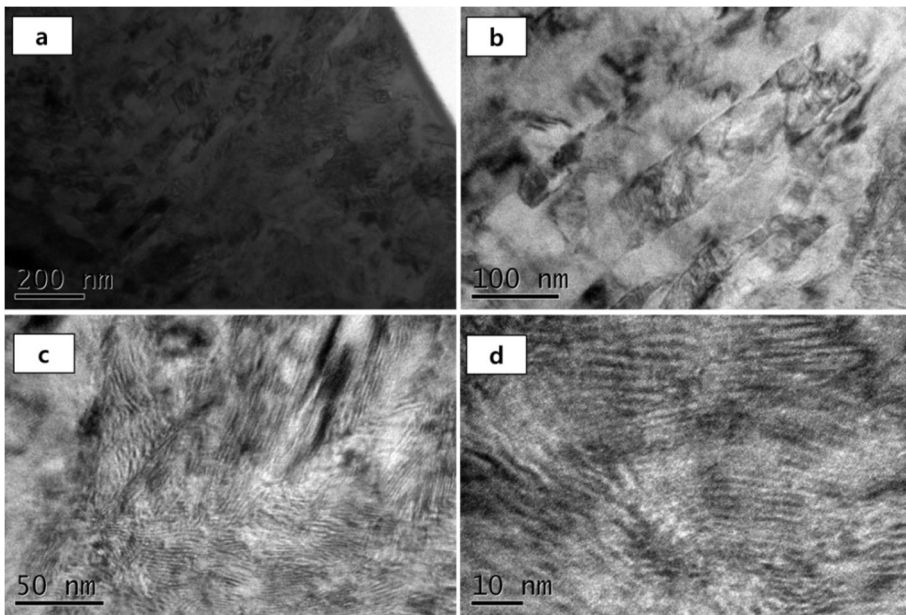


**Figure 7.1** HR-TEM images of shape memory alloy of TiNi

### 7.3 Sample preparation and instrumentation

#### 7.3.1 Memorizing the geometry of NiTi

Here, two types of TiNi were prepared to memorize their geometries for one-way and two-way actuations. The thin foil of TiNi having a thickness of 100  $\mu\text{m}$  was memorized by curling up this foil with 6.5 mm shaft, resulting in the prestrain of 3.1 %. For one-way memorization, the TiNi was heated with

its deformed geometry at the temperature of 450 °C. For two-way memorization, the heating and cooling at the temperature of 150 °C and 25 °C was repeated over 10 times.

### 7.3.2 Fabrication of nanoscale beam of TiNi

In order to fabricate functional nanostructures, FIB itself and FIB/NPDS were utilized. Figure 7.2 represents the nanoscale beams. In case of Figure 7.2(c), the Sn/TiNi double layer structure was formed using NPDS. It was found out that NPDS enable metallic particle to deposit on the TiNi. Each nanoscale TiNi beams were fabricated on the TEM grids. They were also fixed at both ends using a diamond like amorphous carbon.

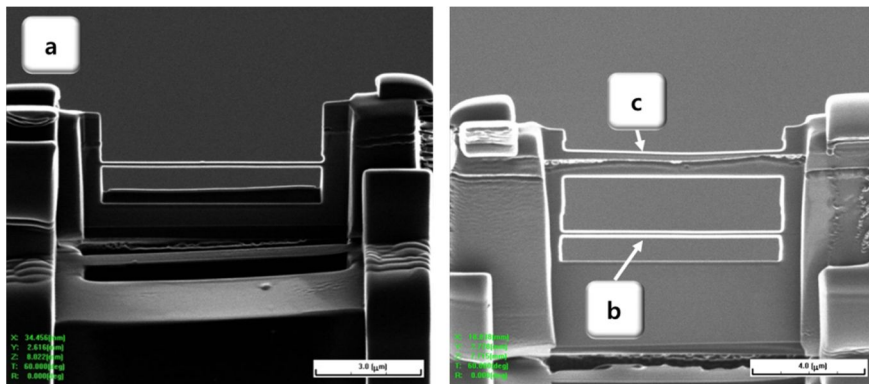


**Figure 7.2** Fabrication of nanoscale TiNi beam using one-way TiNi (a), two-way TiNi (b) and Sn on two-way TiNi (c).

### 7.3.3 Instrumentation for nanomanipulation

The source of the actuation of NiTi nanostructure is the microstructural transformation from martensite to austenite. This transformation has to be driven by temperature variance. This temperature increment should be engaged to the nanostructure. In order to observe the actuation of NiTi

nanostructure, it was placed in *in situ* TEM for both heating and cooling. Figure 7.3(a) and (b) represents the *in situ* TEM used and the loaded nanoscale TiNi beam on the *in situ* heating sample holder, respectively.

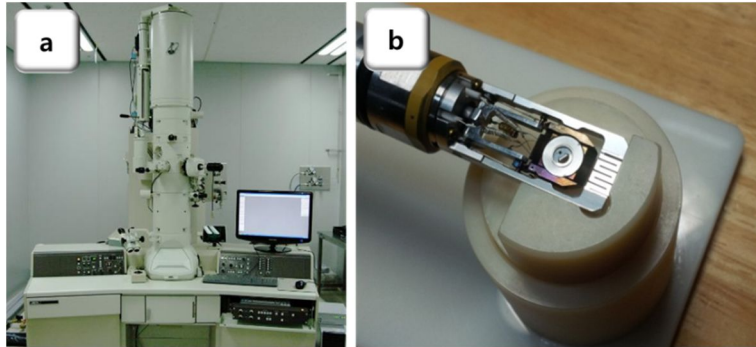


**Figure 7.3** *in situ* TEM (JEM-3011 (HR), Jeol Ltd, Japan) which can heat up the sample up to 800 °C and can observe in real time with CCD camera (SC 1000, Gatan Inc.) and its heating sample holder; the NiTi sample was loaded in the sample holder

#### **7.4 Manipulation of nanoscale TiNi beam**

Nanoscale TiNi beam, shown in Figure 7.2, was inserted into *in situ* TEM. The resistive heat was transferred into the beam on the TEM grid. First, the one-way actuation was implemented as shown in Figure 7.4. When the temperature reached around 90 °C, the nanoscale beam started to deform into downward, and then the temperature was increased up to 100 °C (Figure 7.4(b)) which is bigger than the operating temperature for shape memory the maximum deformation was around 525 nm. In order to observe the temperature effect over the operating temperature, the heat was increased up to 150 °C and 200 °C, as shown in Figure 7.4 (c-d), respectively. The maximum displacements which are measured from Figure 7.4(c-d) are 497.934 nm and 550.903 nm, respectively. These values are almost the same

as maximum displacement value at 100 °C. It was noticeable that the microstructural change from martensite and austenite was observed from Figure 7.4(a) to Figure 7.4(b) obviously.

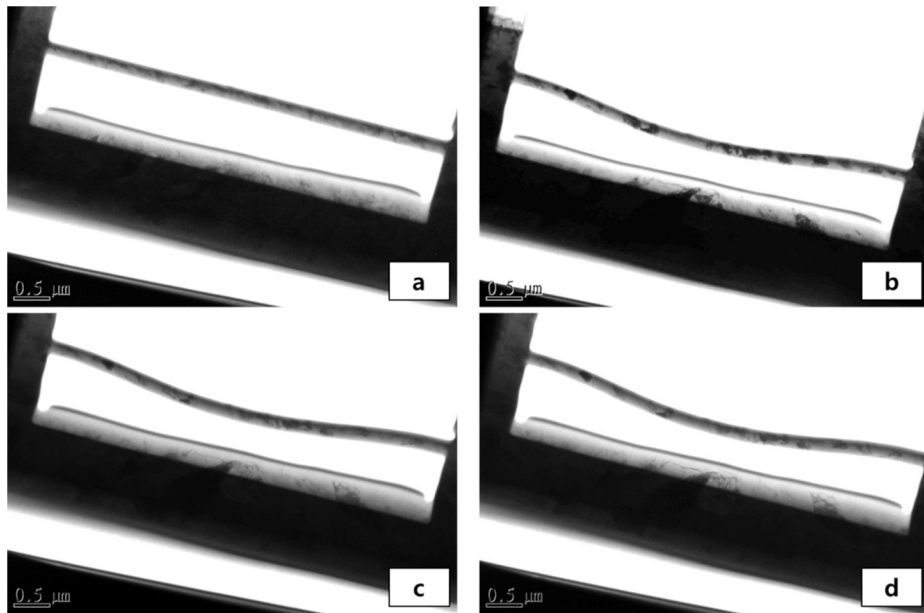


**Figure 7.4** Manipulation of one-way nanoscale TiNi beam: (a) 25 °C, (b) 100°C, (c) 150 °C and (d) 200 °C

The motion of two-way nanoscale TiNi beam was shown in Figure 7.5. In case of this beam, its actuation direction was backward against the one-way motion because its TiNi was taken at the bottom side of thin foil. Namely, it has negative prestrain value of -3.1 % (Figure 7.5(a)). The actuation geometry itself from two-way TiNi was almost same as the actuation geometry from one-way TiNi. However, the operation temperature was much higher than its original operation temperature of 100 °C. It was originated from the changes in chemical composition and stresses because the gallium implantation was inevitable when fabricating nanoscale TiNi beam using FIB [139, 141]. Also, the implantation of gallium was scattered in random. Therefore, it is

noticeable that the probe current of FIB should be selected carefully for the reduction of the microstructural defects and changes, and internal stresses. This extraordinarily increased operation temperature shown in Figure 7.5(b) might be also affect the decrement of deformation compared to the Figure 7.4.

In case of Sn/TiNi bilayer structure shown in Figure 7.2(c), its thermally-driven manipulation was not observed in the *in situ* TEM. It might be due to the defect generation of TiNi by the impaction of high velocity particle. However, it is very obvious that NPDS can deposit metallic particle, especially Sn, on TiNi, one of the smart materials.

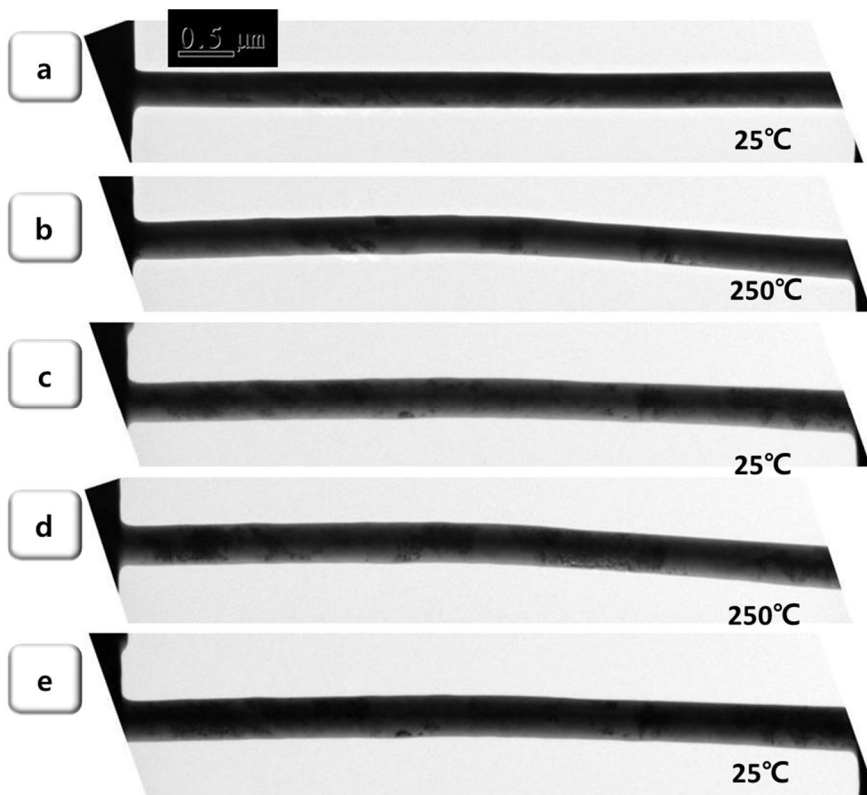


**Figure 7.5** Manipulation of two-way nanoscale TiNi beam: (a) 25 °C, (b) 250°C, (c) 25 °C, (d) 250 °C and (e) 25 °C

## 7.5 Model for NiTi actuation

To demonstrate the manipulation of TiNi nanoscale beams, including one-way and two-way actuators, the manipulation principle was suggested as shown in Figure 7.6. On the basis of this principle, the structural model of beam-column pinned at both ends was assumed. The governing equation of buckling model was given as Equation 7.1 with its general solution of Equation 7.2.

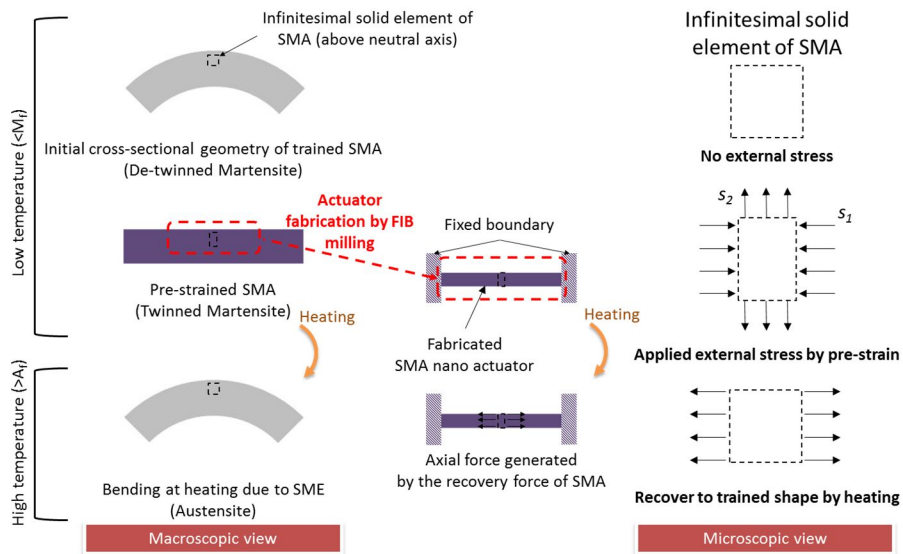


**Figure 7.6** Manipulation principle of nanoscale TiNi beam

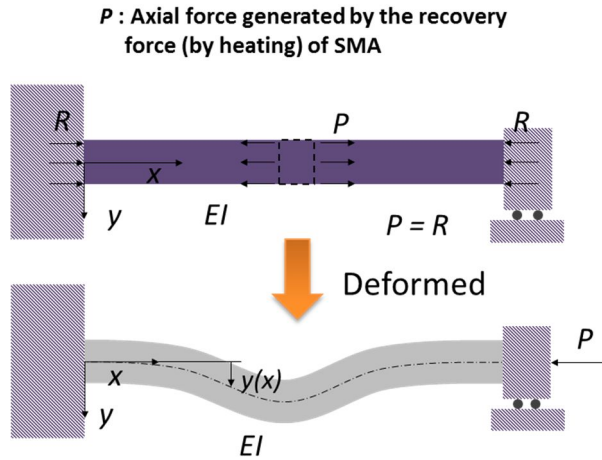


**Figure 7.7** Structural model and geometrical configuration of nanoscale TiNi beam

$$\frac{d^4 y}{dx^4} + \frac{P}{EI} \cdot \frac{d^2 y}{dx^2} = 0 \quad \text{Equation 7.1}$$

$$y = C_1 \cdot \sin\left(\sqrt{\frac{P}{EI}} \cdot x\right) + C_2 \cdot \cos\left(\sqrt{\frac{P}{EI}} \cdot x\right) + C_3 \cdot x + C_4 \quad \text{Equation 7.2}$$

The boundary conditions of the nanoscale beam which is pin-connected at both ends requires that

$$y(0) = 0, \frac{dw(0)}{dx} = 0 \text{ and } y(L) = 0, \frac{dw(L)}{dx} = 0,$$

Apply to Equation 7.2, the foregoing conditions lead to the following equations:

$$y(0) = C_2 + C_4 = 0$$

$$y(L) = C_1 \cdot \sin\left(\sqrt{\frac{P}{E \cdot I}} \cdot L\right) + C_2 \cdot \cos\left(\sqrt{\frac{P}{E \cdot I}} \cdot L\right) + C_3 \cdot L + C_4 = 0$$

$$y'(0) = C_1 \cdot \sqrt{\frac{P}{E \cdot I}} + C_3 = 0$$

$$y'(L) = C_1 \cdot \sqrt{\frac{P}{E \cdot I}} \cdot \cos\left(\sqrt{\frac{P}{E \cdot I}} \cdot L\right) - C_2 \cdot \sqrt{\frac{P}{E \cdot I}} \cdot \sin\left(\sqrt{\frac{P}{E \cdot I}} \cdot L\right) + C_3 = 0$$

By solving Eigenvalue problem, the first mode condition is

$$\sqrt{\frac{P}{E \cdot I}} \cdot L = 2 \cdot \pi \quad \text{Equation 7.3}$$

By the first mode condition,

$$y = -C_2 \cdot \left(1 - \cos\left(\frac{2 \cdot \pi \cdot x}{L}\right)\right) \quad \text{Equation 7.4}$$

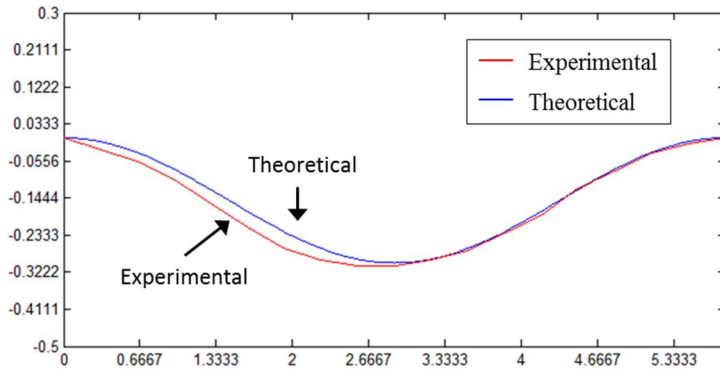
Using the maximum deflection conditions from experiments, equations were given in both one-way and two-way as following:

$$y_{one-way} = -0.15 \cdot (1 - \cos(1.087 \cdot x)) (\mu m) \quad \text{Equation 7.5}$$

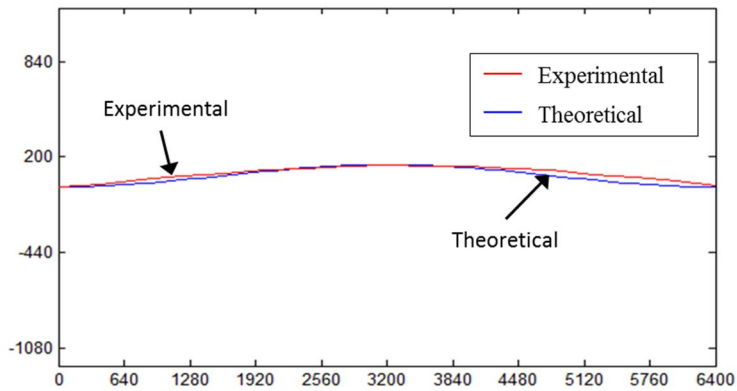
$$y_{two-way} = -74.78 \cdot (1 - \cos(0.00098 \cdot x)) (\mu m) \quad \text{Equation 7.6}$$

Figure 7.7-8 are the simulation results with the comparison of experimental and theoretical results. As shown in these figures, there were only small errors between theoretical and experimental deflection

value. It proved that the bucking model at pinned at both end was appropriate to model the nanoscale TiNi beam.



**Figure 7.8** Comparison of experimental and theoretical results of one-way nanoscale TiNi beam



**Figure 7.9** Comparison of experimental and theoretical results of two-way nanoscale TiNi beam

## 8 Conclusions

A novel nanoscale hybrid manufacturing process was developed by integrating the NPDS and FIB. NPDS is an additive process for thin film deposition, and can fabricate metal and ceramic film by spraying nano/micro-sized particles at room temperature. FIB is a subtractive process used for nanoscale etching; it is ultra-precise, yielding less than 100 nm resolution under room-temperature processing conditions. Neither process requires any binder, solution, or post-processing.

Through the analysis of FIB scan style thoroughly, the influences of important two parameters, including dwell time and beam overlap, were investigated. As a result, their effects on characteristics of surface morphology, composition and physicochemical characteristics were analyzed, and the parameter induced by the scan style was analyzed.

In order to overcome the defective structures studied from dwell time and beam overlap, the new ion beam paths were generated by the vector scan code, and it showed the improvement of precision and accuracy. Furthermore, this new ion beam path was applied onto the 3D FIB profiling which can expand the manufacturability restricted from NPDS resolution. In case of NPDS nanostructuring, the minimum thicknesses for metal and ceramic materials were investigated to suggest the resolution of current NPDS.

By combining or repeating both the deposition and the profile cutting, the feasibility of nanostructuring through hybrid process has been create the nanoscale metallic and porous structures for Sn and TiO<sub>2</sub>, respectively. And the nanostructures with multimaterials were well fabricated through the integrated process, and one of these nanostructures was modified by post-processing of FIB, resulting in the electrode fabrication on hybrid process fabricated multilayer structure. Moreover, the repetition of both process

created that multi-layered nanostructures with thickness of 500 nm were made of different materials at room temperature without any binding materials.

Furthermore the interfaces between substrate and film were experimentally observed to see the adhesion state and mechanism of adhesion for metal and ceramic materials, respectively. Through entire sets of HR-TEM analysis, the adhesion status and deposition mechanism were investigated and proved against the existing theory. Additionally, the mechanical and physical phenomena related to mechanics of material adhesion were investigated and give the new mechanism by the ultra-small nanoparticle formation, especially in metal particle deposition.

As an application, the functional nanostructures with shape memory alloy were fabricated through this nanoscale manufacturing process. It showed that feasibility of actuation using NiTi material in the nanoscale regime.

Overall, the nanoscale hybrid manufacturing process has been developed and each process of FIB and NPDS were investigated to combine and apply the functional 3D nanostructures with multimaterials.

It is very meaningful; (1) the terms of 'hybrid' was adopted to build the 3D printing system for 3D nanostructure with multimaterials, (2) the FIB technology applied for conventional mechanical machining process by adopting the ion beam path generation like tool path generation, (3) the particle based deposition technology was applied in the nanotechnology unlike other cold spray or aerosol technology.

# Bibliography

- [1] <http://www.moorelaw.org/>.
- [2] Swanson E. 15 - Moore's Law. In: Jim W, editor. The Art and Science of Analog Circuit Design. Woburn: Newnes; 1998. p. 251-61.
- [3] Commission E. The march of micro- and nano-manufacture. 2009.
- [4] Scholz SG, Griffiths CA, Dimov SS, Brousseau EB, Lalev G, Petkov P. Manufacturing routes for replicating micro and nano surface structures with bio-mimetic applications. CIRP Journal of Manufacturing Science and Technology. 2011;4:347-56.
- [5] Brousseau EB, Dimov SS, Pham DT. Some recent advances in multi-material micro- and nano-manufacturing. Int J Adv Manuf Technol. 2010;47:161-80.
- [6] Ngo HD, Leib J. Wafer Level Packaging Technology for Optical Imaging Sensors. Procedia Chemistry. 2009;1:17-20.
- [7] Fang Z, Chen QY, Zhao CZ. A review of recent progress in lasers on silicon. Optics & Laser Technology. 2013;46:103-10.
- [8] Biswas A, Bayer IS, Biris AS, Wang T, Dervishi E, Faupel F. Advances in top-down and bottom-up surface nanofabrication: Techniques, applications & future prospects. Advances in Colloid and Interface Science. 2012;170:2-27.
- [9] Dimov SS, Matthews CW, Glanfield A, Dorrington P. A roadmapping study in Multi-Material Micro Manufacture. Cardiff University; 2006. p. 1-15.
- [10] [http://creativemachines.cornell.edu/Multi\\_material\\_3D\\_Printing](http://creativemachines.cornell.edu/Multi_material_3D_Printing).
- [11] <http://www.nottingham.ac.uk/>
- [12] <http://cubify.com/cube/>.
- [13] Bergmann C, Lindner M, Zhang W, Koczur K, Kirsten A, Telle R, et al. 3D printing of bone substitute implants using calcium phosphate and bioactive

- glasses. *Journal of the European Ceramic Society*. 2010;30:2563-7.
- [14] S CW, Jeong SY, Kim SG, Ha WS, Chi SC, Ahn SH. Fabrication of a biodegradable drug delivery system with controlled release made of PLGA/5-FU/hydroxyapatite. *Rapid Prototyping Journal*. 2008;14:293-9.
- [15] <http://www.popularmechanics.com/technology/engineering/extreme-machines/advanced-3d-printer-creates-nano-indycar-7358796>.
- [16] Kometani R, Hoshino T, Kanda K, Haruyama Y, Kaito T, Fujita J-i, et al. Three-dimensional high-performance nano-tools fabricated using focused-ion-beam chemical-vapor-deposition. *Nuclear Instruments and Methods in Physics Research Section B: Beam Interactions with Materials and Atoms*. 2005;232:362-6.
- [17] Fischer AC, Belova LM, Rikers YGM, Malm BG, Radamson HH, Kolahdouz M, et al. 3D Free-Form Patterning of Silicon by Ion Implantation, Silicon Deposition, and Selective Silicon Etching. *Advanced Functional Materials*. 2012;22:4004-8.
- [18] Matsui S. Focused-ion-beam deposition for 3-D nanostructure fabrication. *Nuclear Instruments and Methods in Physics Research Section B: Beam Interactions with Materials and Atoms*. 2007;257:758-64.
- [19] Whatmore RW. Nanotechnology: big prospects for small engineering. *Ingenia*. 2001:28-33.
- [20] [www.fei.com/](http://www.fei.com/)
- [21] [www.siint.com/en/](http://www.siint.com/en/)
- [22] Hibi Y, Enomoto Y, Kikuchi K, Shikata N, Ogiso H. Excimer laser assisted chemical machining of SiC ceramic. *Applied Physics Letters*. 1995;66:817-8.
- [23] Miyazawa H, Miyake S, Watanabe S, Murakawa M, Miyazaki T. Laser-assisted thermochemical processing of diamond. *Applied Physics Letters*. 1994;64:387-9.
- [24] Zhang H, Xu J, Wang J. Investigation of a novel hybrid process of laser drilling assisted with jet electrochemical machining. *Optics and Lasers in*

Engineering. 2009;47:1242-9.

[25] Li L, Achara C. Chemical Assisted Laser Machining for The Minimisation of Recast and Heat Affected Zone. CIRP Annals - Manufacturing Technology. 2004;53:175-8.

[26] Zhu D, Zeng YB, Xu ZY, Zhang XY. Precision machining of small holes by the hybrid process of electrochemical removal and grinding. CIRP Annals - Manufacturing Technology. 2011;60:247-50.

[27] Chen S-T, Jiang Z-H, Wu Y-Y, Yang H-Y. Development of a grinding-drilling technique for holing optical grade glass. International Journal of Machine Tools and Manufacture. 2011;51:95-103.

[28] Aspinwall DK, Dewes RC, Burrows JM, Paul MA, Davies BJ. Hybrid High Speed Machining (HSM): System Design and Experimental Results for Grinding/HSM and EDM/HSM. CIRP Annals - Manufacturing Technology. 2001;50:145-8.

[29] Liu HS, Yan BH, Chen CL, Huang FY. Application of micro-EDM combined with high-frequency dither grinding to micro-hole machining. International Journal of Machine Tools and Manufacture. 2006;46:80-7.

[30] Kang B, Woo Kim G, Yang M, Cho S-H, Park J-K. A study on the effect of ultrasonic vibration in nanosecond laser machining. Optics and Lasers in Engineering. 2012;50:1817-22.

[31] Yan BH, Wang AC, Huang CY, Huang FY. Study of precision micro-holes in borosilicate glass using micro EDM combined with micro ultrasonic vibration machining. International Journal of Machine Tools and Manufacture. 2002;42:1105-12.

[32] Hwang Y-L, Kuo C-L, Hwang S-F. Fabrication of a micro-pin array with high density and high hardness by combining mechanical peck-drilling and reverse-EDM. Journal of Materials Processing Technology. 2010;210:1103-30.

[33] [http://microscopy.zeiss.com/microscopy/en\\_de/products.html](http://microscopy.zeiss.com/microscopy/en_de/products.html).

[34] <http://www.sinam.org/>.

[35] Sutanto E, Shigeta K, Kim YK, Graf PG, Hoelzle DJ, Barton KL, et al. A

multimaterial electrohydrodynamic jet (E-jet) printing system. *Journal of Micromechanics and Microengineering*. 2012;22:045008.

[36] Lewis JA. Direct Ink Writing of 3D Functional Materials. *Advanced Functional Materials*. 2006;16:2193-204.

[37] Kim H, Lee H-B-R, Maeng WJ. Applications of atomic layer deposition to nanofabrication and emerging nanodevices. *Thin Solid Films*. 2009;517:2563-80.

[38] [http://en.wikipedia.org/wiki/Atomic\\_layer\\_deposition](http://en.wikipedia.org/wiki/Atomic_layer_deposition).

[39] Ahn SH, Guo LJ. Large-Area Roll-to-Roll and Roll-to-Plate Nanoimprint Lithography: A Step toward High-Throughput Application of Continuous Nanoimprinting. *ACS Nano*. 2009;3:2304-10.

[40] Spinney PS, Collins SD, Smith RL. Solid-Phase Direct Write (SPDW) of Carbon via Scanning Force Microscopy. *Nano Letters*. 2007;7:1512-5.

[41] Ahn SH, Chun DM, Kim CS. Nanoscale hybrid manufacturing process by nano particle deposition system (NPDS) and focused ion beam (FIB). *CIRP Annals - Manufacturing Technology*. 2011;60:583-6.

[42] Chun DM, Kim MH, Lee JC, Ahn SH. TiO<sub>2</sub> coating on metal and polymer substrates by nano-particle deposition system (NPDS). *CIRP Annals - Manufacturing Technology*. 2008;57:551-4.

[43] <http://fab.snu.ac.kr/>.

[44] Doo-Man C, Min-Hyeng K, Jae-Chul L, Sung-Hoon A. A Nano-particle Deposition System for Ceramic and Metal Coating at Room Temperature and Low Vacuum Conditions. *International Journal of Precision Engineering and Manufacturing*. 2008;9:51-3.

[45] Kyubong J, Woojin S, Doo-Man C, Yang-Hee K, Jun-Cheol Y, Min-Saeng K, et al. Nickel Line Patterning Using Silicon Supersonic Micronozzle Integrated with a Nanoparticle Deposition System. *Jpn J Appl Phys*. 2010;49:05EC9-1-4.

[46] Chun D-M, Kim M-S, Yeo J-C, Kim M-H, Lee CS, Ahn S-H. Nano/micro particle beam for ceramic deposition and mechanical etching.

Physica Scripta. 2010;2010:014047.

[47] Chun DM. Development of nano particle deposition system (NPDS) for room temperature deposition of metals and ceramics and its applications. Seoul Seoul National University; 2010.

[48] Lin HT, McDonald JF, Corelli JC, Balakrishnan S, King N. Focused electron and ion beam repair strategies for wafer-scale interconnections in thin film packaging. *Thin Solid Films*. 1988;166:121-30.

[49] Sudraud P, Benassayag G, Bon M. Focused ion beam repair in microelectronics. *Microelectronic Engineering*. 1987;6:583-95.

[50] Van Camp R, Van Doorselaer K, Clemminck I. Reliability of a focused ion beam repair on digital cmos circuits. *Microelectronics Reliability*. 1996;36:1787-90.

[51] Ho Kahng Y, Choi J, Jeong K, Chon Park B, Kim D-H, Lyou J, et al. Fabrication of ball-shaped atomic force microscope tips by ion-beam-induced deposition of platinum on multiwall carbon nanotubes. *Ultramicroscopy*. 2009;110:82-8.

[52] Kim CS, Park J, Chu WS, Jang DY, Kim SD, Ahn SH. Fabrication of silicon micro-mould for polymer replication using focused ion beam. *Microelectronic Engineering*. 2009;86:556-60.

[53] Stomeo T, Visimberga G, Todaro MT, Passaseo A, Cingolani R, De Vittorio M, et al. Rapid prototyping of two-dimensional photonic crystal devices by a dual beam focused ion beam system. *Microelectronic Engineering*. 2005;78–79:417-21.

[54] An Q, Dong N, Chen F, Lin W. Photonic crystal structure in Nd:YAG laser crystals. *Optical Materials*. 2012;34:1811-4.

[55] Kim C-S, Ahn S-H, Jang D-Y. Review: Developments in micro/nanoscale fabrication by focused ion beams. *Vacuum*. 2012;86:1014-35.

[56] Groeber MA, Haley BK, Uchic MD, Dimiduk DM, Ghosh S. 3D reconstruction and characterization of polycrystalline microstructures using a FIB–SEM system. *Materials Characterization*. 2006;57:259-73.

- [57] Inkson BJ, Mulvihill M, Möbus G. 3D determination of grain shape in a FeAl-based nanocomposite by 3D FIB tomography. *Scripta Materialia*. 2001;45:753-8.
- [58] Uchic MD, Groeber MA, Dimiduk DM, Simmons JP. 3D microstructural characterization of nickel superalloys via serial-sectioning using a dual beam FIB-SEM. *Scripta Materialia*. 2006;55:23-8.
- [59] Singh DRP, Chawla N, Shen YL. Focused Ion Beam (FIB) tomography of nanoindentation damage in nanoscale metal/ceramic multilayers. *Materials Characterization*. 2010;61:481-8.
- [60] Schmidt F, Kühbacher M, Gross U, Kyriakopoulos A, Schubert H, Zehbe R. From 2D slices to 3D volumes: Image based reconstruction and morphological characterization of hippocampal cells on charged and uncharged surfaces using FIB/SEM serial sectioning. *Ultramicroscopy*. 2011;111:259-66.
- [61] Wang K, Strunk K, Zhao G, Gray JL, Zhang P. 3D structure determination of native mammalian cells using cryo-FIB and cryo-electron tomography. *Journal of Structural Biology*. 2012;180:318-26.
- [62] Schroeder-Reiter E, Pérez-Willard F, Zeile U, Wanner G. Focused ion beam (FIB) combined with high resolution scanning electron microscopy: A promising tool for 3D analysis of chromosome architecture. *Journal of Structural Biology*. 2009;165:97-106.
- [63] Utke I, Hoffmann P, Melngailis J. Gas-assisted focused electron beam and ion beam processing and fabrication. *Journal of Vacuum Science & Technology B: Microelectronics and Nanometer Structures*. 2008;26:1197-276.
- [64] <http://www.orsayphysics.com/>.
- [65] Chun D-M, Ahn S-H. Deposition mechanism of dry sprayed ceramic particles at room temperature using a nano-particle deposition system. *Acta Materialia*. 2011;59:2693-703.
- [66] Chun D-M, Choi J-O, Lee C, Kanno I, Kotera H, Ahn S-H. Nano-particle

- deposition system (NPDS): Low energy solvent-free dry spray process for direct patterning of metals and ceramics at room temperature. *International Journal of Precision Engineering and Manufacturing*. 2012;13:1107-12.
- [67] Ahn S-H, Choi J-O, Kim C-S, Lee G-Y, Lee H-T, Cho K, et al. Laser-assisted nano particle deposition system and its application for dye sensitized solar cell fabrication. *CIRP Annals - Manufacturing Technology*. 2012;61:575-8.
- [68] Chun D-M, Choi J-O, Lee CS, Ahn S-H. Effect of stand-off distance for cold gas spraying of fine ceramic particles ( $<5 \mu\text{m}$ ) under low vacuum and room temperature using nano-particle deposition system (NPDS). *Surface and Coatings Technology*. 2012;206:2125-32.
- [69] Kim M-S, Chun D-M, Choi J-O, Lee J-C, Kim K-S, Kim Y, et al. Room temperature deposition of  $\text{TiO}_2$  using nano particle deposition system (NPDS): Application to dye-sensitized solar cell (DSSC). *International Journal of Precision Engineering and Manufacturing*. 2011;12:749-52.
- [70] Jung K, Song W, Chun D-M, Yeo J-C, Kim M-S, Ahn S-H, et al. Coating of Ni powders through micronozzle in a nano particle deposition system. *Met Mater Int*. 2010;16:465-7.
- [71] Kim MS. Manufacturing of flexible dye-sensitized solar cell (DSSC) using nano particle deposition system (NPDS): Seoul National University; 2011.
- [72] El-Daly AA, Hammad AE, Fawzy A, A. Nasrallah D. Microstructure, mechanical properties, and deformation behavior of Sn–1.0Ag–0.5Cu solder after Ni and Sb additions. *Materials & Design*. 2013;43:40-9.
- [73] Li G-y, Shi X-q. Effects of bismuth on growth of intermetallic compounds in Sn-Ag-Cu Pb-free solder joints. *Transactions of Nonferrous Metals Society of China*. 2006;16, Supplement 2:s739-s43.
- [74] Zhao X-y, Zhao M-q, Cui X-q, Tong M-x. Effect of cerium on microstructure and mechanical properties of Sn-Ag-Cu system lead-free solder alloys. *Transactions of Nonferrous Metals Society of China*.

2007;17:805-10.

[75] Lucas IT, Syzdek J, Kostecki R. Interfacial processes at single-crystal  $\beta$ -Sn electrodes in organic carbonate electrolytes. *Electrochemistry Communications*. 2011;13:1271-5.

[76] Marinel S, Choi DH, Heuguet R, Agrawal D, Lanagan M. Broadband dielectric characterization of TiO<sub>2</sub> ceramics sintered through microwave and conventional processes. *Ceramics International*. 2013;39:299-306.

[77] Wang H, Wei J, Xiong R, Shi J. Enhanced ferromagnetic properties of Fe+N codoped TiO<sub>2</sub> anatase. *Journal of Magnetism and Magnetic Materials*. 2012;324:2057-61.

[78] Kesmez Ö, Erdem Çamurlu H, Burunkaya E, Arpaç E. Sol-gel preparation and characterization of anti-reflective and self-cleaning SiO<sub>2</sub>-TiO<sub>2</sub> double-layer nanometric films. *Solar Energy Materials and Solar Cells*. 2009;93:1833-9.

[79] Moon J, Park J-A, Lee S-J, Zyung T, Kim I-D. Pd-doped TiO<sub>2</sub> nanofiber networks for gas sensor applications. *Sensors and Actuators B: Chemical*. 2010;149:301-5.

[80] Marin E, Guzman L, Lanzutti A, Ensinger W, Fedrizzi L. Multilayer Al<sub>2</sub>O<sub>3</sub>/TiO<sub>2</sub> Atomic Layer Deposition coatings for the corrosion protection of stainless steel. *Thin Solid Films*. 2012;522:283-8.

[81] Shan MN, Wang SS, Bian ZQ, Liu JP, Zhao YL. Hybrid inverted organic photovoltaic cells based on nanoporous TiO<sub>2</sub> films and organic small molecules. *Solar Energy Materials and Solar Cells*. 2009;93:1613-7.

[82] <http://nsl.caltech.edu/research>.

[83] Lee K-M, Hu C-W, Chen H-W, Ho K-C. Incorporating carbon nanotube in a low-temperature fabrication process for dye-sensitized TiO<sub>2</sub> solar cells. *Solar Energy Materials and Solar Cells*. 2008;92:1628-33.

[84] [http://www.redorbit.com/news/technology/1869698/new\\_disc\\_could\\_hold\\_a\\_thousand\\_times\\_more\\_data/](http://www.redorbit.com/news/technology/1869698/new_disc_could_hold_a_thousand_times_more_data/).

[85] Krell A, Klimke J, Hutzler T. Advanced spinel and sub- $\mu$ m Al<sub>2</sub>O<sub>3</sub> for

transparent armour applications. *Journal of the European Ceramic Society*. 2009;29:275-81.

[86] Sang S, Li W, Pu J, Jian L. Novel Al<sub>2</sub>O<sub>3</sub>-based compressive seals for IT-SOFC applications. *Journal of Power Sources*. 2008;177:77-82.

[87] Zhou L, Zhou W, Su J, Luo F, Zhu D, Dong Y. Plasma sprayed Al<sub>2</sub>O<sub>3</sub>/FeCrAl composite coatings for electromagnetic wave absorption application. *Applied Surface Science*. 2012;258:2691-6.

[88] Kalmodia S, Goenka S, Laha T, Lahiri D, Basu B, Balani K. Microstructure, mechanical properties, and in vitro biocompatibility of spark plasma sintered hydroxyapatite–aluminum oxide–carbon nanotube composite. *Materials Science and Engineering: C*. 2010;30:1162-9.

[89] Si T, Liu N, Zhang Qa, You X. Thermal shock fatigue behavior of TiC/Al<sub>2</sub>O<sub>3</sub> composite ceramics. *Rare Metals*. 2008;27:308-14.

[90] Li H, Xu Y, Gao C, Zhao Y. Structural and textural evolution of Ni/ $\gamma$ -Al<sub>2</sub>O<sub>3</sub> catalyst under hydrothermal conditions. *Catalysis Today*. 2010;158:475-80.

[91] Szczygieł B, Kołodziej M. Composite Ni/Al<sub>2</sub>O<sub>3</sub> coatings and their corrosion resistance. *Electrochimica Acta*. 2005;50:4188-95.

[92] Chun DM. Development of nano particle deposition system for room temperature deposition of metals and ceramics and its applications: Seoul National University; 2010.

[93] Gaillard Y, Rico VJ, Jimenez-Pique E, González-Elipé AR. Nanoindentation of TiO<sub>2</sub> thin films with different microstructures. *Journal of Physics D: Applied Physics*. 2009;42:145305.

[94] Mathur S, Kuhn P. CVD of titanium oxide coatings: Comparative evaluation of thermal and plasma assisted processes. *Surface and Coatings Technology*. 2006;201:807-14.

[95] Stollberg DW, Hampikian JM, Riester L, Carter WB. Nanoindentation measurements of combustion CVD Al<sub>2</sub>O<sub>3</sub> and YSZ films. *Materials Science and Engineering: A*. 2003;359:112-8.

- [96] Tripp MK, Stampfer C, Miller DC, Helbling T, Herrmann CF, Hierold C, et al. The mechanical properties of atomic layer deposited alumina for use in micro- and nano-electromechanical systems. *Sensors and Actuators A: Physical*. 2006;130–131:419-29.
- [97] Selvakumar N, Barshilia HC, Rajam KS. Effect of substrate roughness on the apparent surface free energy of sputter deposited superhydrophobic polytetrafluoroethylene coatings: A comparison of experimental data with different theoretical models. *Journal of Applied Physics*. 2010;108:013505-9.
- [98] Wu S. *Polymer interface and adhesion*. Marcel Dekker, New York; 1982.
- [99] Gierak J, Mailly D, Faini G, Pelouard JL, Denk P, Pardo F, et al. Nano-fabrication with focused ion beams. *Microelectronic Engineering*. 2001;57–58:865-75.
- [100] Nagata T, Ahmet P, Yamauchi Y, Sakuma Y, Sekiguchi T, Chikyow T. Three-dimensional GaN nano-structure fabrication by focused ion beam chemical vapor deposition. *Nuclear Instruments and Methods in Physics Research Section B: Beam Interactions with Materials and Atoms*. 2006;242:250-2.
- [101] Xu X, Chen H, Xiong Z, Jin A, Gu C, Cheng B, et al. Fabrication of photonic crystals on several kinds of semiconductor materials by using focused-ion beam method. *Thin Solid Films*. 2007;515:8297-300.
- [102] Sun J, Luo X, Ritchie JM, Chang W, Wang W. An investigation of redeposition effect for deterministic fabrication of nanodots by focused ion beam. *Precision Engineering*. 2012;36:31-6.
- [103] Hobler G, Kovač D. Dynamic binary collision simulation of focused ion beam milling of deep trenches. *Nuclear Instruments and Methods in Physics Research Section B: Beam Interactions with Materials and Atoms*. 2011;269:1609-13.
- [104] Kim C-S, Ahn S-H, Jang D-Y. Nanoscale effects in carbon structures fabricated using focused ion beam-chemical vapor deposition. *Thin Solid Films*. 2010;518:5177-82.

- [105] Hopman WCL, Ay F, Hu W, Gadgil VJ, Kuipers L, Pollnau M, et al. Focused ion beam scan routine, dwell time and dose optimizations for submicrometre period planar photonic crystal components and stamps in silicon. *Nanotechnology*. 2007;18:195305.
- [106] Rommel M, Jambrech JD, Ebm C, Platzgummer E, Bauer AJ, Frey L. Influence of FIB patterning strategies on the shape of 3D structures: Comparison of experiments with simulations. *Microelectronic Engineering*. 2010;87:1566-8.
- [107] Kim C-S, Kim H-J, Ahn S-H, Jang D-Y. Morphological influence of the beam overlap in focused ion beam induced deposition using raster scan. *Microelectronic Engineering*. 2010;87:972-6.
- [108] Frey L, Lehrer C, Ryssel H. Nanoscale effects in focused ion beam processing. *Appl Phys A*. 2003;76:1017-23.
- [109] de Winter DAM, Mulders JJJL. Redeposition characteristics of focused ion beam milling for nanofabrication. 6 ed: AVS; 2007. p. 2215-8.
- [110] Cairney JM, Munroe PR. Redeposition effects in transmission electron microscope specimens of FeAl–WC composites prepared using a focused ion beam. *Micron*. 2003;34:97-107.
- [111] Matteson TL, Schwarz SW, Houge EC, Kempshall BW, Giannuzzi LA. Electron backscattering diffraction investigation of focused ion beam surfaces. *Journal of Elec Materi*. 2002;31:33-9.
- [112] Chu CH, Hsieh YF, Harriott LR, Wade HH. Structural damage induced by Ga<sup>+</sup> focused ion beam implantation in (001) Si. *Journal of Vacuum Science & Technology B: Microelectronics and Nanometer Structures*. 1991;9:3451-5.
- [113] Philipp MN, Rolf B. Milling micro-structures using focused ion beams and its application to photonic components. *Measurement Science and Technology*. 2006;17:943.
- [114] Lindsey S, Hobler G. The significance of redeposition and backscattering in nanostructure formation by focused ion beams. *Nuclear*

Instruments and Methods in Physics Research Section B: Beam Interactions with Materials and Atoms. 2012;282:12-6.

[115] Li W, Minev R, Dimov S, Lalev G. Patterning of amorphous and polycrystalline Ni<sub>78</sub>B<sub>14</sub>Si<sub>8</sub> with a focused-ion-beam. Applied Surface Science. 2007;253:5404-10.

[116] Motooka T, Holland OW. Amorphization processes in ion implanted Si: Ion species effects. Applied Physics Letters. 1992;61:3005-7.

[117] Fedina L, Gutakovskii A, Aseev A, Van Landuyt J, Vanhellefont J. Extended Defects Formation in Si Crystals by Clustering of Intrinsic Point Defects Studied by in-situ Electron Irradiation in an HREM. *physica status solidi (a)*. 1999;171:147-58.

[118] Toth M, Lobo CJ, Hartigan G, Knowles WR. Electron flux controlled switching between electron beam induced etching and deposition. Journal of Applied Physics. 2007;101:054309-6.

[119] Pelaz L, Marques LA, Barbolla J. Ion-beam-induced amorphization and recrystallization in silicon. Journal of Applied Physics. 2004;96:5947-76.

[120] Motooka T, Holland OW. Amorphization processes in self-ion-implanted Si: Dose dependence. Applied Physics Letters. 1991;58:2360-2.

[121] Dubner AD, Wagner A, Melngailis J, Thompson CV. The role of the ion-solid interaction in ion-beam-induced deposition of gold. Journal of Applied Physics. 1991;70:665-73.

[122] Reyntjens S, Puers R. A review of focused ion beam applications in microsystem technology. Journal of Micromechanics and Microengineering. 2001;11:287.

[123] Ro JS, Thompson CV, Melngailis J. Mechanism of ion beam induced deposition of gold. Journal of Vacuum Science & Technology B: Microelectronics and Nanometer Structures. 1994;12:73-7.

[124] Bret T, Utke I, Hoffmann P. Influence of the beam scan direction during focused electron beam induced deposition of 3D nanostructures. Microelectronic Engineering. 2005;78-79:307-13.

- [125] Xu X, Xu S, Jin L, Song E. Characteristic analysis of Otsu threshold and its applications. *Pattern Recognition Letters*. 2011;32:956-61.
- [126] Adams DP, Vasile MJ. Accurate focused ion beam sculpting of silicon using a variable pixel dwell time approach. *Journal of Vacuum Science & Technology B: Microelectronics and Nanometer Structures*. 2006;24:836-44.
- [127] Adams DP, Vasile MJ, Mayer TM. Focused ion beam sculpting curved shape cavities in crystalline and amorphous targets. *Journal of Vacuum Science & Technology B: Microelectronics and Nanometer Structures*. 2006;24:1766-75.
- [128] Fu Y, Bryan NKA. Fabrication of three-dimensional microstructures by two-dimensional slice by slice approaching via focused ion beam milling. *Journal of Vacuum Science & Technology B: Microelectronics and Nanometer Structures*. 2004;22:1672-8.
- [129] Yamaguchi H, Shimase A, Haraichi S, Miyauchi T. Characteristics of silicon removal by fine focused gallium ion beam. *Journal of Vacuum Science & Technology B: Microelectronics and Nanometer Structures*. 1985;3:71-4.
- [130] Kubena RL, Seliger RL, Stevens EH. High resolution sputtering using a focused ion beam. *Thin Solid Films*. 1982;92:165-9.
- [131] Santamore D, Edinger K, Orloff J, Melngailis J. Focused ion beam sputter yield change as a function of scan speed. 6 ed. Dana Point, California (USA): AVS; 1997. p. 2346-9.
- [132] Steffens HD, Wielage B, Drozak J. Interface phenomena and bonding mechanism of thermally-sprayed metal and ceramic composites. *Surface and Coatings Technology*. 1991;45:299-308.
- [133] Ganesan A, Affi J, Yamada M, Fukumoto M. Bonding behavior studies of cold sprayed copper coating on the PVC polymer substrate. *Surface and Coatings Technology*. 2012;207:262-9.
- [134] Klinkov SV, Kosarev VF, Rein M. Cold spray deposition: Significance of particle impact phenomena. *Aerospace Science and Technology*. 2005;9:582-91.

- [135] Gramotnev DK, Gramotnev G. A new mechanism of aerosol evolution near a busy road: fragmentation of nanoparticles. *Journal of Aerosol Science*. 2005;36:323-40.
- [136] Stepanov AL. Synthesis of silver nanoparticles in dielectric matrix by ion implantation: a review. *Rev Adv Mater Sci*. 2010;26:1-29.
- [137] Akedo J. Aerosol Deposition of Ceramic Thick Films at Room Temperature: Densification Mechanism of Ceramic Layers. *Journal of the American Ceramic Society*. 2006;89:1834-9.
- [138] Akedo J. Room temperature impact consolidation (RTIC) of fine ceramic powder by aerosol deposition method and applications to microdevices. *Journal of Thermal Spray Technology*. 2008;17:181-98.
- [139] Fu YQ, Zhang S, Wu MJ, Huang WM, Du HJ, Luo JK, et al. On the lower thickness boundary of sputtered TiNi films for shape memory application. *Thin Solid Films*. 2006;515:80-6.
- [140] Clark BG, Gianola DS, Kraft O, Frick CP. Size Independent Shape Memory Behavior of Nickel–Titanium. *Advanced Engineering Materials*. 2010;12:808-15.
- [141] Dmitry Z, Gor L, Artemy I, Veronika A, Alexey M, Vladimir K, et al. Submicron-sized actuators based on enhanced shape memory composite material fabricated by FIB-CVD. *Smart Materials and Structures*. 2012;21:052001.
- [142] Bellouard Y. Shape memory alloys for microsystems: A review from a material research perspective. *Materials Science and Engineering: A*. 2008;481–482:582-9.
- [143] Casati R, Passaretti F, Tuissi A. Effect of electrical heating conditions on functional fatigue of thin NiTi wire for shape memory actuators. *Procedia Engineering*. 2011;10:3423-8.
- [144] Costanza G, Tata ME, Calisti C. Nitinol one-way shape memory springs: Thermomechanical characterization and actuator design. *Sensors and Actuators A: Physical*. 2010;157:113-7.

- [145] Duerig T, Pelton A, Stöckel D. An overview of nitinol medical applications. *Materials Science and Engineering: A*. 1999;273–275:149-60.
- [146] Rogante M, Pasquini U, Rosta L, Lebedev V. Feasibility study for the investigation of Nitinol self-expanding stents by neutron techniques. *Physica B: Condensed Matter*. 2011;406:527-32.

## 국문 초록

구조 및 시스템의 소형화 및 다중재료를 이용한 기능구조의 지속적인 요구에 따라 마이크로/나노영역에서 3 차원 구조를 손쉽게 제작할 수 있는 새로운 공정에 대한 개발이 요구된다. 이와 같은 공정의 개발을 위하여 두 가지 기술적인 패러다임인 3 차원 인쇄 및 하이브리드 개념을 도입하여 큰 시너지를 얻을 수 있는 공정을 개발하고자 하였다. 따라서 본 연구는 적층 및 절삭에 사용될 수 있는 나노입자적층시스템 (NPDS) 및 집속이온빔 (FIB) 공정을 통합하였으며, 이를 통하여 기존에 없는 나노스케일 3 차원 인쇄공정 (Nanoscale 3D Printing Process)을 개발하였다.

나노입자 적층시스템의 경우, 금속 (Sn)과 세라믹 ( $\text{TiO}_2$  및  $\text{Al}_2\text{O}_3$ ) 입자를 이용하여 공정 변수 (이송속도 및 노즐/기판 거리)에 따라 박막을 적층 특성을 파악하였다. 결과 NPDS를 이용하여 나노 정밀도의 박막을 제작할 수 있음을 보였다. 또한 제작된 3가지 재료의 박막에 대한 물리적 특성 (압입강도/탄성계수/접착일/마이크로구조)을 평가하여 박막으로 사용될 수 있음을 확인하였다.

집속이온빔의 경우 정밀하고 빠른 프로파일 절삭을 위한 선 (line) 기반의 이온빔 주사제어 방식을 점 (dot) 기반으로 개선하여 이온빔의 위치를 자유자재로 조절할 수 있도록 하였다. 점/선기반의 이온빔 주사방식에 따른 공정변수 (주거시간 및 빔중첩)의 영향을 분석하여 점기반의 이온빔 주사 방식이 효율 및 정밀도가 증가함을 보였다. 또한 점기반 이온빔 제어를 이용하여 오프셋, 스파이럴 등의 가공형상에 맞는 새로운 이온빔 가공경로를 생성하였으며 이를 적

용한 집속이온빔 프로파일 절삭할 시 가공형상의 정밀도/정확도가 개선됨을 보였다.

나노입자 적층시스템과 집속이온빔 공정을 통합하여 다종재료로 구성된 2~3차원 나노구조를 다양한 방법으로 제작할 수 있음을 보였다. 또한 통합공정을 통하여 제작된 박막 (Sn, TiO<sub>2</sub> 및 Al<sub>2</sub>O<sub>3</sub>)의 표면/계면에 대한 마이크로구조 분석을 진행함으로써 금속 입자 및 세라믹 입자를 이용한 NPDS 적층 메커니즘을 제시하였다.

마지막으로 본 공정 중 집속이온빔 공정을 형상기억합금에 적용하여 나노 구동기를 제작하는 예를 보였으며 이의 나노구동에 대한 모델을 제시하고 검증하였다. 또한 형상기억합금과 같은 지능재료에 나노입자 적층이 가능함으로 선보였다.

결론적으로 다종재료를 이용한 3차원 나노구조의 제작을 위하여 새로운 공정 및 시스템 개발이 이루어졌다. 개발된 공정을 이용하여 다종재료 3차원 나노구조를 정밀/정확하게 제작하는 기본적인 연구가 진행되었다. 기본적인 가공공정에 대한 연구를 통하여 본 논문에서 개발된 통합 공정이 나노스케일 3차원 인쇄공정을 수행할 수 있는 것을 보였다.

**주요어:** 나노스케일 3 차원 인쇄공정, 나노입자 적층시스템, 집속이온빔, 다종재료, 나노구동기

**학번:** 2007-30192